EFFICIENT SEISMIC MODELING IN MULTI-SCALE HETEROGENEOUS MEDIA

A DISSERTATION
SUBMITTED TO THE DEPARTMENT OF GEOPHYSICS
AND THE COMMITTEE ON GRADUATE STUDIES
OF STANFORD UNIVERSITY
IN PARTIAL FULFILLMENT OF THE REQUIREMENTS
FOR THE DEGREE OF
DOCTOR OF PHILOSOPHY

Chunling Wu
June 2005

© Copyright 2005 by Chunling Wu
All Rights Reserved

I certify that I have read this dissertation and that in my opinion it is fully adequate, in scope and in quality, as a dissertation for the degree of Doctor of Philosophy.

Jerry M. Harris
(Principal Advisor)

I certify that I have read this dissertation and that in my opinion it is fully adequate, in scope and in quality, as a dissertation for the degree of Doctor of Philosophy.

Gregory C. Beroza

I certify that I have read this dissertation and that in my opinion it is fully adequate, in scope and in quality, as a dissertation for the degree of Doctor of Philosophy.

Biondo Biondi

I certify that I have read this dissertation and that in my opinion it is fully adequate, in scope and in quality, as a dissertation for the degree of Doctor of Philosophy.

Richard T. Coates

Approved for the University Committee on Graduate Studies.

Abstract

Numerical seismic modeling can aid in the understanding of wave patterns observed on seismograms and can provide crucial guidance on seismic experiment design, data processing, and data interpretation. However, modeling wave propagation in multi-scale heterogeneous media can be extremely computationally intensive, especially if small spatial sampling, required by small features, is used throughout a large domain.

In this thesis, I present a new variable grid finite-difference (FD) method for solving wave equations. This method accommodates multi-scale features by allowing fine grid spacing for zones with small-scale features, and coarse grid spacing for zones with large-scale structures. Since the FD stability condition requires a very small timestep for the finest grid spacing, a spatially variable timestep FD technique is implemented to further reduce CPU time by providing small timesteps for zones with fine grid spacing and large timesteps for zones with coarse grid spacing. Comparing numerical results of the variable grid, and the variable grid and timestep FD methods with those obtained by the conventional constant grid and timestep FD method demonstrates their high accuracy and efficiency. Furthermore, parallel versions of the variable grid FD codes are developed for efficient solution of large problems.

Four applications are used to demonstrate the efficacy and the benefits of the developed techniques. First, I directly model an open fluid-filled fracture using the variable grid FD method and compare the numerical results with those obtained using an equivalent medium theory. Then, the variable grid and timestep FD method is used for efficient single-well seismic modeling with a realistic-sized borehole in the modeling scheme. Third, I use a parallel variable grid FD code to model cross-well field data with inclusion of tube-waves and tube-wave-related arrivals caused by the presence of the perforated cased boreholes. Finally, I apply the variable grid FD method for DARS (Differential Acoustic Resonance Spectroscopy) lab data simulation to better understand the theory and to guide experimental design and data analysis.

Acknowledgments

First, I would like to thank my advisor, Jerry Harris, for his guidance and contributions to my education and research. I've learned a lot from Jerry about wave theory, how to analyze data, and how to communicate ideas. I would also like to thank Jerry for his patience, encouragement, support, and above all friendship during my years at Stanford.

I'd like to thank my academic committee members, Greg Beroza and Biondo Biondi, for their constructive comments and excellent suggestions during my qualifying exam, annual reviews, and interesting discussions. Richard Coates of Schlumberger-Doll Research (SDR) also served on my academic committee and I am grateful for his suggestions and support. I especially want to thank Richard for traveling a significant distance to serve on my oral exam committee. I would also like to thank Lou Durlofsky for his willingness to chair my oral exam.

I greatly enjoyed being a member of Stanford Wave Physics Lab (SWP). I thank Xianyun Wu, Xiuming Wang, and Guan Wang for mentoring me when I started at SWP. I thank Jonathan Ajo-Franklin, Jaime Urban, Martins Akintunde, Chuntang Xu, and Jolene Robin-McCaskill, for being great fellow students. I specially thank Jonathan, now a postdoc in MIT, for coming back Stanford for my defense. I also thank Youli Quan, Pratap Sahay, and Fred Boadu for their help and enthusiasm in sharing research ideas.

I still remember the broken Chinese-English I spoke when I first arrived at Stanford. Thanks to Jerry for helping me and waiting for me to start speaking understandable English. Thanks to Jonathan and Adam Pidlisecky for helping me in editing most of my papers. Thanks also to Claudia Baroni for reading through the final draft

of my thesis. Special thanks to my friend Dee Baily and her husband Jon Heiner for helping with my English and for many other things.

I am also thankful to all Geophysics faculty, staff and students for creating such wonderful study and research environment. The past six and a half years have been one of the best parts in my life experience.

Financial support for my research is from DOE through Lawrence Berkeley National Laboratory (LBNL). Scientists in LBNL, especially Kurt Nihei, Seiji Nakagawa, Tom Daley, and Ernie Majer, offered me a tremendous amount of help in getting me some data and discussing my research. They are co-authors of some of my published papers.

I benefited from many discussions and a wonderful summer time working with Richard Coates at SDR. I thank Kurt Nihei for the fruitful summer with LBNL. I also acknowledge John Queen and Dale Cox who made my summer internship with Conoco Inc. such a pleasant one.

Finally, I'd like to thank my family, especially my husband Linbin and my son Ruxun for their continued love and support during this long journey. I thank my in-laws for helping me take care of my son for years. I also thank my parents for supporting and encouraging my education since the very beginning.

Contents

List of Figures

Chapter 1

Introduction

The main focus of this thesis has been to develop and apply efficient finite-difference techniques to model wave propagation in multi-scale heterogeneous media to guide seismic experiment design, data processing, and data interpretation.

In this chapter, first I present the research motivation; then I discuss numerical modeling methods; third I overview applications; and finally I briefly describe the chapters of this dissertation.

1.1 Research motivation

In seismology, variations in the subsurface of the earth are often present on many scales: from scales much larger than the typical seismic wavelength down to scales that are much smaller. Figure 1.1 shows a model with multi-scale structures: a large-scale salt dome, thick layers, small-scale thin layers, fractures and a borehole. The presence of heterogeneous structures at various scales often leads to a very complicated wavefield. In fact, even heterogeneities that are much smaller than the seismic wavelength can have significant effects on the wavefield. For example, the presence of borehole(s) often causes strong tube waves in borehole seismic data (Campbell, 1992; Mo and Harris, 1995; Wu et al., 2001; Wu et al., 2004); and the aligned fractures often induce azimuthal anisotropy on field observations (Lynn and Thomsen, 1986; Garotta, 1989; and Lynn et al., 1995).

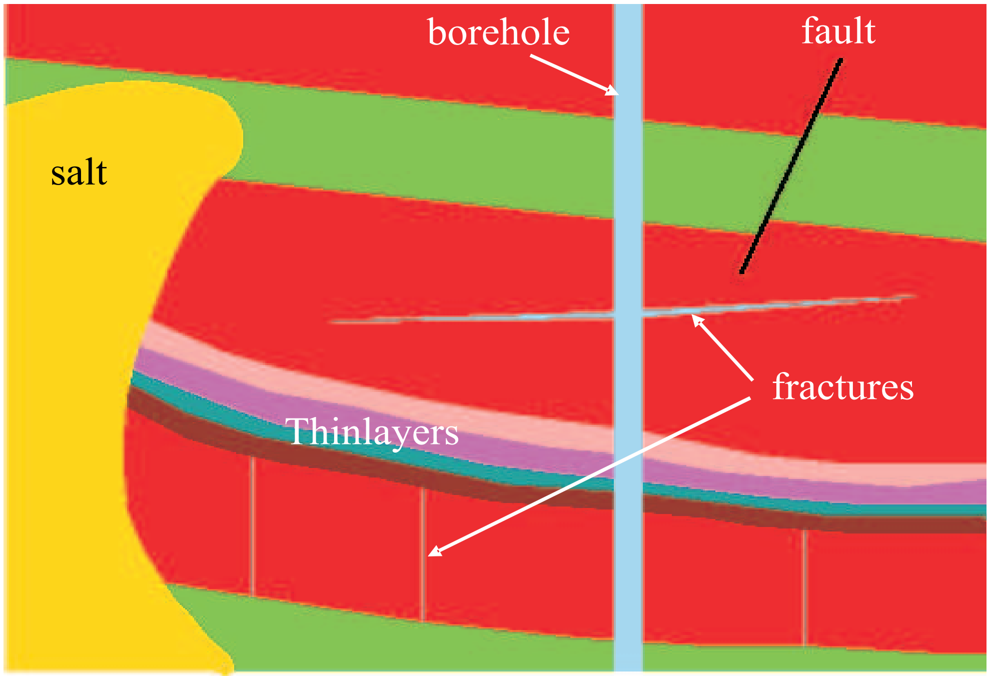

Figure 1.1: A model with multi-scale structures: a large-scale salt dome, thick layers, small-scale thin layers, fractures and a borehole.

Numerical seismic modeling can aid in the understanding of wave patterns observed on seismograms and can provide crucial guidance on seismic survey design, data processing, and data interpretation. However, modeling wave propagation in multi-scale heterogeneous media can be extremely computationally intensive because of the large range of spatial scales present. In order to resolve the small-scale features such as boreholes or/and fractures which are often 2 or 3 orders of magnitude smaller than the typical seismic wavelength in the medium, a very fine grid spacing is required. Using this fine grid spacing throughout the entire domain will require too much memory and CPU time thereafter for simulation on most computers. It is desirable to develop special computational techniques for efficient seismic modeling in multi-scale heterogeneous media to aid in experimental design, data processing, and data interpretation.

1.2 Modeling methods

1.2.1 Review

There are a variety of approaches for seismic modeling which can be classified as: (1) analytical methods (e.g. Green's function and Cagniard-de Hoop), (2) semi-analytical methods (e.g. integral-equation), (3) asymptotic methods (ray tracing), and (4) direct methods (finite-difference, finite-element, and pseudo-spectral). These techniques differ by their regime of validity, their usefulness and their cost.

Analytical methods (e.g. Lamb, 1904) are limited for problems with very simple geometries. However, they yield exact solutions which can serve as reference results for other modeling methods.

Integral-equation methods (Cruse and Rizzo, 1968; and Cruse, 1968) are based on integral representations of the wavefield in terms of waves originating from point sources. These methods are very efficient and accurate for specific geometries, such as a bounded object in a homogeneous background. However, they require high computational cost for complex geometries.

Asymptotic methods or ray tracing methods (Cerveny et al., 1977) are based on high frequency asymptotic solutions to the wave equation; therefore they do not take the full wavefield into account. Amplitude and spectral characteristics modeled by these methods are not always accurate, particularly when the medium contains wavelength-scale or smaller heterogeneities. On the other hand, they are very efficient for computing the arrival times of waves and are very useful for identifying specific events on seismic records.

Direct methods, e.g. finite-difference (FD), finite-element (FE) and pseudo-spectral (PS) methods, numerically solve wave equations on a discrete grid; therefore they are also called grid methods. These techniques simulate the full wavefield. Direct or grid methods can model wave propagation in arbitrarily inhomogeneous media and can achieve high accuracy by using a fine grid. Furthermore, these techniques provide the ability to generate snapshots or movies of the wavefield which are very important for the interpretation of the results. However, a main disadvantage of these general methods is the computational cost which can be more expensive than the analytical and ray methods.

1.2.2 The choice of FD method

The objective of this thesis is to efficiently model wave propagation in multi-scale heterogeneous media. Clearly this goal has significant influence on the choice of algorithm. The most likely candidates are the direct or grid methods which can model wave propagation in arbitrarily heterogeneous media. Further requirements for the grid method to be chosen are:

- high accuracy,
- low operation cost,
- compatibility with multi-scale heterogeneities,
- easy parallelization.

Most existing grid approaches excel in one or sometimes two of these respects. For example, the FE method (Lysmer and Drake, 1972; Drake, 1972) is very flexible in incorporating variable geometries, but it has difficulty achieving high accuracy without a large operation count; the PS method (Gazdag, 1981; Kosloff and Baysal, 1982) is accurate and efficient in modeling large models with a coarse grid, but it is often incompatible with multi-scale structures.

The FD method (Alterman and Karal, 1968; Kelly et al., 1976) is an alternative grid based modeling method. This method is less computationally intensive than the FE method, and is more flexible in representing multi-scale features than the PS method. Also, the FD method is easy and straight forward to implement, and can be easily parallelized on a parallel computer.

Therefore, I choose to explore and improve the FD method to efficiently model wave propagation in multi-scale heterogeneous media. The new FD scheme to be developed will meet all the four requirements above.

1.2.3 The history of FD modeling

Alterman and Karal (1968) pioneered in the use of FD techniques in seismic modeling. They developed a discrete solution to the second-order elastic wave equation in homogeneous regions by the use of explicit time integration methods. For this method, boundary conditions across all interfaces separating different regions must be satisfied explicitly.

A heterogeneous FD algorithm solution of the second-order system of equations on a single grid was introduced by Boore (1972) and extended by Kelly et al. (1976). This approach incorporates the boundary conditions implicitly by specifying physical properties at each node of a FD grid; therefore it provides the flexibility required to simulate a variety of complex subsurface geometries.

Madariaga (1976) developed the first of currently very popular staggered grid FD algorithms based on the first-order velocity-stress equation to model fault-rupture dynamics. Virieux (1984, 1986) and Levander (1988) have since extended the technique to model wave propagation in 2-D media, and the formulation for 3-D media is outlined by Randall (1989). The advantage of the staggered grid FD scheme is that it is stable and accurate for modeling large Poisson's ratio materials and mixed acoustic-elastic media.

The displacement-stress staggered grid FD scheme was introduced by Luo and Schuster (1990) and extended to the 3-D case by Olsen and Schuster (1992). This FD scheme requires less computer memory than the velocity-stress scheme since it only stores displacement components, not stress components.

Recently, many efforts have been made to optimize FD modeling. For example, Falk et al. developed a varying grid spacing (1996) and a adjustable timestep (1998) FD technique to avoid spatial and temporal oversampling for tube wave modeling. Zhang (1997) proposed a quadrangle-grid FD method to flexibly handle complex geometrical boundaries and interfaces. Saenger et al. (2000) presented a rotated grid FD scheme to improve the computational accuracy on modeling wave propagation in fractured media. All these techniques made FD modeling more efficient, accurate and flexible in representing variable complex structures.

1.2.4 The efficient FD techniques developed in this work

In this thesis, I explore and improve the FD method for efficient seismic modeling in multi-scale heterogeneous media.

I first developed an "optimized" variable grid FD scheme on a staggered grid mesh (Wu and Harris, 2002; Wu and Harris, 2004) for solution of wave equations. Variable grid FD methods can accommodate multi-scale features by allowing fine grid spacing for zones with small-scale features, and coarse grid spacing for zones with large-scale structures. The advantage of this optimized variable grid FD scheme is that it has less dispersion errors than the variable grid FD scheme based on the Taylor series expansion (Moczo, 1989; Jastram and Behle, 1991; Jastram and Tessmer, 1994; Falk et al., 1996; Pitarka, 1999); therefore it leads to either more accurate results or more efficient computations.

Using variable grid spacing for seismic modeling in multi-scale media considerably reduces computer memory requirements and CPU time, however the simulation is still time consuming. This is due to the use of a very small timestep required by the finest grid spacing to satisfy the FD stability condition. To overcome this problem, I developed a spatially variable timestep FD scheme for a spatial staggered grid based on the technique introduced by Tessmer (2000) for a spatial non-staggered grid. This variable timestep scheme is more flexible than the scheme proposed by Falk et al. (1998), because it can handle any integer timestep ratios between different domains. The use of the variable timestep scheme with the variable grid scheme in the FD method results in great savings in CPU time.

Recently, low-cost networked PC clusters (Beowulf clusters) have become widely available. In addition, the FD algorithm is well suited for distributed parallelization. Therefore, I developed 2-D/3-D parallel variable grid FD codes for solution of large realistic problems.

1.3 Applications

The developed FD techniques have a wide range of applications. Four examples are presented in this thesis.

First, I directly model a very small feature in a large homogeneous domain, i.e., an open fluid-filled fracture, using the variable grid FD method and compare the numerical results with those obtained using an equivalent medium theory. The comparison shows excellent agreement between the two methods for the wavefield away from the fracture. The discrepancy between the two is that a fracture slow wave is only observed from the variable grid FD simulation.

Then, I apply the variable grid and timestep FD method for single-well seismic modeling with the presence of a realistic-sized borehole in the modeling scheme. Numerical results show that reflections from the near vertical structures can be observed although strong tube waves obscure some temporal regions of the data.

Third, I use a parallel variable grid FD code to model cross-well field data with inclusion of the two perforated cased boreholes. The synthetics resemble the field observations not only on direct waves, but also on tube waves and tube-wave-related secondary arrivals generated by the perforations in the receiver and source wells.

Finally, I apply the variable grid FD method for DARS (Differential Acoustic Resonance Spectroscopy) lab data simulation to better understand the theory and to guide experimental design and data analysis.

These widely successful applications demonstrate the efficacy and the benefits of the developed FD techniques for efficient seismic modeling in multi-scale heterogeneous media.

1.4 Chapter description

The following is a brief description of each chapter in this dissertation.

This chapter presents the research motivation and thesis overview. Chapter 2 briefly reviews the derivation of the acoustic and elastic wave equations. These equations are solved by FD methods in the following chapters. Chapter 3 presents the finite-difference techniques (variable grid and variable time FD techniques). Their accuracy and efficiency are tested by numerical examples. Chapter 4 describes the parallel implementation of the variable grid FD algorithm in the 3-D case. The accuracy and the performance of the 3-D parallel code are demonstrated by numerical examples also.

In chapter 5, I apply the variable grid FD method to directly model an open fluid-filled fracture and compare these results with those obtained using an equivalent medium theory. Chapter 6 provides the application of the variable grid and timestep FD method for single-well seismic modeling with a small realistic-sized borehole in the modeling scheme. In chapter 7, I use a parallel 2-D variable grid FD code to model cross-well field data with inclusion of tube waves and tube-wave-related arrivals caused by the presence of the perforated cased boreholes. Finally, chapter 8 presents the application of the variable grid FD method for DARS modeling including DARS methodology and sensitivity study, and lab data simulation.

Chapter 2

Wave equations

This chapter presents a brief derivation of the acoustic and elastic wave equations that are numerically solved by the FD methods in the following chapters. First, we introduce the concepts of traction, stress and strain that characterize the forces in, and deformation of, a fluid or solid. Then, we present the relation between stress and strain, called the constitutive relation, in acoustic and elastic media. Finally, we derive wave equations based on the constitutive relations and Newton's law. We assume infinitesimal deformations and we limit our discussion to a Cartesian coordinate system.

2.1 Basic concepts

2.1.1 Traction and stress

The concepts of traction and stress are used to analyze the internal forces acting mutually between adjacent particles within a continuum.

Traction is a vector, being the force per unit area acting on a surface. Considering an infinitesimal force $\delta \mathbf{f}$ acting on an infinitesimal surface element δS with unit outward normal vector $\mathbf{n}$, the traction vector $\mathbf{t}$ is defined as:

$$\mathbf{t} = \lim_{\delta S \to 0} \frac{\delta \mathbf{f}}{\delta S} \tag{2.1}$$

The adopted convention is that **t** is the force per unit area exerted by the side to which **n** points, acting on the other side.

In equilibrium, the two sides exert equal and opposite tractions:

$$\mathbf{t}(-\mathbf{n}) = -\mathbf{t}(\mathbf{n}) \tag{2.2}$$

Traction depends on the orientation of the surface on which it acts. In Cartesian coordinates, tractions acting on the three coordinate planes can be represented as:

$$\mathbf{t}(\mathbf{x}_1) = \sigma_{11}\mathbf{x}_1 + \sigma_{21}\mathbf{x}_2 + \sigma_{31}\mathbf{x}_3 \tag{2.3}$$

$$\mathbf{t}(\mathbf{x}_2) = \sigma_{12}\mathbf{x}_1 + \sigma_{22}\mathbf{x}_2 + \sigma_{32}\mathbf{x}_3 \tag{2.4}$$

$$\mathbf{t}(\mathbf{x}_3) = \sigma_{13}\mathbf{x}_1 + \sigma_{23}\mathbf{x}_2 + \sigma_{33}\mathbf{x}_3 \tag{2.5}$$

The components σ_{ij} of these tractions are called stress components. Thus, stress is a tensor, being the set of components of tractions acting on the various surfaces. σ_{ij} is the *ith* component of traction acting on the *jth* plane.

We can use the stress tensor to calculate the traction on an arbitrarily oriented surface with unit normal **n**:

$$\mathbf{t} = \boldsymbol{\sigma} \cdot \mathbf{n}, \tag{2.6}$$

or

$$t_i = \sigma_{ij} n_j, \tag{2.7}$$

which is known as Cauchy's formula.

The stress tensor is symmetric

$$\sigma_{ij} = \sigma_{ji}, \tag{2.8}$$

therefore, there are only 6 independent terms. The diagonal components $(i = j)$ of the stress tensor are called normal stresses, and the off-diagonal components $(i \neq j)$ are called the shear stresses.

2.1.2 Strain

Strain is a geometric quantity that describes a change in size or shape. With strain, we have deformation or distortion of a medium, whether it is fluid or solid.

We can describe the deformation or distortion of a continuum with a vector displacement field $\mathbf{u}$. The displacement gives the vector motion of each point in the body. It is important to note that the displacement can vary with position.

For infinitesimal strain, the components of strain ϵ_{ij}, defined in terms of displacement, are:

$$\epsilon_{ij} = \frac{1}{2}(u_{i,j} + u_{j,i}). \tag{2.9}$$

Like the stress tensor, the strain tensor is symmetric

$$\epsilon_{ij} = \epsilon_{ji}, \tag{2.10}$$

and so has six independent terms too. The diagonal strain terms $(i = j)$, called normal strains, describe relative changes in length. The off-diagonal terms $(i \neq j)$, called shear strains, describe a change in angle.

The trace (sum of the diagonal components) of the strain tensor is volumetric strain θ, which is sometimes called the dilatation. It is given by

$$\theta = \epsilon_{ii} = \frac{\partial u_i}{\partial x_i} = \nabla \cdot \mathbf{u}. \tag{2.11}$$

2.2 Constitutive relation

The connection between stress and strain is called the constitutive relation or the stress-strain relation. For infinitesimal strain, the relation is given by Hooke's law, which states that the stress is linearly proportional to the strain. We now present the relations in an acoustic medium or fluid, and an elastic medium or solid.

2.2.1 Acoustic medium

In an acoustic medium or a fluid when viscous effects are assumed negligible, the shear stresses are zero and normal stresses equal to the pressure p acting on the medium. Thus we have:

$$\sigma_{ij} = -p\delta_{ij}, \tag{2.12}$$

or:

$$\boldsymbol{\sigma} = -p\mathbf{I}, \tag{2.13}$$

where $\mathbf{I}$ is the 3×3 identity matrix.

The pressure p causes a volumetric strain or dilatation θ defined by equation (2.11). The pressure and the accompanying dilatation are linearly related through the bulk modulus K:

$$p = -K\theta, \tag{2.14}$$

which expresses the generalized Hooke's law for a fluid. This constitutive relation is normally valid for small pressures and deformations ($\theta \ll 1$).

2.2.2 Elastic medium

In an elastic medium or a solid, both normal and shear stresses can be non-zero. For small elastic deformations ($\epsilon_{ij} \ll 1$), the generalized form of Hooke's law states that each component of the stress tensor is a linear combination of all components of the strain tensor:

$$\sigma_{ij} = c_{ijkl}\epsilon_{kl}, \tag{2.15}$$

where c_{ijkl}, called elastic stiffnesses, form a fourth-order tensor with 81 components. However, not all 81 components are independent. The symmetry of the stress tensor (2.8) and strain tensor (2.10) implies that

$$c_{ijkl} = c_{jikl} = c_{ijlk} = c_{jilk}, \tag{2.16}$$

reducing the number of independent constants to 36. Also the existence of a unique strain energy potential requires that

$$c_{ijkl} = c_{klij}, \tag{2.17}$$

further reducing the number of elastic constants to 21. Thus, the most general stiffness tensor for an elastic medium contains 21 independent parameters.

Alternatively, the strains may be expressed as a linear combination of the stresses by the expression

$$\epsilon_{ij} = s_{ijkl}\sigma_{kl}. \tag{2.18}$$

In this case, s_{ijkl} are elements of the elastic compliance tensor, which has the same symmetry as the corresponding stiffness tensor. The compliance and stiffness are tensor inverses denoted by

$$\begin{aligned} c_{ijkl}s_{klmn} &= I_{ijmn} \\ &= \frac{1}{2}(\delta_{im}\delta_{jn} + \delta_{in}\delta_{jm}). \end{aligned} \tag{2.19}$$

It is a standard practice in elasticity to use an abbreviated notation for the stress, strain and stiffness tensors, for doing so simplifies some of the key equations (Auld, 1973). In this abbreviated notation, the stresses and strains are written as six-element column vectors rather than as nine-element square matrices:

$$\begin{bmatrix} \sigma_1 = \sigma_{11} \\ \sigma_2 = \sigma_{22} \\ \sigma_3 = \sigma_{33} \\ \sigma_4 = \sigma_{23} \\ \sigma_5 = \sigma_{13} \\ \sigma_6 = \sigma_{12} \end{bmatrix}, \qquad \begin{bmatrix} \epsilon_1 = \epsilon_{11} \\ \epsilon_2 = \epsilon_{22} \\ \epsilon_3 = \epsilon_{33} \\ \epsilon_4 = 2\epsilon_{23} \\ \epsilon_5 = 2\epsilon_{13} \\ \epsilon_6 = 2\epsilon_{12} \end{bmatrix}. \tag{2.20}$$

Note the factor of 2 in the definitions of strains.

The four subscripts of the stiffness tensor are reduced to two. Each pair of indexes $ij(kl)$ is replaced by one index $I(J)$ using the following convention:

$$\begin{array}{cc} ij(kl) & I(J) \\ 11 & 1 \\ 22 & 2 \\ 33 & 3 \\ 23,32 & 4 \\ 13,31 & 5 \\ 12,21 & 6 \end{array} \qquad (2.21)$$

The relation, therefore, is:

$$c_{IJ} = c_{ijkl}, \qquad (I, J = 1, 2, \cdots, 6), \qquad (2.22)$$

and

$$s_{IJ} = s_{ijkl}N, \qquad (I, J = 1, 2, \cdots, 6), \qquad (2.23)$$

where

$$N = \begin{cases} 1 \text{ for } I \text{ and } J = 1, 2, 3 \\ 2 \text{ for } I \text{ or } J = 4, 5, 6 \\ 4 \text{ for } I \text{ and } J = 4, 5, 6 \end{cases}$$

Then, the constitutive relation (2.15) and (2.18) can be rewritten as

$$\sigma_I = c_{IJ}\epsilon_J, \qquad (I, J = 1, 2, \cdots, 6). \qquad (2.24)$$

and

$$\epsilon_I = s_{IJ}\sigma_J, \qquad (I, J = 1, 2, \cdots, 6). \qquad (2.25)$$

respectively. c_{IJ} and s_{IJ} form 6×6 stiffness matrix $\mathbf{C}$ and compliance matrix $\mathbf{S}$, respectively.

The stiffness matrix $\mathbf{C}$ is widely used to display the elastic constants. The maximum number of elastic constants is 21, which is required by a general anisotropic body. This number is considerably reduced for media with various symmetries. The non-zero constants of the more symmetric models used in this thesis are given below.

Isotropic-2 independent constants:

$$\mathbf{C} = \begin{bmatrix} \lambda+2\mu & \lambda & \lambda & 0 & 0 & 0 \\ \lambda & \lambda+2\mu & \lambda & 0 & 0 & 0 \\ \lambda & \lambda & \lambda+2\mu & 0 & 0 & 0 \\ 0 & 0 & 0 & \mu & 0 & 0 \\ 0 & 0 & 0 & 0 & \mu & 0 \\ 0 & 0 & 0 & 0 & 0 & \mu \end{bmatrix}, \tag{2.26}$$

where λ and μ are Lamé constants.

Transversely isotropic-5 independent constants:

$$\mathbf{C} = \begin{bmatrix} c_{11} & c_{12} & c_{13} & 0 & 0 & 0 \\ c_{12} & c_{11} & c_{13} & 0 & 0 & 0 \\ c_{13} & c_{13} & c_{33} & 0 & 0 & 0 \\ 0 & 0 & 0 & c_{44} & 0 & 0 \\ 0 & 0 & 0 & 0 & c_{44} & 0 \\ 0 & 0 & 0 & 0 & 0 & c_{66} \end{bmatrix}, \tag{2.27}$$

with $c_{12} = c_{11} - 2c_{66}$.

2.3 Wave equations

In the previous sections, we have reviewed the concepts of stress and strain, and the relation between them. We now introduce the equation of motion which is valid for any continuum—fluid or solid. Combining this equation with the constitutive relations, we then derive acoustic and elastic wave equations.

2.3.1 Equation of motion

Consider a particle of arbitrary shape, with volume δV and surface area δS. The forces associated with its acceleration are a body force $\mathbf{f}\delta V$ and traction forces $\mathbf{t}(\mathbf{n})\delta S$.

Newton's Law then states that

$$\int_{\delta S} \mathbf{t}(\mathbf{n})\, dS + \int_{\delta V} \mathbf{f}\, dV = \int_{\delta V} \rho \frac{\partial^2 \mathbf{u}}{\partial t^2}\, dV, \tag{2.28}$$

where ρ is the density of the medium.

Applying (2.6) and the divergence theorem to the surface integral in (2.28) gives:

$$\int_{\delta S} \mathbf{t}(\mathbf{n})\, dS = \int_{\delta S} \boldsymbol{\sigma} \cdot \mathbf{n}\, dS = \int_{\delta V} \nabla \cdot \boldsymbol{\sigma}\, dV. \tag{2.29}$$

Using this equation, (2.28) becomes:

$$\int_{\delta V} (\nabla \cdot \boldsymbol{\sigma} + \mathbf{f})\, dV = \int_{\delta V} \rho \frac{\partial^2 \mathbf{u}}{\partial t^2}\, dV, \tag{2.30}$$

If the particle volume is sufficiently small, the integrands of the volume integrals in (2.30) are essentially constant, hence

$$\rho \frac{\partial^2 \mathbf{u}}{\partial t^2} = \nabla \cdot \boldsymbol{\sigma} + \mathbf{f}. \tag{2.31}$$

This is the equation of motion which is valid for any continuum—fluid or solid. It also can be written as:

$$\rho \frac{\partial^2 u_i}{\partial t^2} = \frac{\partial \sigma_{ij}}{\partial x_j} + f_i. \tag{2.32}$$

2.3.2 Acoustic wave equation

Acoustic waves are pressure waves in a fluid. Substituting for the stress tensor (2.13) in the equation of motion (2.31) and set body force $\mathbf{f}$ equal to zero, we obtain:

$$\frac{\partial \mathbf{v}}{\partial t} = -\frac{1}{\rho} \nabla p. \tag{2.33}$$

where $\mathbf{v}$ is the particle velocity.

The constitutive relation (2.14) can be rewritten as:

$$\frac{\partial p}{\partial t} = -K\nabla \cdot \mathbf{v}. \tag{2.34}$$

Replacing the bulk modulus K by the acoustic velocity c and the fluid density ρ according to $K = \rho c^2$, equation (2.34) becomes:

$$\frac{\partial p}{\partial t} = -\rho c^2 \nabla \cdot \mathbf{v}. \tag{2.35}$$

Taking the divergence of equation (2.33), differentiating equation (2.35) with respect to t, and subtracting to eliminate $\mathbf{v}$, we get one single partial differential equation:

$$\frac{1}{\rho c^2}\frac{\partial^2 p}{\partial t^2} - \nabla \cdot (\frac{1}{\rho}\nabla p) = 0. \tag{2.36}$$

This is the 3-D acoustic wave equation for small amplitude waves in a fluid with spatial variations in both density and wave velocity.

For a medium with constant density, equation (2.36) is reduced to:

$$\frac{1}{c^2}\frac{\partial^2 p}{\partial t^2} - \nabla^2 p = 0, \tag{2.37}$$

which is the familiar wave equation for acoustic waves in a constant density medium.

2.3.3 Elastic wave equation

Elastic waves propagate in a solid. Different forms of the elastic wave equation can be obtained by combining the equation of motion and the constitutive relation. To clearly demonstrate this, we consider an isotropic elastic medium.

Navier wave equation

Setting f_i equal to zero, the equation of motion (2.32) becomes:

$$\rho\frac{\partial^2 u_i}{\partial t^2} = \frac{\partial \sigma_{ij}}{\partial x_j}. \tag{2.38}$$

With the stiffness matrix (2.26), the constitutive relation for an isotropic elastic medium can be written as:

$$\sigma_{ij} = \lambda\theta\delta_{ij} + 2\mu\epsilon_{ij}, \tag{2.39}$$

where θ is the dilatation (2.11).

Using (2.9) and (2.10), equation (2.39) becomes:

$$\sigma_{ij} = \lambda\theta\delta_{ij} + \mu(\frac{\partial u_i}{\partial x_j} + \frac{\partial u_j}{\partial x_i}). \tag{2.40}$$

Using this to substitute the stress in the equation of motion (2.38), we get the elastic wave equation involving only displacement

$$\rho\frac{\partial^2 u_i}{\partial t^2} = (\lambda + \mu)\frac{\partial \theta}{\partial x_i} + \mu\nabla^2 u_i, \tag{2.41}$$

which is called the Navier wave equation. The FD algorithm solution of this second order system of equations is on a single grid.

Velocity-stress wave equation

Using particle velocity rather than displacement, the equation of motion (2.38) becomes

$$\rho\frac{\partial v_i}{\partial t} = \frac{\partial \sigma_{ij}}{\partial x_j}, \tag{2.42}$$

and the constitutive relation (2.40) becomes

$$\frac{\partial \sigma_{ij}}{\partial t} = \lambda\frac{\partial v_k}{\partial x_k} + \mu(\frac{\partial v_i}{\partial x_j} + \frac{\partial v_j}{\partial x_i}). \tag{2.43}$$

These two equations generate a coupled system

$$\begin{cases} \rho\dfrac{\partial v_i}{\partial t} = \dfrac{\partial \sigma_{ij}}{\partial x_j}, \\ \dfrac{\partial \sigma_{ij}}{\partial t} = \lambda\dfrac{\partial v_k}{\partial x_k} + \mu(\dfrac{\partial v_i}{\partial x_j} + \dfrac{\partial v_j}{\partial x_i}), \end{cases} \tag{2.44}$$

which is called the velocity-stress wave equation. This first order system of equations can be solved by staggered grid FD algorithms in both space and time domains

(Virieux, 1984, 1986; Levander, 1988; Graves, 1996).

Displacement-stress wave equation

The coupled displacement-stress wave equation can be easily obtained by combining the equation of motion (2.38) with the constitutive relation (2.40):

$$\begin{cases} \rho \dfrac{\partial^2 u_i}{\partial t^2} = \dfrac{\partial \sigma_{ij}}{\partial x_j}, \\ \sigma_{ij} = \lambda \dfrac{\partial u_k}{\partial x_k} + \mu(\dfrac{\partial u_i}{\partial x_j} + \dfrac{\partial u_j}{\partial x_i}). \end{cases} \tag{2.45}$$

Solving this system by FD method involves a staggered grid scheme only in space. In this system, the differencing formula for stress can be plugged into the differencing formula for displacement to yield a formula in terms of displacement only (Luo and Schuster, 1990). Thus, this system requires less computer memory than the velocity-stress system by storing only displacement components, not stress components.

Chapter 3

Efficient FD techniques

To efficiently model wave propagation in multi-scale heterogeneous media, we developed an optimized variable grid FD scheme to approximate the first spatial derivatives in wave equations, and developed a variable timestep FD scheme for time marching. The use of the variable grid and timestep FD techniques results in great savings in both computer memory and CPU time. In this chapter, we present these techniques and their accuracy and efficiency in detail.

3.1 Introduction

Conventional FD methods use a constant grid and timestep throughout the entire domain for seismic modeling. While the constant grid and timestep FD schemes are easy to implement (Kelly et al., 1976; Virieux, 1984, 1986; Levander; 1988; Graves, 1996), they lead to intensive computational cost for geological models with multi-scale heterogeneities (e.g. Figure 1.1). To resolve small-scale features such as boreholes or/and fractures which are often 2 or 3 orders smaller than the typical seismic wavelength in the medium, a very fine grid spacing is required. Using the fine grid spacing throughout the entire domain requires too much memory and CPU time thereafter for simulation on most computers.

Variable grid FD methods can overcome this problem by allowing fine grid spacing for zones with small-scale features and coarse grid spacing for zones with large structures. However, most variable grid FD schemes developed so far are based on the Taylor series expansion (Moczo, 1989; Jastram and Behle, 1991; Jastram and Tessmer, 1994; Falk et al., 1996; Pitarka, 1999) which may suffer unacceptable dispersion.

We derived an optimized variable grid FD scheme based on the idea of the DRP (dispersion-relation-preserving) scheme proposed by Tam and Webb (1993). The philosophy of the DRP method is to optimize the coefficients of the FD scheme by matching the effective wave number and the actual wave number over a wide range of wave numbers. The optimized variable grid FD scheme has less dispersion errors than the Taylor variable grid FD scheme (Pitarka, 1999); therefore it can lead to either more accurate results or more efficient computations.

The use of variable grid spacing considerably reduces the computer memory requirements and CPU time thereafter for seismic modeling in multi-scale heterogeneous media. However, if a constant timestep is used throughout the entire domain, the simulation is still time consuming. This is due to a very small timestep required by the finest grid spacing in the model to satisfy the FD stability condition. The global use of the small timestep yields temporal oversampling for coarser grids; thus CPU time is wasted.

To further reduce the CPU time in the simulation, we developed a spatially variable timestep FD scheme for a spatial staggered grid based on the method introduced by Tessmer (2000) for a spatial non-staggered grid. A spatial staggered grid is crucial for handling solid-liquid interfaces present in most applications in this thesis (e.g. fracture and borehole modeling in the following chapters). This variable timestep FD scheme is more flexible than the scheme proposed by Falk et al. (1998), because it can handle any integer timestep ratios between two different domains. The use of this variable timestep scheme with the variable grid scheme results in great savings in CPU time.

The following sections present the developed efficient FD techniques and their accuracy and efficiency in detail.

3.2 Efficient FD techniques

3.2.1 Optimized variable grid FD method

The optimized variable grid FD scheme we developed is based on the idea of the DRP scheme (Tam and Webb, 1993). The idea in the DRP scheme is to optimize the coefficients of the FD operator by minimizing the difference between the effective wave number and the actual wave number over a wide range of wave numbers.

We derived an optimized fourth-order variable grid FD operator on a staggered grid mesh to approximate the first spatial derivatives in wave equations. To illustrate the problem, the 1-D displacement-pressure wave equation is considered (because spatial derivatives with respect to x, y and z are decoupled, the 1-D wave equation illustration will not lose generality):

$$\begin{cases} \rho\dfrac{\partial^2 u}{\partial^2 t} = \dfrac{\partial p}{\partial x}, \\ p = K\dfrac{\partial u}{\partial x}, \end{cases} \tag{3.1}$$

where p and u are pressure and displacement, respectively; ρ is density and K is bulk modulus.

Discretizing equation (3.1) in space by a staggered grid FD mesh with variable grid spacing yields the scheme shown in Figure 3.1. Suppose that the field variable g represents displacement u or pressure p. The approximation of the first-order spatial derivative $\partial g/\partial x$ by a fourth-order FD operator on a variable grid of spacing dx_i is given by

$$\frac{\partial g(x)}{\partial x} \approx c_1 g(x+\Delta_1) + c_2 g(x-\Delta_2) + c_3 g(x+\Delta_3) + c_4 g(x-\Delta_4), \tag{3.2}$$

where c_i are the four coefficients to be determined. Spatial increments Δ_i can be expressed in terms of the variable grid spacing dx_i (Figure 3.2).

After Fourier transform of equation (3.2), the effective numerical wave number of

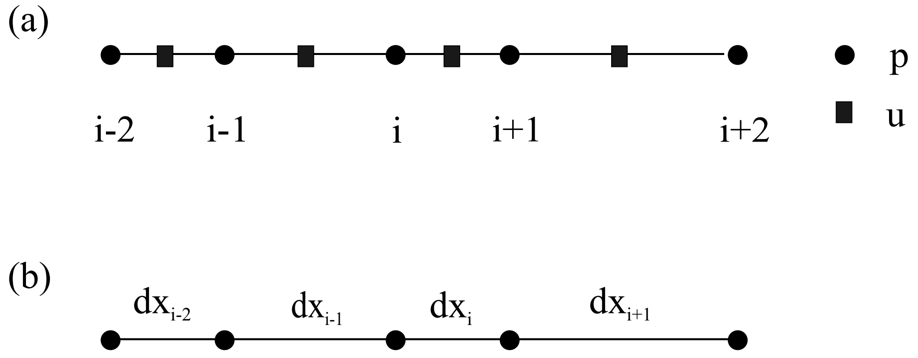

Figure 3.1: 1-D staggered grid mesh with variable grid spacing: (a) unit cells; (b) the variable grid spacing.

the FD scheme can be calculated by

$$k_e = -i(c_1 e^{ik\Delta_1} + c_2 e^{-ik\Delta_2} + c_3 e^{ik\Delta_3} + c_4 e^{-ik\Delta_4}). \tag{3.3}$$

For the optimized FD scheme, c_i in equation (3.3) are chosen so that the effective wave number k_e is close to the actual wave number k for a wide range of wave numbers.

To determine the coefficients c_i, we impose the condition that equation (3.2) is accurate to the third-order of Δ_i through the Taylor series expansion:

$$\begin{cases} c_1 + c_2 + c_3 + c_4 = 0, \\ c_1\Delta_1 - c_2\Delta_2 + c_3\Delta_3 - c_4\Delta_4 = 1, \\ c_1\Delta_1^2 + c_2\Delta_2^2 + c_3\Delta_3^2 + c_4\Delta_4^2 = 0. \end{cases} \tag{3.4}$$

This leaves one of the coefficients, e.g., c_1, as a free parameter. This parameter is then chosen to minimize the integrated error E, defined as

$$E = \lambda \int_0^{\eta} (k - Re(k_e))^2\, dk + (1-\lambda) \int_0^{\eta} (Im(k_e))^2\, dk, \tag{3.5}$$

where η is a predetermined number that gives the optimized range of wave numbers. λ is a weighting coefficient which is used to balance the L_2 norm of the truncation errors of the approximation of the real and imaginary parts of the effective numerical wave number to the actual wave number. The necessary condition used to minimize

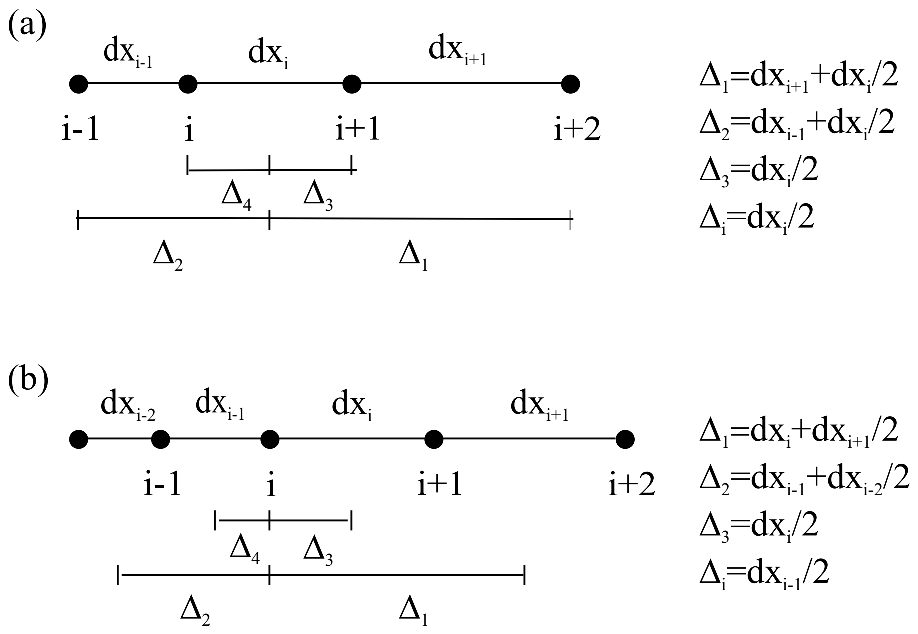

Figure 3.2: Grid nodes with variable spacing. Spatial increments Δ_i (i = 1, 4) are used to calculate the FD operator centered between (a) the nodes i and i+1 and (b) that centered at the node i.

E is

$$\frac{\partial E}{\partial c_1} = 0. \tag{3.6}$$

From equation (3.6), we can get c_1 analytically. Then c_2, c_3, and c_4 can be obtained from equation (3.4). Thus, we get the four coefficients of the optimized fourth-order variable grid FD operator.

To show the advantages of this optimized variable grid FD operator over the same order variable grid FD operator based on the Taylor series expansion (Pitarka, 1999), we compare their spectral properties for different variable grid meshes.

Figure 3.3 shows the relation between $Re(k_e)dx_{min}$ and kdx_{min} of both schemes for the stencil in Figure 3.2(a) with the spacing ratio (r) between the coarse grid size and the fine grid size of 1, 3 and 6. The closer the curves are to the exact relation $Re(k_e)dx_{min} = kdx_{min}$, the smaller the dispersions.

Figure 3.3 demonstrates that the optimized FD scheme has less dispersion errors than the FD scheme based on the Taylor series expansion with the same mesh. In fact, the spectral resolution property of the optimized FD scheme with the grid spacing ratio of 6 is much better than that of the Taylor variable grid FD scheme of the same stencil and is even close to that of the Taylor regular grid FD scheme (spacing ratio of 1). This means that the optimized variable grid FD scheme with large spacing ratios between two grid size domains can give the same accurate results as the Taylor variable grid FD scheme with small spacing ratios. Therefore, the optimized variable grid FD technique can lead to either more accurate results with the same grid points or more efficient computations with the less grid points compared to the Taylor variable grid FD method.

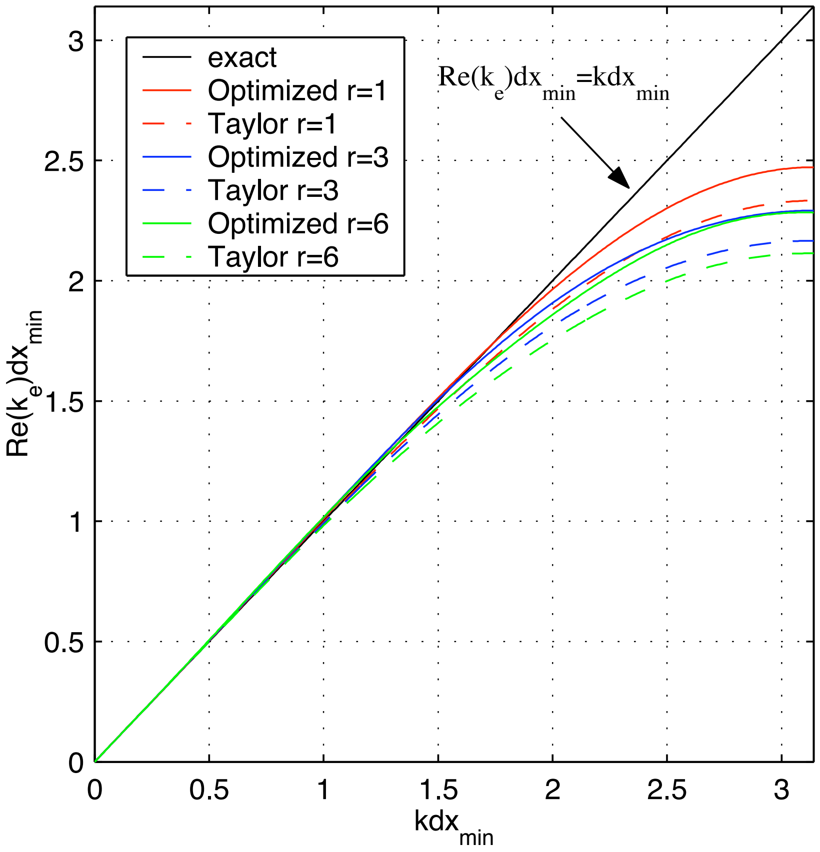

Figure 3.3: $Re(k_e)dx_{min}$ versus kdx_{min} of the optimized and Taylor variable grid FD schemes for the stencil in Figure 3.2(a). r represents the ratio of the coarse grid spacing to the fine grid spacing. The exact relation is $Re(k_e)dx_{min} = kdx_{min}$.

3.2.2 Variable timestep FD method

The variable timestep FD method we developed is based on the staggered grid FD scheme for the displacement-stress wave equation (2.45). To clearly illustrate the method, we consider the 1-D case.

Solution of wave equation

Equation (3.1) is the 1-D displacement-pressure wave equation. After discretization in time, we replace the temporal derivative in equation (3.1) by the second-order central FD operator. For a timestep of Δt, the solution of this system of equations can be written as:

$$\begin{cases} u^{n+1} = -u^{n-1} + 2u^n + \dfrac{(\Delta t)^2}{\rho}\dfrac{\partial p^n}{\partial x}, \\ p^{n+1} = K\dfrac{\partial u^{n+1}}{\partial x}. \end{cases} \tag{3.7}$$

where the superscripts refer to the time index.

The time stepping defined by equation (3.7) is done iteratively from one time level to the next. At time level $t = n\Delta t$, the algorithm is: (1) update displacement u at the following time level $(n+1)\Delta t$ using the values of u at the present and previous time levels $n\Delta t$ and $(n-1)\Delta t$ plus the spatial derivative $\partial p/\partial x$ at the present time level $n\Delta t$; (2) update pressure p at time level $(n+1)\Delta t$ using the spatial derivative $\partial u/\partial x$ at the same time level $(n+1)\Delta t$. The spatial derivatives ($\partial p/\partial x$ and $\partial u/\partial x$) are calculated by the fourth-order staggered grid FD operator developed in the previous section.

Variable timestep FD scheme

Based on equation (3.7), we developed a spatially variable timestep FD scheme which can handle any integer ratios of timesteps used in two spatial domains. I use an example to illustrate the method.

Figure 3.4 shows two different timesteps used in two domains of a 1-D spatial staggered grid. A large timestep of $3\Delta t$ is used in Domain 1 and a small timestep of Δt is used in Domain 2. The ratio of the large timestep to the small timestep is

3. The dashed black line represents the boundary separating the two domains with different timesteps.

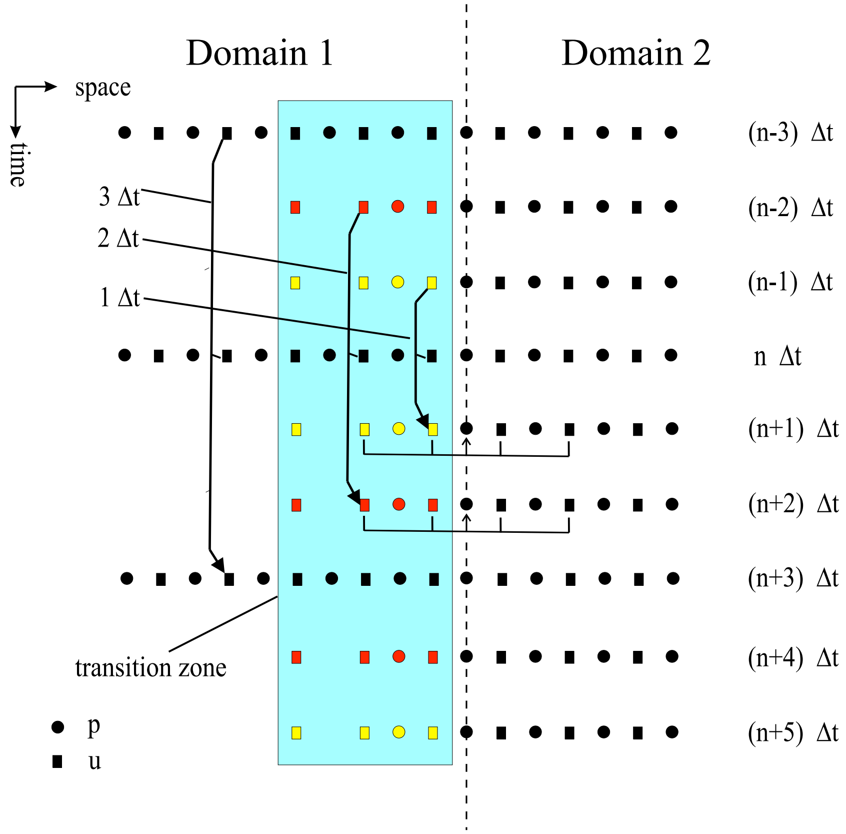

Figure 3.4: Time stepping scheme with spatially variable timesteps for a 1-D spatial staggered grid. The timestep of $3\Delta t$ used in Domain 1 (left) is three times greater than the timestep of Δt used in Domain 2 (right). Symbols with yellow and red colors represent intermediate wavefield values in the transition zone (blue shaded area).

When time stepping with different timesteps in two spatial domains is performed, difficulties are encountered for the calculation of the spatial derivatives by the fourth-order FD operator on or around the boundary between the two domains. A spatial derivative at a grid point is calculated from the wavefield values at four grid points symmetrically around it (see Figure 3.4). However, due to the change of timesteps, the wavefield values required by the spatial derivatives on or around the domain boundary do not exist at certain time levels. For example, to calculate the spatial derivative $\partial u/\partial x$ on the boundary at time levels of $(n+1)\Delta t$ and $(n+2)\Delta t$, we need wavefield values of u beyond the boundary at the same time levels (Figure 3.4). Thus, the critical issue for a variable timestep FD scheme is how to provide the wavefield values within a transition zone (blue shaded area in Figure 3.4).

We calculate the wavefield values within the transition zone at intermediate time levels by the same time stepping scheme (equation (3.7)) used in the computational domain but with different timesteps. For example, we update the displacements in the transition zone at time levels of $(n+1)\Delta t$ and $(n+2)\Delta t$ (yellow and red squares in Figure 3.4) with timesteps of Δt and $2\Delta t$, respectively. The advantage of this multiple time stepping method is that the calculated wavefield values within the transition zone have the same order accuracy as those in the computational domain.

Therefore, our variable timestep FD scheme uses the same time stepping formula (equation (3.7)) throughout the entire model. The only difference is that the timesteps used in different domains and transition zones are different.

Now we start at time level $n\Delta t$ to demonstrate the procedure of time stepping for the variable timestep FD scheme shown in Figure 3.4:

(1) Update the displacement in Domain 1 (large timestep domain) at time level $(n+3)\Delta t$ from the displacement at time levels $n\Delta t$ and $(n-3)\Delta t$, and the pressure at time level $n\Delta t$.

(2) Calculate the displacement in the transition zone at intermediate time levels (yellow and red squares). This is done by updating the displacement at $(n+1)\Delta t$ and $(n+2)\Delta t$ with timesteps of Δt and $2\Delta t$, using time levels $n\Delta t$ and $(n-1)\Delta t$ and time levels $n\Delta t$ and $(n-2)\Delta t$, respectively. These wavefield values are needed for the time stepping in Domain 2 (small timestep domain).

(3) Perform time stepping in Domain 2 with the small timestep of Δt until time level $(n+3)\Delta t$ is reached. At each timestep, we first update the displacement at the following time level in Domain 2; we then update the pressure in both the transition zone and Domain 2 to the same time level.

(4) Update the pressure in Domain 1 at time level $(n+3)\Delta t$ from the displacement at the same time level. This calculation needs the displacement values in Domain 2.

After steps (1)-(4), we get all wavefield values (both displacement and pressure) at time level $(n+3)\Delta t$. Repeat steps (1)-(4) after incrementing the timestep of $3\Delta t$.

While the timestep ratio between the large timestep and the small timestep of 3 is used in the example, this variable timestep FD scheme can handle any integer timestep ratios between different domains. Also, the width of the transition zone, which is determined by the length of the spatial FD operator, is independent of the timestep ratios. The constant width of the transition zone is very narrow (e.g. four grid points for the fourth-order spatial staggered grid scheme); thus the computer memory and CPU time required by the intermediate wavefield values within the transition zone are negligible.

3.3 Accuracy and efficiency

To test the accuracy and efficiency of the developed techniques, we compare the numerical results and the computational costs of the variable grid, and the variable grid and timestep FD methods with those of the constant grid and timestep FD method.

The simulations are performed for a 108 m × 108 m 2-D homogeneous model with the physical properties of V_p=3000 m/s, V_s=1732 m/s, ρ=2100 kg/m^3. Figure 3.5 shows the grid spacing and timesteps used for the simulations by the constant grid and timestep FD method (Figure 3.5a), the variable grid FD method (Figure 3.5b), and the variable grid and timestep FD method (Figure 3.5c). The two dashed lines (at x=40.5 m and x=67.5 m, respectively) in Figure 3.5b and 3.5c represent the artificial boundaries at the change of grid spacing and the change of both grid spacing and timesteps. The ratio of the coarse grid spacing to the fine grid spacing is 3 in both Figure 3.5b and 3.5c. The timestep ratio of the large timestep to the small timestep in Figure 3.5c is 3. An explosive source S(54 m, 54 m), which has a Ricker pulse with central frequency of 500 Hz, is used for the three simulations. Two receivers R_1(41.4 m, 51.84 m) and R_2(39.69 m, 51.84 m) are placed on each side of the artificial boundary at x=40.5 m (see Figure 3.5b and 3.5c) to measure the reflections and transmissions, respectively.

Figure 3.6 shows the wavefield snapshots of the horizontal displacement component at 15 ms of the simulations by the constant grid and timestep FD method (left column panel), the variable grid FD method (middle column panel), and the variable grid and timestep FD method (right column panel). For each column panel, the snapshots from the top to the bottom are the same results but displayed with different ranges of the amplitude. On the top, the amplitude range is from -100 to 100, taken to be 100 %; in the middle, the range is from -1 to 1 which is 1 %; and on the bottom, it is from -0.1 to 0.1 which is 0.1 %. Comparison of these snapshots shows that the effects caused by the change of grid spacing (middle panel) and the change of both grid spacing and timesteps (right panel) are less than 0.1 %.

The comparison of the wavefield snapshots of the vertical displacement component at 15 ms of the three simulations is shown in Figure 3.7. We can see that the artificial effects caused by the change of grid spacing, and the change of both grid spacing and timesteps are less than 0.1 %, too.

Figure 3.8 and 3.9 present the comparisons of the seismograms of the horizontal and vertical displacements (U_x and U_z) computed by the constant grid and timestep, the variable grid, and the variable grid and timestep FD methods at receiver R_1 and R_2, respectively. The fit among the results of the three simulations is excellent. We then calculate the corresponding differences due to the change of the grid spacing, and the change of both grid spacing and timesteps at R_1 and R_2, which are shown in Figure 3.10 and 3.11, respectively. We can see that the artificial reflections observed at R_1 and the artificial transmissions observed at R_2 are all less than 0.1 %. These results quantitatively demonstrate the high accuracy of the developed variable grid and variable timestep FD techniques.

The simulations were carried out on a 1.4 GHz Athlon computer with 1 GB DDR RAM. The memory and CPU time required by the three methods are listed in Table 3.1 for comparison.

Compared to the oversampled constant grid and timestep FD method, the variable grid FD method saves 43 % memory and 54 % CPU time, and the variable grid and timestep FD method saves 42 % memory and 71 % CPU time with comparable accuracy. Compared to the variable grid FD method, the variable grid and timestep FD method further reduces CPU time of 17 % with almost the same memory requirement. The comparison shows that the use of the variable grid and variable timestep

FD techniques greatly saves both memory requirements and CPU time.

The efficiency of the developed techniques depends on the simulation model. For more realistic multi-scale problems, such as borehole seismic modeling in the following chapters, higher efficiency can be achieved.

	Const. dx and dt nx×nz=1201×401 dt=.008 ms nt=3000	Varied dx and Const. dt nx×nz=601×401 dt=.008 ms nt=3000	Varied dx and dt nx×nz=601×401 dt=.008/.024 ms nt=3000/1000
Memory (Mb)	20	11.5 (save 43 %)	11.6 (save 42 %)
CPU (min)	24	11 (save 54 %)	7 (save 71 %)

Table 3.1: Computer memory and CPU time required by the simulations of the constant grid and timestep, variable grid, and variable grid and timestep FD methods for a homogeneous model.

3.4 Conclusions

In this chapter, we presented a new variable grid and timestep FD method for efficient seismic modeling in multi-scale heterogeneous media.

The developed optimized variable grid FD scheme has less dispersion errors than the variable grid FD scheme based on the Taylor series expansion; therefore it can lead to either more accurate results or more efficient computations.

The developed variable timestep FD scheme for a spatial staggered grid has a narrow constant width of the transition zone for any integer timestep ratios between different domains; thus the computer memory and CPU time required by the intermediate wavefield values within the transition zone are negligible.

Numerical examples show the high accuracy and efficiency of the variable grid and variable timestep FD techniques. Applications of these techniques for seismic modeling in multi-scale heterogeneous media are presented in the following chapters.

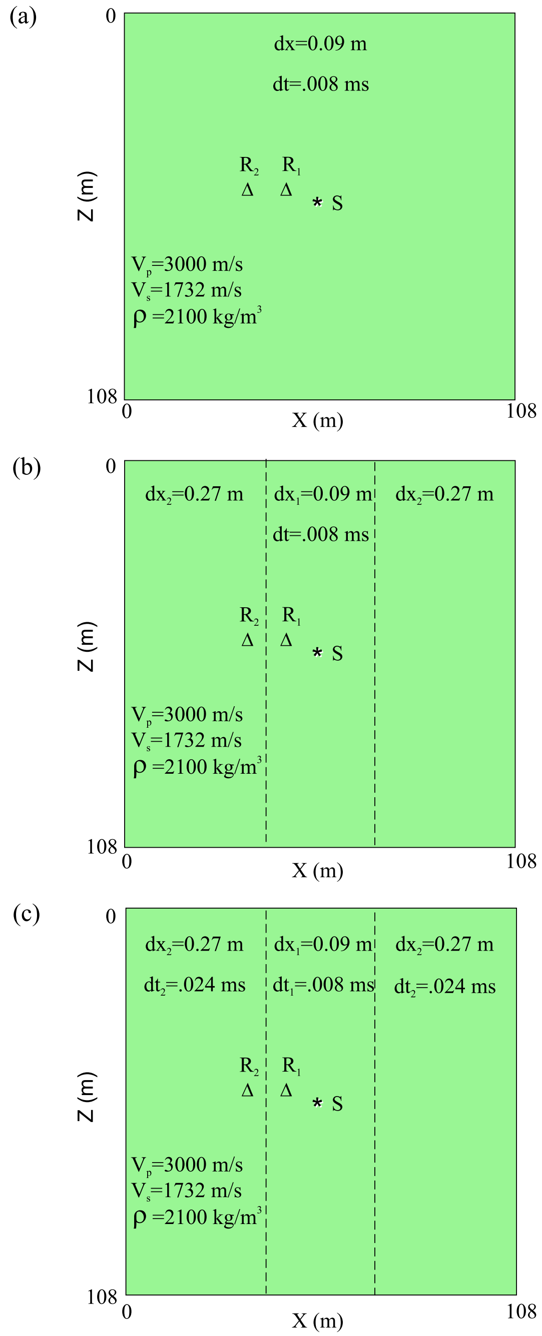

Figure 3.5: Grid spacing and timesteps for the same homogeneous model used for the simulations of the constant grid and timestep FD method (a), the variable grid FD method (b), and the variable grid and timestep FD method (c). The dashed lines in (b) represent the artificial boundaries at the change of grid spacing, and the dashed lines in (c) represent the artificial boundaries at the change of both grid spacing and timesteps.

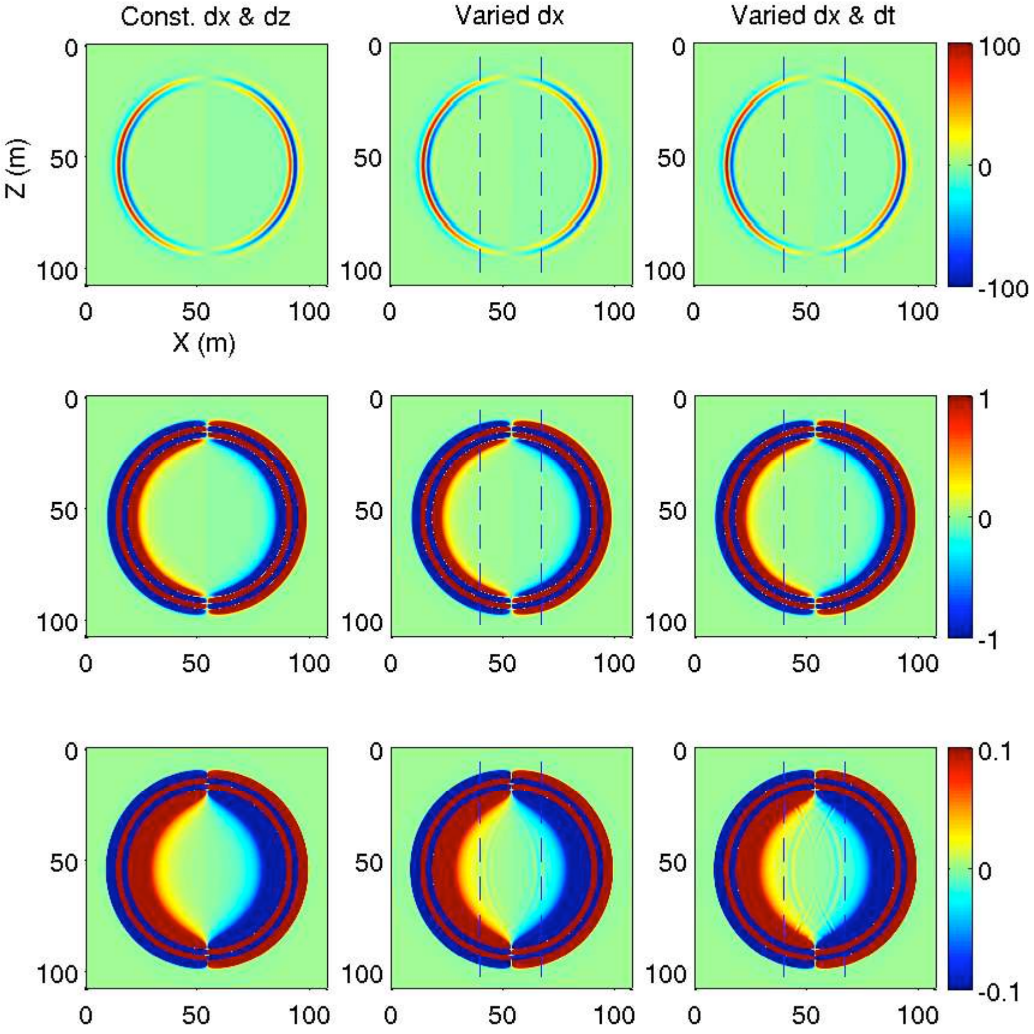

Figure 3.6: Comparison of the horizontal displacement snapshots at 15 ms of the simulations by the constant grid and timestep FD method (left column panel), the variable grid FD method (middle column panel), and the variable grid and timestep FD method (right column panel). For each column panel, the snapshots from the top to the bottom are the same results but displayed with different ranges of the amplitude. Dashed lines represent the artificial boundaries at the change of grid spacing (middle panel) and the change of both grid spacing and timesteps (right panel).

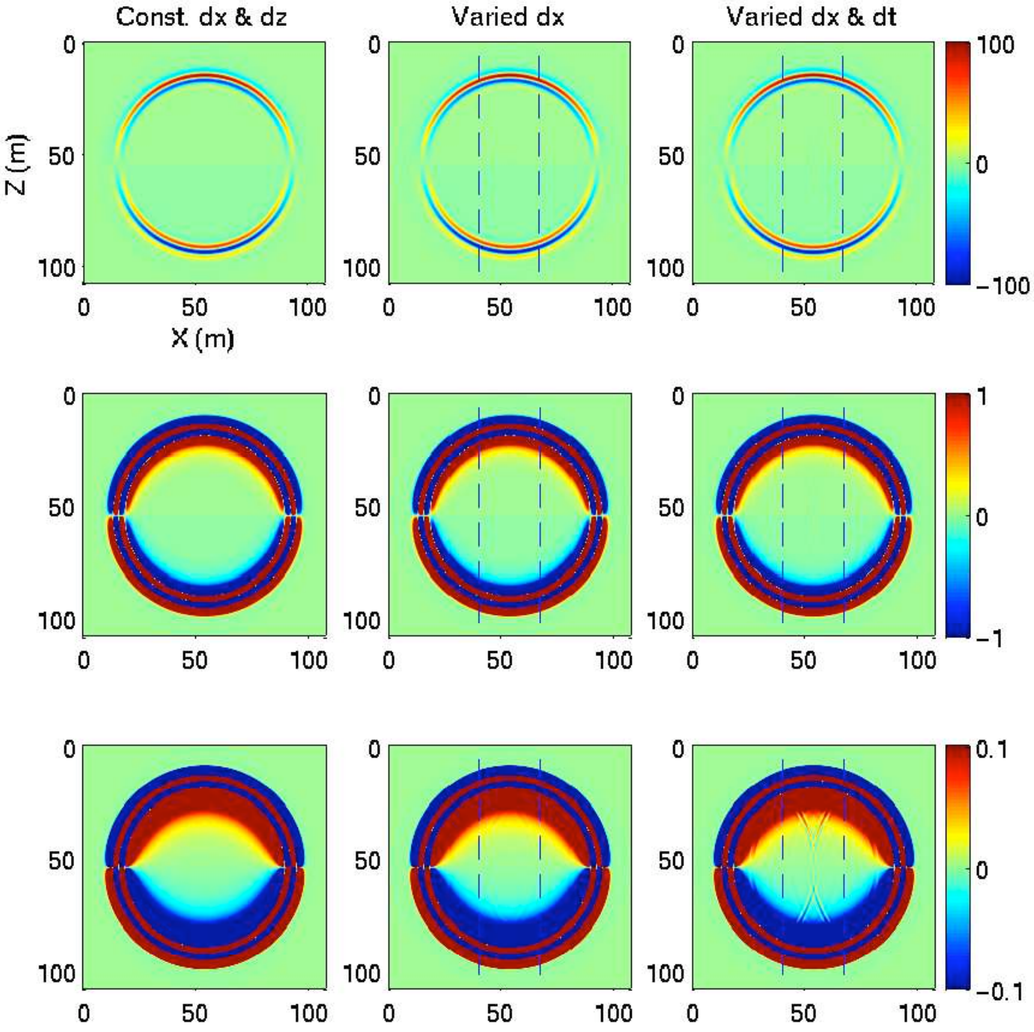

Figure 3.7: Comparison of the vertical displacement snapshots at 15 ms of the simulations by the constant grid and timestep FD method (left column panel), the variable grid FD method (middle column panel), and the variable grid and timestep FD method (right column panel). For each column panel, the snapshots from the top to the bottom are the same results but displayed with different ranges of the amplitude. Dashed lines represent the artificial boundaries at the change of grid spacing (middle panel) and the change of both grid spacing and timesteps (right panel).

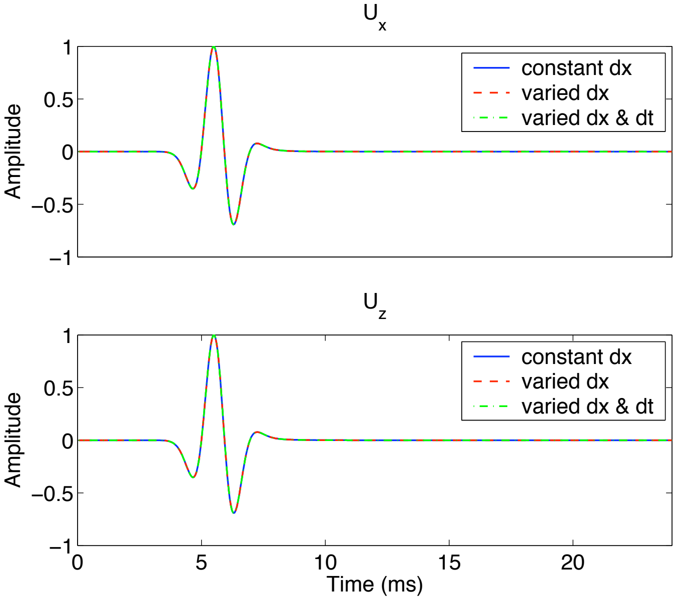

Figure 3.8: Comparison of seismograms of the horizontal and vertical displacements ($\mathrm{U_x}$ and $\mathrm{U_z}$) at receiver $\mathrm{R_1}$ of the simulations by the constant grid and timestep, the variable grid, and the variable grid and timestep FD methods.

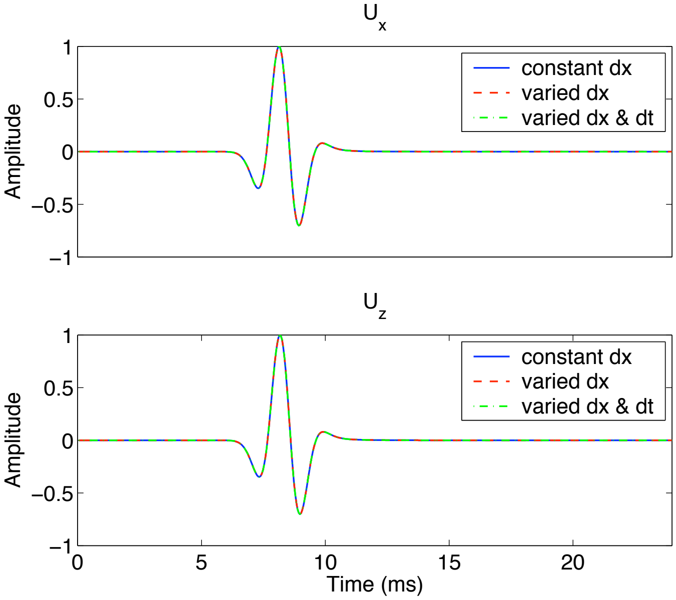

Figure 3.9: Comparison of seismograms of the horizontal and vertical displacements ($\mathrm{U_x}$ and $\mathrm{U_z}$) at receiver $\mathrm{R_2}$ of the simulations by the constant grid and timestep, the variable grid, and the variable grid and timestep FD methods.

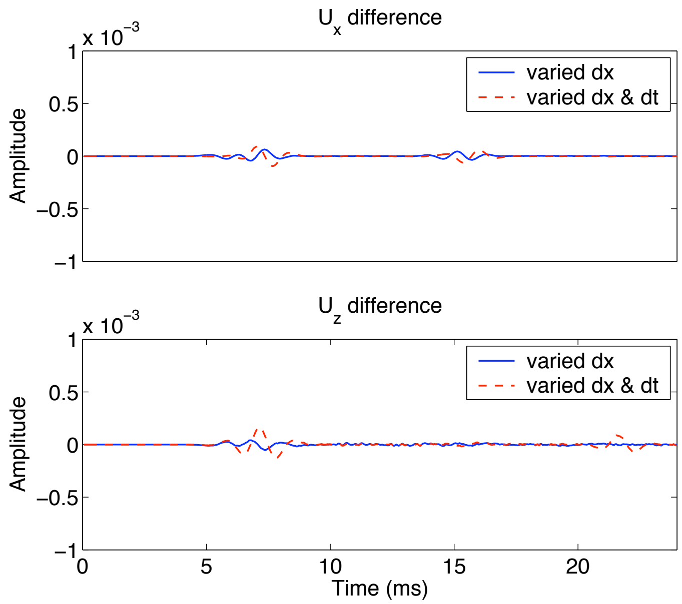

Figure 3.10: The differences of the horizontal and vertical displacements ($\mathrm{U_x}$ and $\mathrm{U_z}$) caused by the change of grid spacing, and the change of grid spacing and timestep at receiver $\mathrm{R_1}$.

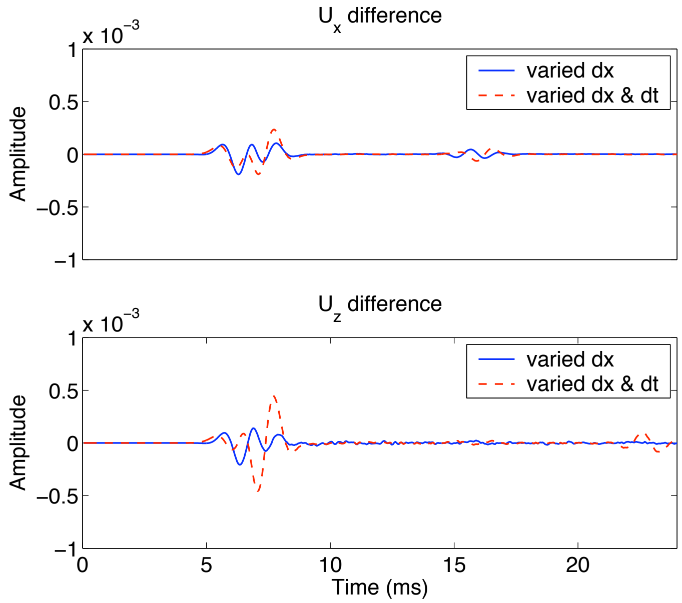

Figure 3.11: The differences of the horizontal and vertical displacements ($\mathrm{U_x}$ and $\mathrm{U_z}$) caused by the change of grid spacing, and the change of grid spacing and timestep at receiver $\mathrm{R_2}$.

Chapter 4

Parallel computing

To efficiently solve large realistic problems, such as borehole seismic field data modeling, we have implemented the parallel 2-D/3-D variable grid FD algorithms for computing on a “Linux Beowulf” cluster. In this chapter, we use the 3-D case to illustrate the parallel implementation. The accuracy and the performance of the 3-D parallel algorithm are tested by numerical examples.

4.1 Introduction

The developed variable grid and variable timestep FD techniques described in chapter 3 make modeling of wave propagation in multi-scale heterogeneous media feasible. However, for real problems with large size, e.g. cross-well field data modeling with the survey geometry (see chapter 7), simulations are still computationally intensive. It is very difficult or impossible to perform such realistic-sized modeling on a single-processor machine except for the large and expensive SMP (Share Memory Processor). Since low-cost networked PC clusters (Beowulf clusters) are now widely available and FD algorithms are well suited for distributed parallelization, it is desirable to develop a parallel version of the algorithm for efficient solution of large problems.

There have been several parallel implementations of FD seismic modeling algorithms on memory distributed computers. Ewing et al. (1994) for example, showed results of a PVM (Parallel Virtual Machine) implementation of 2-D acoustic and elastic FD seismic modeling in a homogeneous dedicated cluster of IBM RS/6000 computers. Villarreal and Scales (1997) presented a distributed 3-D FD acoustic modeling algorithm using the PVM message-passing library, and showed the performance of the algorithm on two different distributed memory architectures, the IBM SP2 and a network of low-cost PCs running the Linux operating system. Xu and McMechan (1998) performed distributed 3-D viscoelastic modeling on an Intel ipsc860.

In this work, we have developed parallel 2-D/3-D variable grid FD elastic modeling codes for more efficient computations of large problems on a "Linux Beowulf" cluster. The parallelization strategy is spatial domain decomposition. We divide a 2-D/3-D full computational grid into subdomains and assign these subdomains to separate processors. Wavefield calculations within each subdomain/processor take place concurrently. Interprocessor data communication uses the MPI (Message Passing Interface) library. Here, we only present the 3-D implementation since the 2-D implementation is just a simpler case of the 3-D in both domain decomposition and data communication. We use numerical examples to show the accuracy and performance of the 3-D parallel algorithm.

4.2 Beowulf cluster and MPI

4.2.1 Beowulf cluster

Cluster is a widely-used term meaning independent computers combined into a unified system through software and networking. At the most fundamental level, when two or more computers are used together to solve a problem, it is considered a cluster. Clusters are typically used for high performance computing to provide greater computational power than a single computer can provide.

Beowulf cluster is scalable performance cluster built primarily out of commodity hardware, running a free-software operating system like Linux or FreeBSD, interconnected by a private system network. The designer can improve performance proportionally with added machines. The commodity hardware can be any of a number of mass-market, stand-alone compute nodes as simple as two networked computers each running Linux and sharing a file system or as complex as 1024 nodes with a high-speed, low-latency network.

Recently, Beowulf clusters have become increasingly popular because they provide a very cost-effective parallel computing environment. A 16 node "Linux Beowulf" PC cluster has been built in the Geophysics Department at Stanford University (see Figure 4.1). Each PC in the cluster has one 1.4/1.6 GHz Athlon processor and 1 GB DDR RAM. The 16 PCs are connected via a 100 Mbps switch. We use this cluster to test the parallel implementation of the variable grid FD algorithm.

Figure 4.1: A 16-node Beowulf PC cluster built in the Geophysics Department at Stanford University.

4.2.2 MPI (Message Passing Interface)

Message passing is the most widely used parallel programming model for distributed memory computers. In this model, a parallel program is executed by multiprocessors concurrently, and each processor can access its own data as well as the data in other processors by sending/receiving messages (Figure 4.2).

MPI is a library specification for message passing. It is becoming the new international standard for parallel programming and is replacing others, such as PVM (Parallel Virtual Machine). MPI was designed for high performance on both massively parallel machines and on workstation clusters and it provides source-code portability of message passing programs across a variety of architectures. The MPI library operates in FORTRAN, C or C++ languages. We use the message passing library MPICH (Gropp et al., 1996), a portable free implementation of MPI under different UNIX OS's (including Linux) and Windows NT. It has support for MPI standards version 1.0 and 2.0.

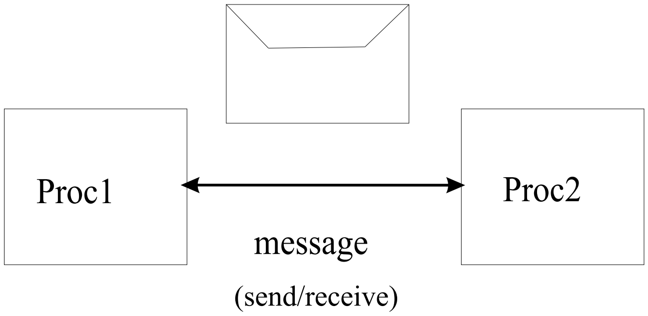

Figure 4.2: Schematic illustration of message passing between two processors (processor 1 and processor 2).

4.3 Method

4.3.1 Sequential algorithm

The sequential algorithm for 3-D variable grid FD modeling of wave propagation is as follows:

```
BEGIN
        -Setup data structures, variables and constants.
        -Read velocity, density, and variable grid spacing.
        FOR every timestep DO
```

```
            FOR every grid point DO
                -calculate the wavefield.
            END
        END
END
```

4.3.2 Parallel implementation

1. Domain decomposition

The parallel implementation of the variable grid FD seismic modeling algorithm is based on domain decomposition. Domain decomposition involves assigning subdomains of the full computational grid to different processors and calculating the wavefield in each subdomain/processor concurrently.

In our implementation, a 3-D computational grid can be partitioned in one, two, or three dimensions. Further, there is no requirement that the number of processors in any one direction must evenly divide the number of grid points. Divisions with remainders are allowed and are transparent to the user. A typical 1-D decomposition is illustrated in Figure 4.3, a 2-D decomposition in Figure 4.4, and a 3-D decomposition in Figure 4.5.

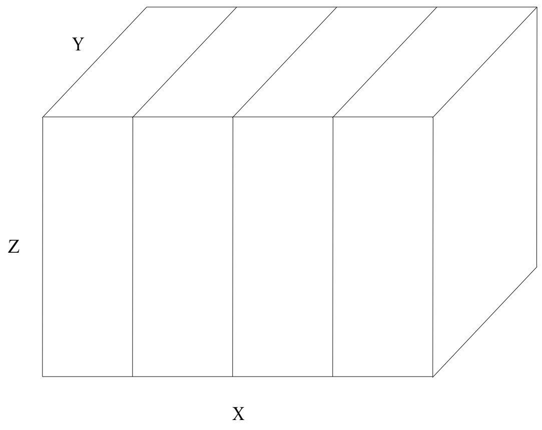

Figure 4.3: 1-D domain decomposition (in the x direction) for parallel computing.

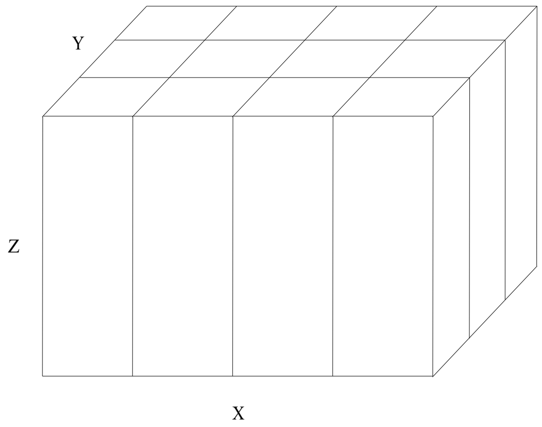

Figure 4.4: 2-D domain decomposition (in the x and y directions) for parallel computing.

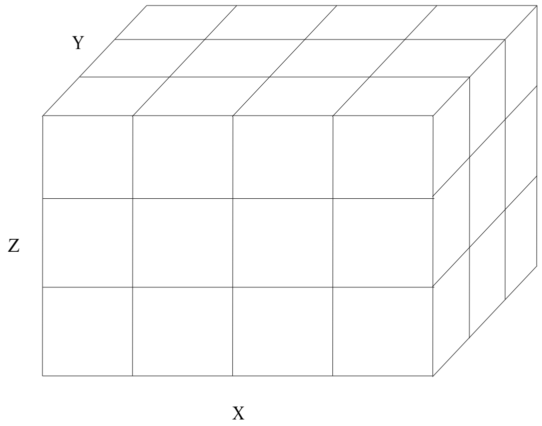

Figure 4.5: 3-D domain decomposition for parallel computing.

Choosing 1-D, 2-D, or 3-D decomposition depends on the number of available processors and the problem size. A proper domain decomposition should equalize load balance and minimize communication time. In a homogeneous multiprocessor environment, the load balancing is assured if all the subdomains are of the same size. Communication is minimized by minimizing the perimeters of the subdomain boundaries.

2. Interprocessor communication

The partitioning of the full computational grid introduces artificial boundaries which are the borders of each subdomain. To calculate the spatial derivatives of

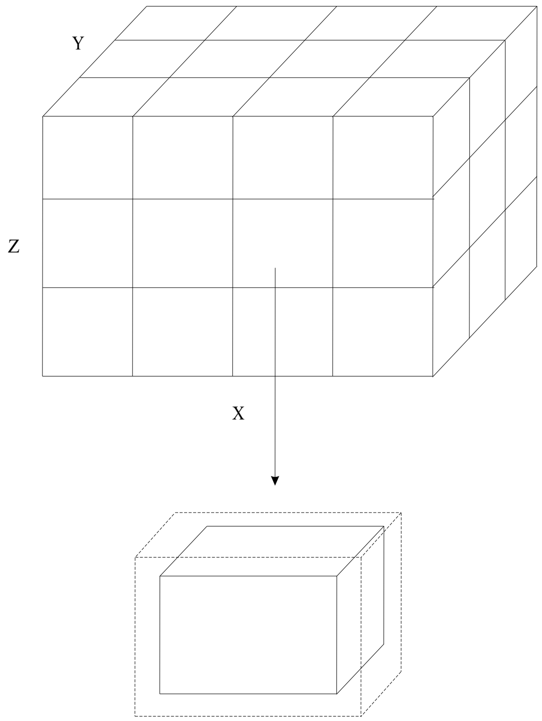

Figure 4.6: Schematic illustration of a subdomain after addition of ghost layers (dashed lines).

wavefield values at a border of a subdomain using a FD operator, wavefield information in the adjacent subdomain is required. This information can be obtained through interprocessor communication.

For the interprocessor communication, padding layers (ghost layers) to each subdomain have to be introduced. (see Figure 4.6 for an illustration of a subdomain after addition of ghost layers). Wavefield information in a subdomain is transferred from the subdomain to the ghost layers of a adjacent subdomain. Figure 4.7 schematically illustrates how this works between two adjacent processors with 2-D view. Every processor sends and receives information to and from its all neighboring processors (up, down, left, right, front, back). The thickness of the padding layer is generally half of the length of the spatial FD operator. For the fourth-order FD scheme we used, the thickness is two grid points. Therefore, two extra planes of memory need to be allocated on each face of a subdomain cube.

The interprocessor communication for data exchange has to be performed at each timestep. The communication is a very expensive operation and long communication time can deteriorate the parallel performance. The communication can be minimized by minimizing the perimeters of the subdomain boundaries. Therefore we need to balance the work load and minimize the communication during domain decomposition of a problem.

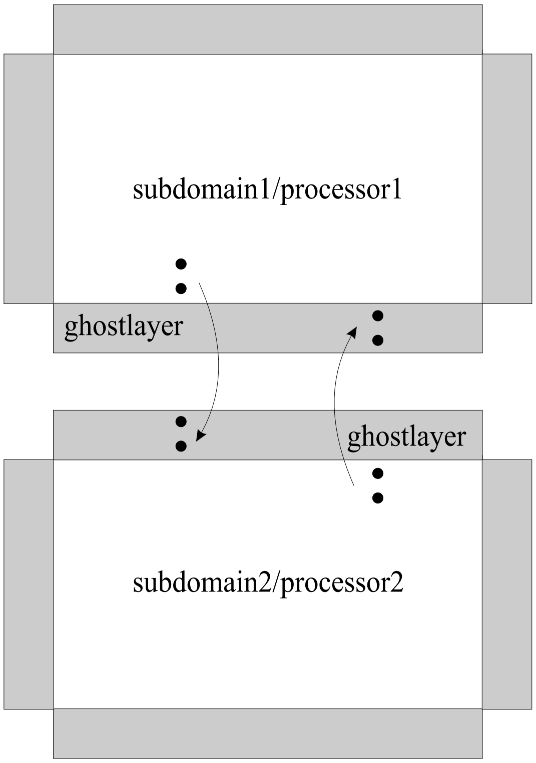

Figure 4.7: Schematic drawing of how ghost layers work for the communication (data exchange) between two adjacent processors. Arrows indicate communication of updated border components. The thickness of the ghost layers required by a fourth-order FD operator is two grid points.

3. A basic algorithm

In summary, the parallel algorithm using the domain decomposition appears as follows:

BEGIN

```
          -Setup data structures, variables and constants.
          -Read velocity, density, and variable grid spacing.
          -Setup the domain decomposition of the grid.
          -Send each subdomain with corresponding
              velocity, density and variable grid spacing.
          FORALL processors simultaneously DO
            FOR every timestep DO
              FOR every grid point DO
                  -calculate the wavefield.
              END
              -interchange wavefield values at borders
               with neighbor processors.
            END
          -Gather wavefield from every processor.
  END
```

This algorithm was implemented on the 16-node “Linux Beowulf” cluster (Figure 4.1) using MPICH library.

4.4 Accuracy and performance

We use numerical examples to test the accuracy and the performance of the developed parallel 3-D FD code.

Figure 4.8 shows the model which is a two-layer 3-D model with dimension of 800 m×800 m×800 m. The interface is in the middle of the model in Z direction. The top layer has $V_p = 3000$ m/s, $V_s = 1732\ m/s$, and $\rho = 1800$ kg/m^3; and the bottom layer has $V_p = 4000\ m/s$, $V_s = 2000\ m/s$, and $\rho = 2200$ kg/m^3. The model is discretized using a 3-D grid containing 201×201×201 grid points. An explosive source, located at (400 m, 400 m, 320 m) which is in the top layer, is used to excite the model. The source function is a Ricker wavelet with a central frequency of 50 Hz.

We performed the simulations for this model on the 16-node “Linux Beowulf” cluster using the sequential code, and using the parallel code with 4, 8, and 15 nodes.

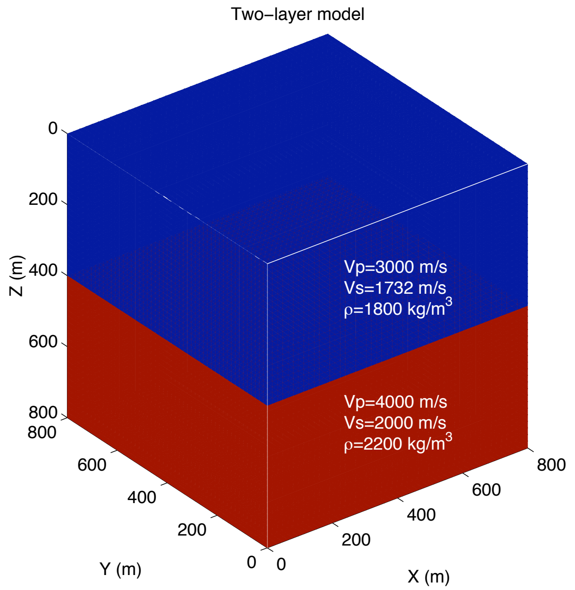

Figure 4.8: A two-layer 3-D model.

To be concise, we do not show all the simulation results here. In fact, the simulation results are identical for the sequential and all parallel runs. This approves the accuracy of the parallel version of the code.

Figure 4.9 shows a 3-D snapshot and corresponding 2-D slices (constant x, y, and z slices) of $\mathrm{V_x}$ component obtained from a parallel run. The interface reflected and transmitted P- and S-waves are clearly seen in the yz-plane (x is constant) and the xz-plane (y is constant) slices. Since the material on xy-plane (z is constant) is homogeneous, we only observe the direct P-wave on the z-plane slice.

Two concepts are used for the performance measurement of parallel computing: speedup and efficiency.

Speedup is defined as the ratio of running time of sequential code to the running time of parallel code:

$$S(n,p) = \frac{T_1(n)}{T_p(n)}, \tag{4.1}$$

where $T_1(n)$ and $T_p(n)$ are the times for running a problem of size n on 1 and p processors, respectively. Speedup is linear if $S(n,p) = p$ (ideal speedup), is superlinear if $S(n,p) > p$, and is sublinear if $S(n,p) < p$. Sublinear speedup is common due to

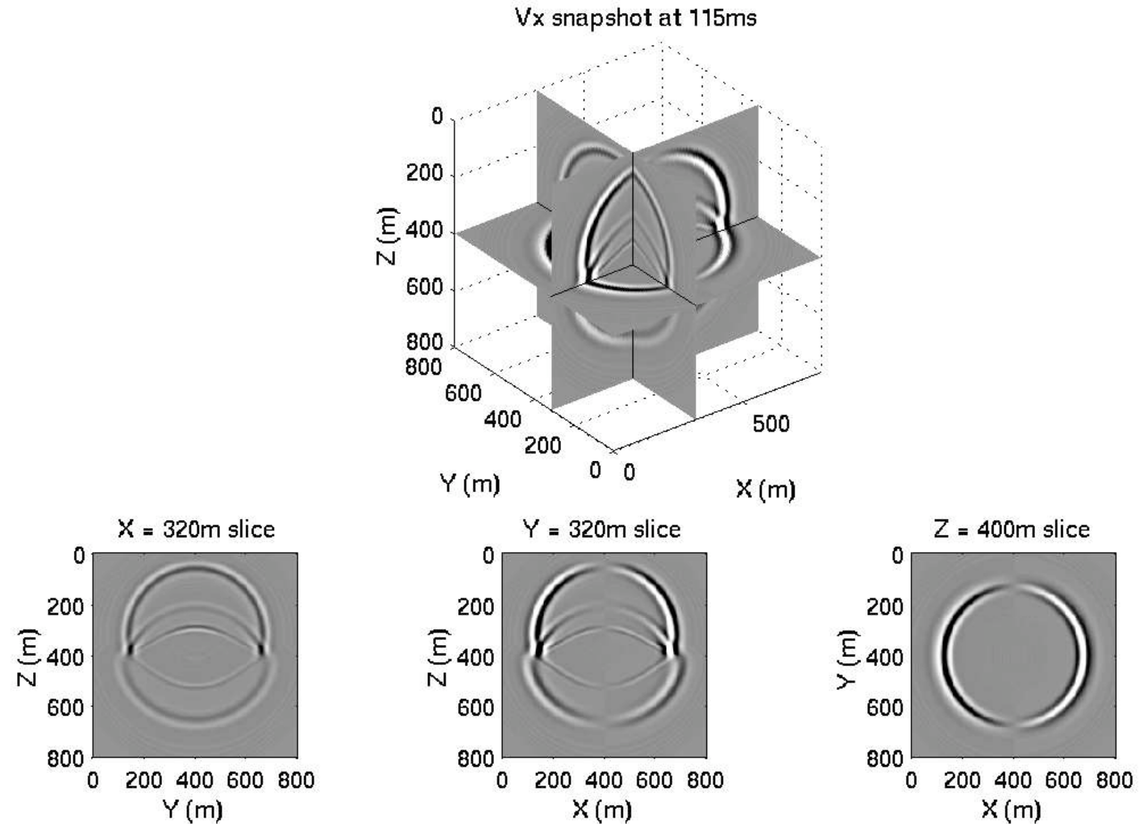

Figure 4.9: $\mathrm{V_x}$ component 3-D snapshots and corresponding 2-D slices of the two-layer 3-D model shown in Figure 4.8.

the presence of sequential code and overhead. Overhead includes costs of starting a process, costs of communication, synchronizing and extra (redundant) computation.

Efficiency is defined as the ratio of speedup to the number of processors:

$$E(n,p) = \frac{T_1(n)}{pT_p(n)}, \tag{4.2}$$

which is a measure of resource utilization in a parallel program, relative to sequential code. Efficiency is 1, greater than 1, and less than 1 for linear, superlinear, and sublinear speedups.

To find the efficiency and speedup of our parallel 3-D FD code, the total time elapsed for the sequential and all the parallel runs are compared (Figure 4.10).

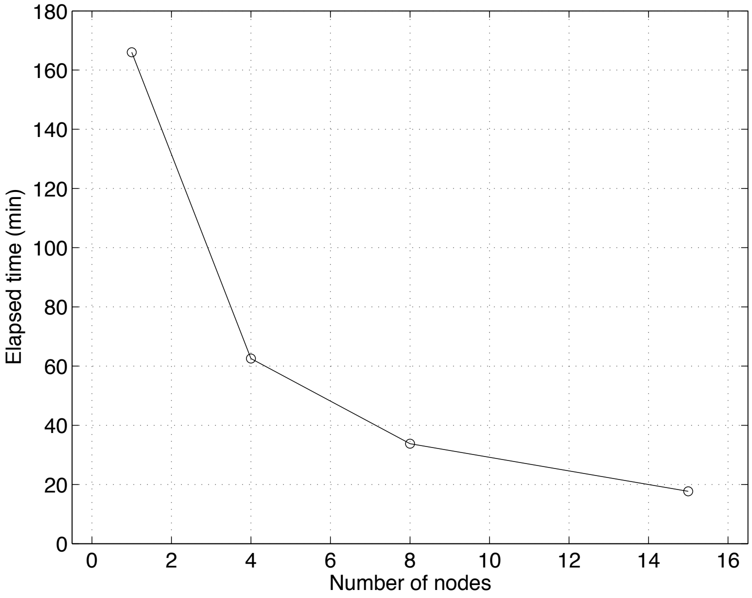

Figure 4.10: Running time of the simulations for model shown in Figure 4.8.

Figure 4.11 shows the speedup curve. The numbers below each point on the speedup curve indicate the efficiency of the parallel code obtained using the number of nodes specified in the horizontal axis. The obtained speedup and efficiency are not very high because the parallel FD algorithm involves a lot of communication and the Ethernet card used in the cluster is slow (100 Mbps). In fact, for this fixed-size problem with 201×201×201 grid points, the efficiency of 0.62 for 15 nodes is very good. With a faster Ethernet card, higher performance of the parallel algorithm can be achieved.

4.5 Conclusions

We have developed parallel 2-D/3-D variable grid FD algorithms based on domain decomposition using the MPI (Message Passing Interface) library. In this chapter, 3-D implementation has been illustrated. Numerical examples show the accuracy and performance of the parallel algorithm. The 2-D parallel variable grid FD code is used for efficiently modeling cross-well field data with the survey geometry (see chapter

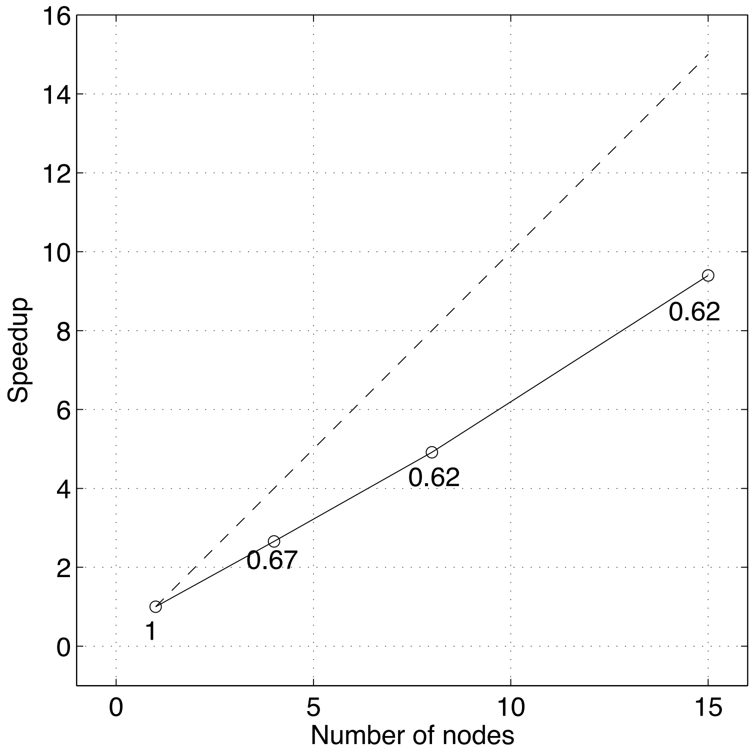

Figure 4.11: Speedup and efficiency for the simulations of the model shown in Figure 4.8. The solid curve is the speedup curve. The numbers below each point on the solid curve indicate the efficiency of the parallel code obtained using the corresponding number of nodes on the horizontal axis. Dashed line is linear speedup.

7). And, the 3-D parallel code is applied for San Juan Basin 9-component VSP field data modeling (not in this thesis).

Chapter 5

Modeling an open fluid-filled fracture

—comparison of thin-layer and linear-slip models

Fractures can be described as thin layers or linear slip interfaces. In this chapter, we apply our optimized variable grid FD method to directly model an open fluid-filled fracture described by the thin-layer model and compare these results with those obtained using the Coates-Schoenberg's approach (equivalent medium theory approach) for the linear-slip model. The purpose of this study is to determine to what extent the thin-layer model agrees with the linear-slip model.

Numerical results show excellent agreement between the two models for the wavefields away from the fracture. The discrepancy between the two is the presence of a slow wave propagating along the fracture of the thin-layer model. This study indicates that the thin-layer model is required to study the fracture slow wave, although the linear-slip model may be used to achieve accurate and more efficient modeling for the remote seismic characterization of fractures.

5.1 Introduction

The presence of fractures critically affects the permeability of rocks and therefore the character of fluid flow in hydrocarbon reservoirs. Thus, fracture detection and characterization is very important in hydrocarbon recovery. Seismic modeling of fractured media is an efficient tool for investigating the possibilities of using seismic waves to characterize the fractures.

For purposes of seismic wave propagation, fractures are often described as linear slip interfaces with displacement discontinuities (Schoenberg, 1980; Pyrak-Nolte, 1988). In the linear-slip model (LSM), it is assumed that a fracture can be represented by an interface across which the displacements caused by a seismic wave are discontinuous while the tractions remain continuous. The linear relationship between the jump in the displacement vector and the traction vector is determined by the fracture compliance tensor. Based on this model, Coates and Schoenberg (1995) introduced an equivalent medium theory approach for embedding a linear slip fracture within an anisotropic finite-difference (FD) code. In this approach, grid cells containing the fracture interface are replaced by grid cells with equivalent anisotropic properties that model the fracture and host compliance.

Alternatively, an open fluid-filled fracture can be represented by a thin fluid layer following the approach of Groenenboom and Fokkema (1998). For the thin-layer model (TLM), a fracture is directly modeled in the modeling scheme (Groenenboom and Falk, 2000). The optimized variable grid FD method developed in chapter 3 can be used to smoothly vary the cell spacing from the far-field mesh to the vicinity of the fracture, thus approximating the fracture directly by a number of grid points. This variable grid approach for explicit modeling of open fluid-filled fractures requires more cells than the Coates-Schoenberg approach. However, the use of the variable grid around the fracture significantly reduces the number of extra cells needed to model the fracture, compared to a constant, very fine grid.

We apply both the variable grid FD method and the Coates-Schoenberg approach to model a single open fluid-filled fracture described by the TLM and the LSM, respectively. The purpose of this study is to determine to what extent the TLM agrees with the LSM. Numerical results show that the agreement between the two models is excellent except for the existence of a slow fracture wave in the TLM. Two computations also demonstrate that the two models require almost the same computer memory, but the TLM costs more CPU time. The sections that follow present the methods and their comparison in greater detail.

5.2 Methodology

5.2.1 Variable grid FD method for the TLM

For constant grid FD methods, grid spacing, and hence the computational effort, is determined by the smallest length scale to be modeled, usually the shortest seismic wavelength. Explicitly modeling a fracture described by the TLM introduces a length scale (the fracture width), which is often two or three orders of magnitude smaller than the shortest seismic wavelength, thus greatly increasing the computational load and restricting calculations to models of very small overall dimensions. To overcome this problem, we apply the optimized variable grid FD scheme developed in chapter 3 to solve the 2-D velocity-stress elastic wave equation:

$$\begin{cases} \rho\dfrac{\partial v_x}{\partial t} = \dfrac{\partial \tau_{xx}}{\partial x} + \dfrac{\partial \tau_{xz}}{\partial z} \\ \rho\dfrac{\partial v_z}{\partial t} = \dfrac{\partial \tau_{xz}}{\partial x} + \dfrac{\partial \tau_{zz}}{\partial z} \\ \dfrac{\partial \tau_{xx}}{\partial t} = (\lambda + 2\mu)\dfrac{\partial v_x}{\partial x} + \lambda\dfrac{\partial v_z}{\partial z} \\ \dfrac{\partial \tau_{zz}}{\partial t} = (\lambda + 2\mu)\dfrac{\partial v_z}{\partial z} + \lambda\dfrac{\partial v_x}{\partial x} \\ \dfrac{\partial \tau_{xz}}{\partial t} = \mu(\dfrac{\partial v_x}{\partial z} + \dfrac{\partial v_z}{\partial x}) \end{cases} , \tag{5.1}$$

where v_x and v_z are the particle velocity components; τ_{xx}, τ_{xz}, and τ_{zz} are stress components; ρ is density; λ and μ are the Lamé coefficients.

We use a simple FD gridding scheme to represent the x-z fracture plane. The plane is partitioned into: (1) domains of fine grid spacing for resolving fractures, (2) domains of coarse grid spacing constrained by the shortest wavelength, and (3) transition regions where the grid spacing smoothly varies between these extremes (see Figure 5.1). The smooth refinement from the coarse grid spacing to fine grid spacing avoids the spurious reflection problems associated with sudden changes in

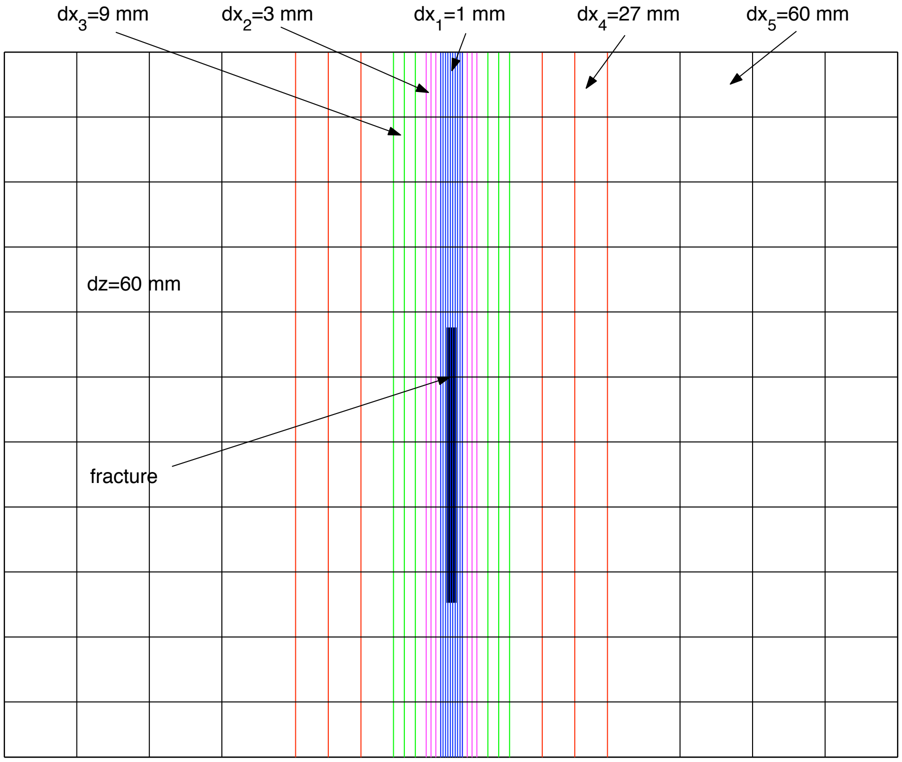

Figure 5.1: Grid spacing in the vicinity of the fracture. The horizontal grid spacing smoothly increases from 1 mm to 6 cm with a factor of 3 over a transition region of 11.7 cm wide. The vertical grid spacing is 6 cm throughout the grid.

grid spacing.

The spatial derivatives in equation (5.1) are approximated by the optimized fourth-order variable grid FD operator (see chapter 3). Coefficients for the stretched grid operators are pre-computed for all spatial locations. Since the mesh is only distorted along the x- and z-axes, coefficients are invariant along grid lines, reducing the memory required for stencil storage. The variable mesh is also staggered to increase stability and minimize numerical dispersion. The staggered scheme is crucial for handling solid-liquid contacts present in fractured media. Time derivatives are staggered across the velocity and stress variables and are approximated using an explicit second-order central difference operator.

To minimize numerical dispersion during the computation, the spatial discretization is chosen to satisfy the following inequality (Pitarka, 1999):

$$h_{max} < \frac{V_{min}}{5\, f_{max}}, \tag{5.2}$$

where h_{max} is the maximum grid spacing, V_{min} is the lowest velocity in the media, and f_{max} is the maximum frequency of the propagating signal.

The stability condition for the 2-D fourth-order staggered grid FD scheme with constant grid spacing h is (Levander, 1988):

$$\Delta t < \frac{1}{\sqrt{2}(|\alpha_1| + |\alpha_2|)} \frac{h}{V_{max}}$$

or

$$\Delta t < 0.606 \frac{h}{V_{max}}, \tag{5.3}$$

where $\alpha_1 = 9/8$ and $\alpha_2 = -1/24$ are the inner and outer coefficients of the fourth-order approximation to the first derivative. V_{max} is the highest velocity in the media.

Through a series numerical tests, we found that the optimized variable grid FD scheme used in this study is stable when the temporal increment Δt is chosen to satisfy equation (5.3) with the minimum grid spacing in the variable grid.

In the modeling, sponge absorbing boundary conditions (Cerjan et al., 1985) are used at the edges of the model to minimize artificial reflections at the boundaries of the computational domain.

5.2.2 Coates-Schoenberg approach for the LSM

To incorporate a fracture described by the LSM into a FD modeling scheme, Coates and Schoenberg (1995) introduced an equivalent anisotropic medium approach. In this approach, all FD grid cells containing a fracture are replaced by grid cells with equivalent anisotropic properties that model the fracture and host compliances (Figure 5.2). After this procedure, the standard FD modeling for anisotropic media can be applied.

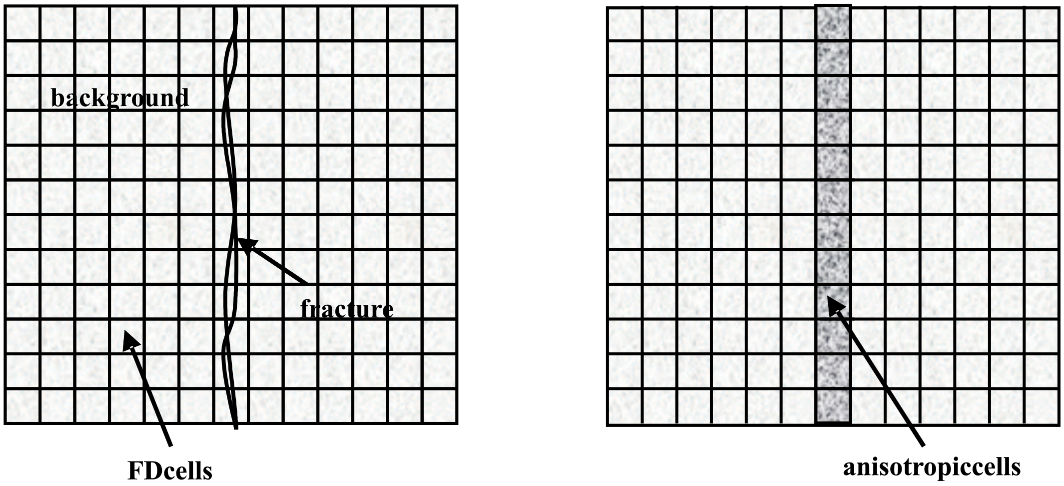

Figure 5.2: Representation of a vertical fracture in a FD model as a single column of anisotropic cells. The elastic constants for these cells are computed using the Coates-Schoenberg approach described in the text.

The process for obtaining the anisotropic elastic constants for the FD cells representing the fracture is based on a calculation of the average strain of each cell (Schoenberg and Sayers, 1995):

$$\epsilon_{ij}^{cell} = s_{ijkl}^{b}\sigma_{kl} + \frac{1}{2L}([u_i]n_j + [u_j]n_i), \tag{5.4}$$

where ϵ_{ijkl}^{b} is the compliance of the host rock, σ_{kl} is the stress, $[u_i]$ is the displacement jump across the fracture (i.e., the displacement-discontinuity or crack opening displacement), L is the length of the cell, and n_i is the fracture normal vector.

For the LSM, the displacement jump $[u_i]$ and the traction $\sigma_{jk}n_k$ are linearly related through the fracture compliance Z_{ij}:

$$[u_i] = Z_{ij}\sigma_{jk}n_k. \tag{5.5}$$

Then equation (5.4) becomes:

$$\begin{aligned}\epsilon_{ij}^{cell} &= s_{ijkl}^{b}\sigma_{kl} + \\ &\quad \frac{1}{4L}(Z_{ik}n_l n_j + Z_{jk}n_l n_i + Z_{il}n_k n_j + Z_{jl}n_k n_i)\sigma_{kl} \\ &\equiv s_{ijkl}^{cell}\sigma_{kl}.\end{aligned} \tag{5.6}$$

Here, s_{ijkl}^{cell} are the anisotropic compliances for the cell containing the fracture.

The compliance matrix given in equation (5.6) can be inverted to give the anisotropic elastic constants for the cell.

The variables required for the equivalent medium calculation in each FD cell are Lamé constants λ and μ of the background medium, the length of the fracture L (in two dimensions) in each cell, its orientation, and the normal and shear fracture compliances Z_N and Z_T.

For a vertical fracture with its normal in the x-direction, the four independent anisotropic elastic constants for a 2-D model in the x-z plane are (Nihei et al., 2001):

$$C_{ij}^{cell} = \begin{bmatrix} (\lambda+2\mu)(1-\delta_N) & \lambda(1-\delta_N) & 0 \\ \lambda(1-\delta_N) & (\lambda+2\mu)(1-r^2\delta_N) & 0 \\ 0 & 0 & \mu(1-\delta_T) \end{bmatrix}, \tag{5.7}$$

where

$r = \nu/(1-\nu)$,

$\delta_N = Z_N(\lambda+2\mu)/[L + Z_N(\lambda+2\mu)]$,

$\delta_T = Z_T\mu/(L + Z_T\mu)$,

and ν, λ and μ are the Poisson's ratio, Lamé constants of the background medium, Z_N and Z_T are the normal and shear fracture compliances, and L is the length of the fracture (in two dimensions) in the cell.

Equation (5.7) describes the fracture as a transversely isotropic material with a horizontal axis of symmetry (HTI media). A fracture oriented at an angle to the FD grid can also be modeled by applying a rotation transformation to Equation (5.7), as described by Coates and Schoenberg (1995); this leads into a full anisotropic medium with six independent elastic constants in two dimensions.

After the equivalent medium properties of each cell are obtained, the standard FD modeling for anisotropic media can be applied. The anisotropic FD code we used is based on a constant staggered grid FD scheme with fourth-order spatial differencing and second-order temporal differencing.

5.3 An open fluid-filled fracture model

Now, we apply both the variable grid FD method and the Coates-Schoenberg approach to model wave propagation in a medium with an open water-filled fracture described by the TLM and the LSM, respectively.

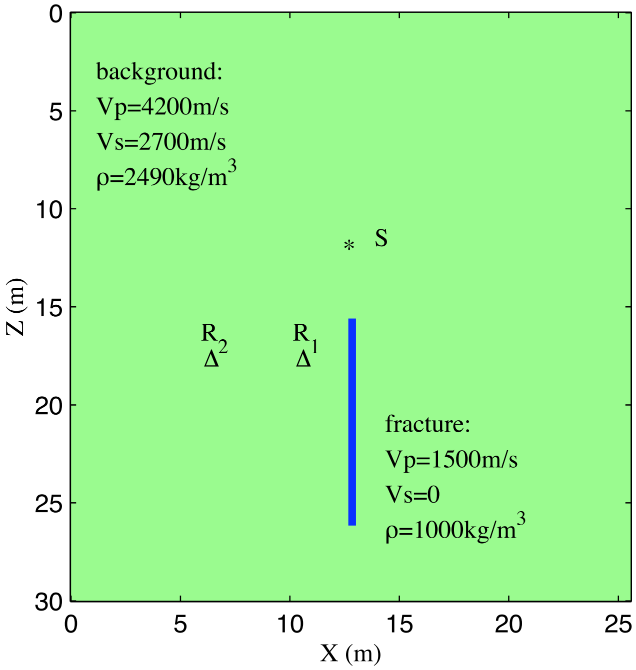

Figure 5.3: A vertical fracture model.

Figure 5.3 shows the model. A vertical water-filled fracture with 4 mm thickness and 10.56 m length is embedded in a homogeneous elastic medium. A monopole source (S), located at (12.78 m, 12 m), radiates a Ricker pulse with a central frequency of 3 kHz. Two receivers (R_1 and R_2) are located at (10.2 m, 18 m) and (6 m, 18 m). For variable grid FD modeling of the TLM, the horizontal grid spacing smoothly increases from 1 mm to 6 cm with a factor of 3 over a transition region 11.7 cm wide in the vicinity of the fracture; the vertical grid spacing is 6 cm throughout the grid (Figure 5.1). For the Coates-Schoenberg approach of the LSM, a constant FD grid spacing of 6 cm is used in both the x and z directions. The calculation of equivalent anisotropic elastic constants of the LSM cells containing the fracture is based on the transverse fracture compliance $Z_T = \infty$, and the normal fracture compliance $Z_N = h/K = 0.004$ m/2.25 GPa (h is the fracture width and K is the bulk modulus of the fluid). The parameters of the background medium are $\lambda = 7.6194$ GPa, $\mu = 18.152$ GPa, and $\nu = 0.148$ calculated from the P-wave velocity V_p, S-wave velocity V_s, and density ρ.

Snapshots of horizontal and vertical particle velocity components of the TLM and the LSM are shown in Figure 5.4. In order to make the faint fracture tip diffracted waves visible, the gain was chosen such that amplitudes were clipped at 1 % of the maximum value. It can be seen that the body wave (P) and the head wave (H) are in good agreement. The tip diffracted waves (PdP, PdS) are similar but with small differences in the amplitudes. The incomparable event is a guided wave (G) propagating along the fracture which is present in the snapshots of the TLM, but absent in the snapshots of the LSM. This guided wave, with a velocity around 1210 m/s, is the very slow wave predicted by Ferrazzini and Aki (1987). In theory, the TLM supports a family of symmetric and antisymmetric normal modes (Ferrazzini and Aki, 1987); the LSM supports only one symmetric and one antisymmetric modes (Pyrak-Nolte and Cook, 1987; Haugen and Schoenberg, 2000). Because the symmetry of the source-fracture geometry used in this study (Figure 5.3) generates only symmetric particle motion with respect to the fracture plane, only symmetric modes are considered in the fracture guided wave analysis presented in Appendix A. As Figure A-1 shows, except for the slow wave (the fundamental symmetric mode) of the TLM, none of the other symmetric modes is expected in our numerical results because the frequency of interest (3 kHz) is far below the cut-off frequencies of those modes (29.1 kHz for the first symmetric normal mode of the TLM and 20.4 kHz for the symmetric mode of the LSM).

Figure 5.5 shows the seismograms of the horizontal and vertical particle velocity

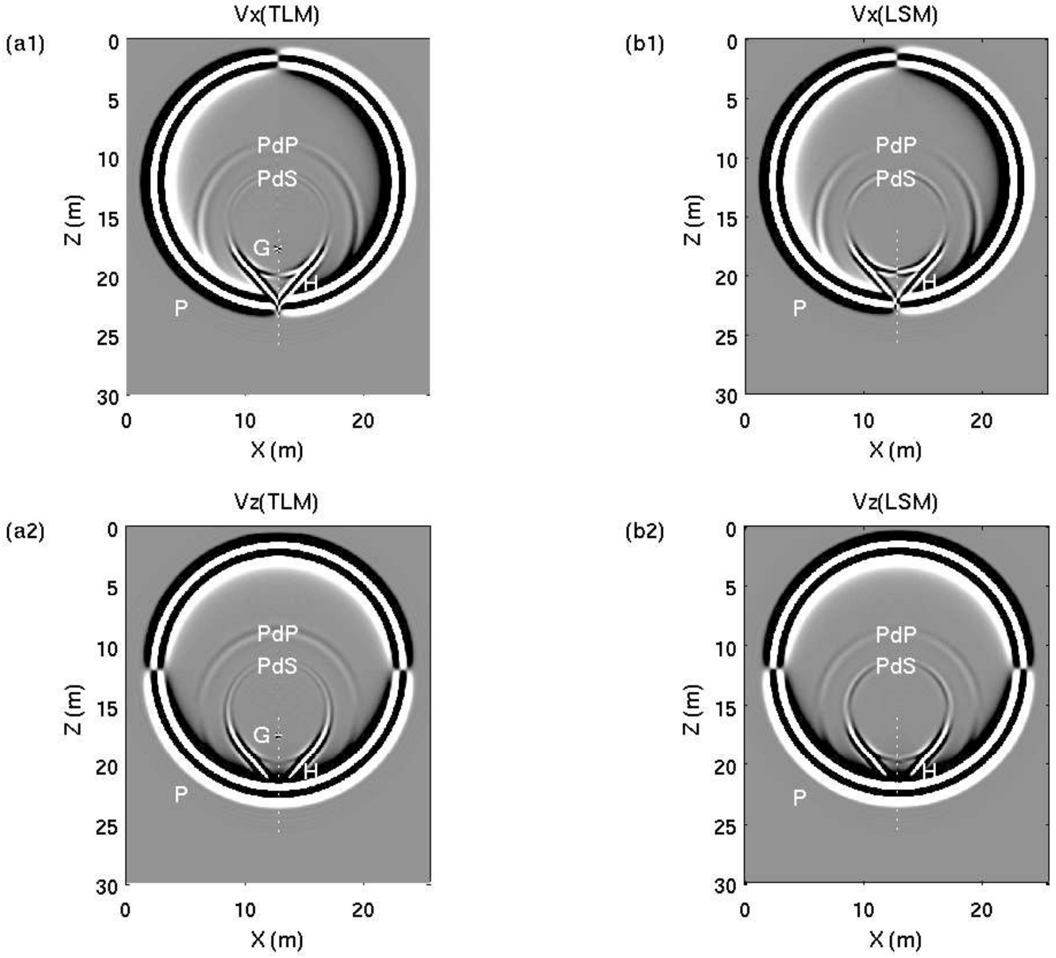

Figure 5.4: Snapshots of the horizontal and vertical particle velocity components (V_x and V_z) at 2.8 ms: (a1) and (a2) are the results of the thin-layer model (TLM); (b1) and (b2) are the results of the linear-slip model (LSM). P, H, and G are direct P-wave, head wave, and fracture guided wave; PdP and PdS are P-to-P and P-to-S diffracted waves, respectively. The fracture is indicated by the white dashed line.

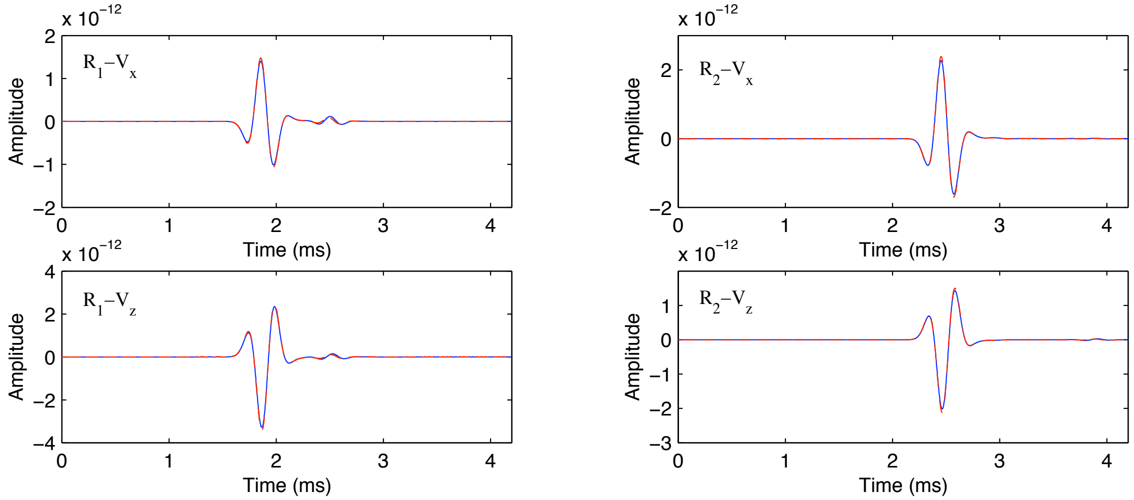

Figure 5.5: Comparison of seismograms of the horizontal and vertical particle velocity components (V_x and V_z) of the TLM (blue solid line) and the LSM (red dashed line) at receiver R_1 and R_2 in the model (Figure 5.3).

components recorded off the fracture at receivers R_1 and R_2 of the TLM (blue solid line) and the LSM (red dashed line). The fit between the two models is excellent. The corresponding normalized differences between the two models at these two receivers are shown in Figure 5.6. We can see that they are all less than 5 %. These results quantitatively demonstrate the excellent agreement of the two models for the body waves and fracture tip diffracted waves.

The simulations were performed on a 1.4 GHz Athlon computer with 1 GB DDR RAM. The memory requirements of the two models are comparable (8.7 MB for the TLM and 8.1 MB for the LSM). However, the CPU time used by the TLM (74 min) is much longer than that of the LSM (14 min). This is because a very small timestep required by the finest grid spacing in the variable grid (Figure 5.1) to satisfy the stability condition (5.3) is globally used for modeling the TLM. Implementation of a spatially variable timestep FD scheme can greatly reduce the CPU time used by the TLM. However, the modeling of the TLM is still more costly than that of the LSM for a set of fractures.

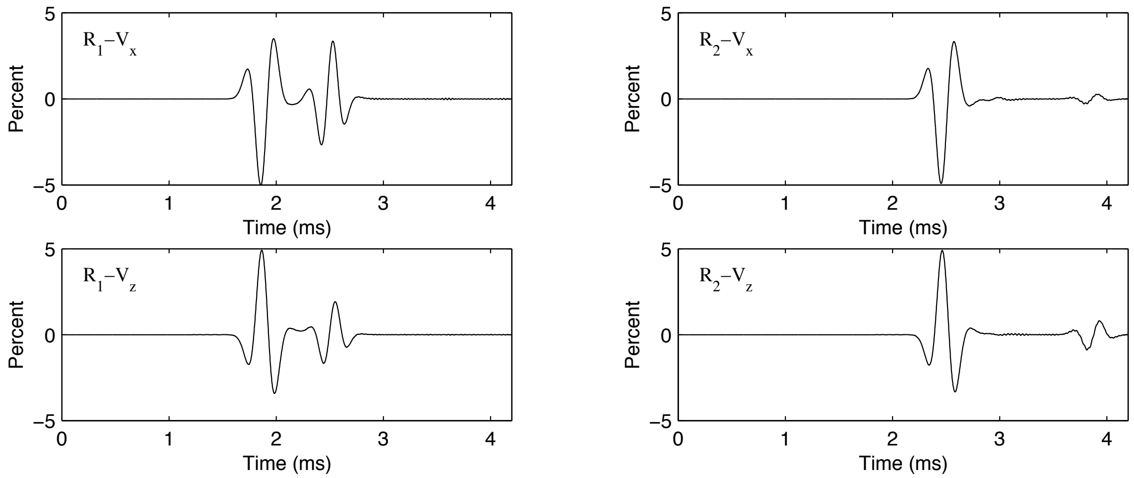

Figure 5.6: The normalized difference of the horizontal and vertical particle velocity components (V_x and V_z) between the TLM and the LSM at receiver R_1 and R_2 in the model (Figure 5.3).

5.4 Conclusions

We have performed seismic modeling for an open water-filled fracture described by the TLM and the LSM using the optimized variable grid FD method and the Coates-Schoenberg' approach, respectively. Numerical results show excellent agreement between the two models on body waves and fracture tip diffracted waves. The primary difference in the observed wavefields of the two models is the presence of a very slow fluid guided wave in the TLM, which is predicted by the theory and confirmed by the numerical simulations.

In this single fracture numerical experiment, the computer memory requirements of the two models are comparable. But the TLM uses more CPU time than the LSM. While the CPU time required by the TLM can be reduced by combining variable grid and variable timestep techniques, modeling the TLM is still more costly than that of the LSM for a model with a set of fractures.

This comparison study indicates that the TLM is required to study the fracture slow wave which can be observed in a borehole intersecting a fracture (Nagano and Niitsuma, 1996); for the remote seismic characterization of fractures, the LSM can be used to achieve accurate and more efficient modeling.

Chapter 6

Modeling single-well seismic

Single-well seismic imaging has recently emerged as a valuable tool for delineating well-parallel features within structurally complex regions. Forward modeling can provide crucial guidance in both the design of single-well experiments and in the later phases of processing and data interpretation. A significant difficulty in modeling single-well data is the large range of spatial scales present: efficient inclusion of a small borehole (10-20 cm) within a larger domain modeling (200-300 m) requires special computational techniques.

Our variable grid and timestep FD method efficiently solves this problem: using fine grid spacing and small timesteps in the vicinity of the borehole, and coarse grid spacing and large timesteps in the far-field, our method allows inclusion of a realistic well and captures the resulting propagation phenomenon including tube waves. Two single-well modeling examples, which include both boreholes of reasonable dimensions and reflecting salt structures in the far-field, demonstrate the efficacy of the numerical method. Although strong tube waves obscure some temporal regions of the data, reflections from the salt flank are evident.

6.1 Introduction

Single-well imaging techniques involve placing both a seismic source and a hydrophone string within the same well: geometries of this type allow characterization of reflectors near the borehole including high-angle faults, salt flanks (Cameron and Chen, 1995), and fracture regions (Majer et al., 1997). For structural features with near-vertical dips, single-well configurations provide favorable seismic illumination conditions in comparison to surface surveys. When horizontal boreholes exist within reservoirs, single-well measurements can aid interpreters in distinguishing local bed boundaries and fluid contacts.

Numerical forward modeling is an excellent tool for exploding the impacts of survey geometry and subsurface structure on imaging experiments. In the case of single-well seismic surveys, intelligent choice of acquisition parameters, such as source/receiver offset, are important in minimizing the amount of primary signal obscured by high-amplitude borehole modes. The realistic synthetic seismograms generated by forward modeling can also be used to evaluate data processing and inversion algorithms in situations where a known model is required.

A significant difficulty in single-well seismic modeling is a large scale difference between the diameter of the borehole and the formation extent present. To resolve the borehole, a structural feature with tiny lateral dimensions, a very fine mesh is required (2 cm). At the same time, the target of the single-well survey may be a salt flank as much as 60 m from the well with significant vertical extent. An equi-spaced mesh with sufficient resolution to describe the borehole and sufficient size to include far-field reflectors requires too much memory for simulation on most computers. The optimized variable grid FD technique developed in chapter 3 provides an efficient solution to this multi-scale borehole problem: smooth refinement in the vicinity of the borehole allows effective representation of the well without exhausting available memory resources. While FD stability condition requires a very small timestep for the finest grid spacing, the developed spatially variable timestep FD technique provides large timesteps for coarse grid spacing to further reduce the CPU time.

We apply our variable grid and timestep FD method for the single-well experiment study in the 2-D elastic case. Numerical results show: although strong tube waves dominate the wavefield, reflections from the salt flanks are visible. The use of variable grid spacing and timesteps significantly reduces computer memory requirements and CPU time in the modeling. The sections that follow present the study in detail.

6.2 Methods

We apply the variable grid and timestep FD method to solve the 2-D displacement-stress wave equation for single-well seismic modeling. The 2-D wave equation can be written as:

$$\begin{cases} \rho\dfrac{\partial^2 u_x}{\partial t^2} = \dfrac{\partial \tau_{xx}}{\partial x} + \dfrac{\partial \tau_{xz}}{\partial z} \\ \rho\dfrac{\partial^2 u_z}{\partial t^2} = \dfrac{\partial \tau_{xz}}{\partial x} + \dfrac{\partial \tau_{zz}}{\partial z} \\ \tau_{xx} = (\lambda + 2\mu)\dfrac{\partial u_x}{\partial x} + \lambda\dfrac{\partial u_z}{\partial z} \\ \tau_{zz} = (\lambda + 2\mu)\dfrac{\partial u_z}{\partial z} + \lambda\dfrac{\partial u_x}{\partial x} \\ \tau_{xz} = \mu(\dfrac{\partial v_x}{\partial z} + \dfrac{\partial v_z}{\partial x}) \end{cases}, \qquad (6.1)$$

where u_x and u_z are the displacement components; τ_{xx}, τ_{xz}, and τ_{zz} are stress components; ρ is density; λ and μ are the Lamé coefficients.

FD solution of equation (6.1) is based on a spatial staggered grid scheme which is crucial for handling the solid-liquid contact present within the borehole.

For spatial discretization, a simple variable grid is used to represent the x-z borehole plane. The plane is partitioned into a near-field region, with fine grid spacing to resolve borehole phenomena, a far-field, with a coarse grid spacing constrained by numerical dispersion, and a transition region where the grid spacing smoothly varies between these extremes (see Figure 6.2). This smooth grid refinement avoids the artificial reflections associated with a sudden change in grid spacing.

For temporal discretization, a small timestep is used for the fine grid spacing region and the transition zones, and a large timestep is used for the coarse grid spacing zones (see Figure 6.2). The small and large timesteps are determined based on local stability criteria.

The spatial derivatives in equation (6.1) are approximated by the optimized fourth-order variable grid FD operator described in chapter 3. We pre-compute the coefficients for the stretched grid operators for all spatial locations. Since the mesh is only distorted along the x- and z- axes, coefficients are invariant along grid lines, reducing the memory required for stencil storage.

Time derivatives are approximated using an explicit second-order central difference operator. However, different timesteps are used for the time stepping in different domains (check chapter 3 for details). Although the implementation of the variable timestep FD scheme in two dimensions is more complex than in one dimension, the time stepping procedure for both one and two dimensions is the same.

6.3 Examples

Now we use the 2-D variable grid and time-step FD code for single-well experiment study. Numerical modeling of two models is performed. The first model, composed only of a vertical well and a simple sediment-salt interface, is used to explore the wide range of wave phenomenon captured by our elastic modeling code. The second test model incorporates a realistic geological structure more typical of the salt-flank plays where single-well imaging is currently being applied. The results from both seismic simulations show reflections from the primary targets which are partially obscured by strong borehole modes over limited temporal windows.

In the first model (Figure 6.1) the borehole is uncased, 14 cm in diameter, and water filled. The source function used to excite the model is a Ricker wavelet with a central frequency of 500 Hz. Figure 6.2 shows the variable grid spacing and timesteps used in the vicinity of the borehole. The lateral grid spacing smoothly increases from 0.01 m to 0.27 m with a factor of 3 over a transition region 0.36 m wide. The vertical spacing is 0.27 m throughout the grid. A small timestep of 2.6×10^{-3} ms is used for the zone with fine grid spacing (inside the two red lines) and a large timestep of 7.8×10^{-3} ms is used for the zones with coarse grid spacing (outside the two red lines). The large timestep is three times greater than the small timestep.

The property contrast between the salt (V_p = 4550 m/s, V_s = 2630 m/s, ρ = 2160 kg/m^3) and the surrounding sediments (V_p =2500 m/s, V_s = 1527 m/s, ρ = 2050 kg/m^3) produces high amplitude reflections. A snapshot of the τ_{xx} component of the wavefield recorded at 21 ms, Figure 6.3, shows a multitude of active modes. In addition to direct P- and S-waves (P, S) and a strong tube wave (T), salt flank reflections (PPr: P-to-P reflection, PSr: P-to-S converted reflection, SPr: S-to-P

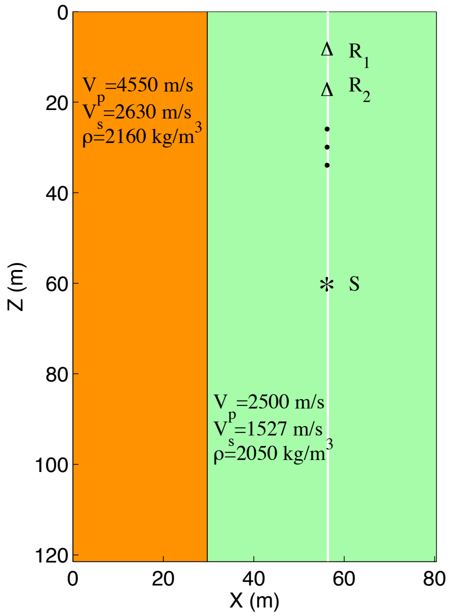

Figure 6.1: Vertical salt flank model.

converted reflection) and transmitted waves (PPt: P-to-P transmission, PSt: P-to-S converted transmission, SSt: S-to-S transmission) are visible.

Figure 6.4 shows the seismogram of the pressure component. We can see: although the strong tube wave dominates the wavefield, reflections from the salt flank are evident.

Our second model (Figure 6.5) incorporates a more complex geological structure, including several dipping sediment layers and a pair of salt-bounded petroleum traps. The borehole parameters used are identical to those described in the first example but the central frequency of the source wavelet is 250 Hz. Table 6.1 provides the physical properties of the model layers. Note that model components 7 and 8 are oil-saturated sections of layers 5 and 3 respectively, while component 9 is a gas pocket in layer 2.

Figure 6.6 shows four τ_{xx} component snapshots which clearly illustrate the wavefield propagation and interaction in the complex media. With the aid of the snapshots, events in the pressure seismogram (Figure 6.7) can be identified: direct P- and S-waves (P and S), strong tube wave (T), salt-dome reflection ($\mathrm{PP_s}$), layer reflections ($\mathrm{PP_l}$, $\mathrm{TT_l}$), and converted layer reflections from salt-dome reflections ($\mathrm{PP_sS_l}$).

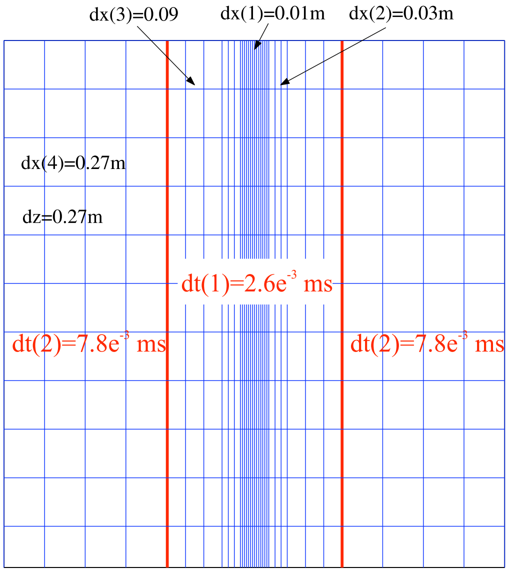

Figure 6.2: Grid spacing and timesteps in the vicinity of the borehole. The horizontal grid spacing smoothly increases from 0.01 m to 0.27 m with a factor of 3 over 0.36 m wide transition region. The vertical grid spacing is 0.27 m throughout the grid. A small timestep of 2.6×10^{-3} ms is used for the fine grid spacing zone (inside the two red lines) and a large timestep of 7.8×10^{-3} ms is used for the coarse grid spacing zones (outside the two red lines).

This example reveals both the high level of wavefield complexity introduced by a small number of lithological boundaries and the effectiveness of our variable grid and timestep FD code in handling multiple-scale models.

For the two simulations, the use of the variable grid spacing saves 93% memory and 98% CPU time for the first model, and saves 95% memory and 99% CPU time for the second model; the use of the variable timestep scheme for the variable grid further reduces the CPU time of 56% for the first model and of 48% for the second model with almost the same memory requirements.

6.4 Conclusions

We have applied the variable grid and timestep FD method for single-well seismic modeling. The use of a variable grid mesh enables us to include a properly scaled

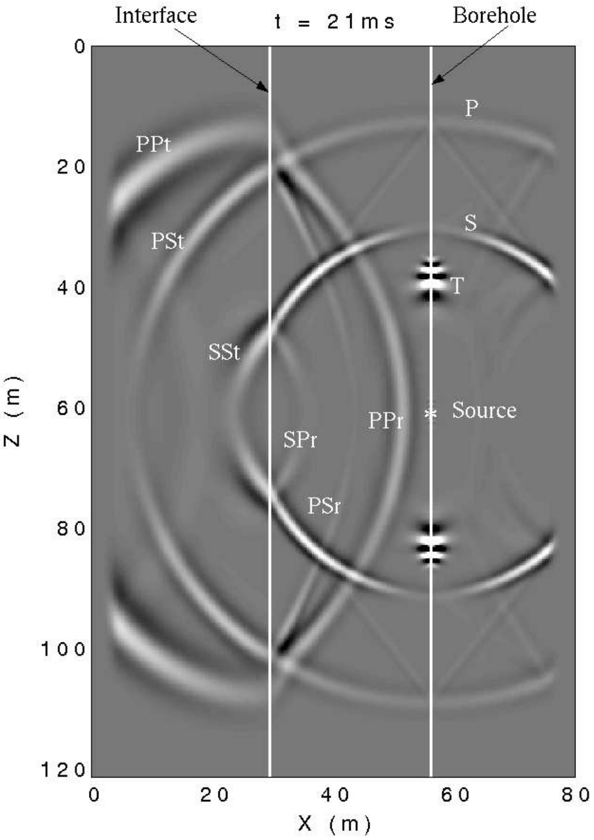

Figure 6.3: Snapshots of τ_{xx} component of the vertical salt flank model (Figure 6.1) at 21 ms. P, S, and T are direct P-wave, S-wave and tube wave; PPr is the P reflections; PSr and SPr are P-to-S, S-to-P converted reflections; PPt and SSt are the P and S transmissions, respectively; PSt is P-to-S converted transmission.

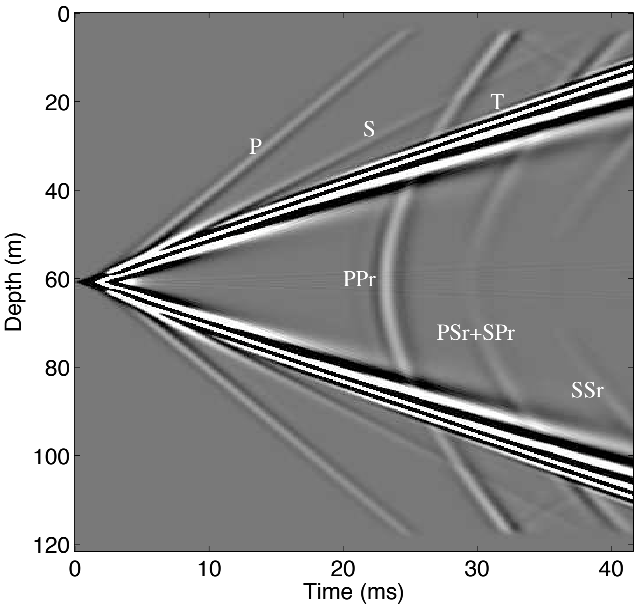

Figure 6.4: Seismogram of pressure of the vertical salt flank model (Figure 6.1). P, S, and T are direct P-wave, S-wave and tube wave; PPr and SSr are the P and S reflections, respectively; PSr and SPr are P-to-S, S-to-P converted reflections, respectively.

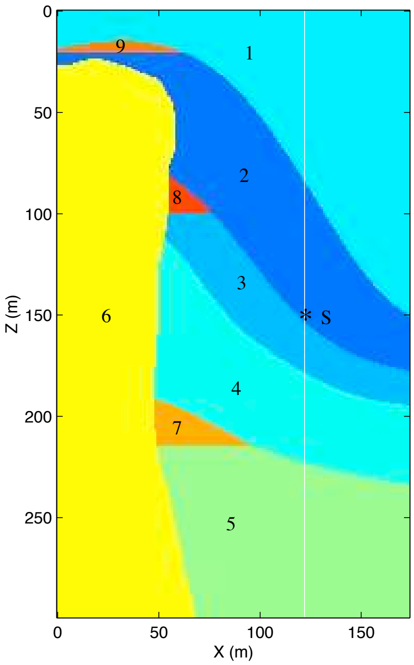

Figure 6.5: Realistic salt flank model. The material properties are presented in Table 6.1.

No.	V_p (m/s)	V_s (m/s)	ρ (kg/m^3)
1	2900	1700	2050
2	3200	1880	2100
3	3700	2180	2130
4	3300	1940	2000
5	4500	2650	2200
6	4900	2630	2160
7	4300	2650	2100
8	3400	2190	2050
9	2200	1890	2000

Table 6.1: Material properties for the second model (Figure 6.5).

borehole within a larger computational domain; and the use of a spatially variable timestep scheme that matches with the spatially variable grid further reduces the CPU time. Excellent synthetic gathers of two single-well models demonstrate the efficacy of the variable grid and timestep FD method. Although strong tube waves obscure some temporal regions of the data, reflections from the salt flank are evident.

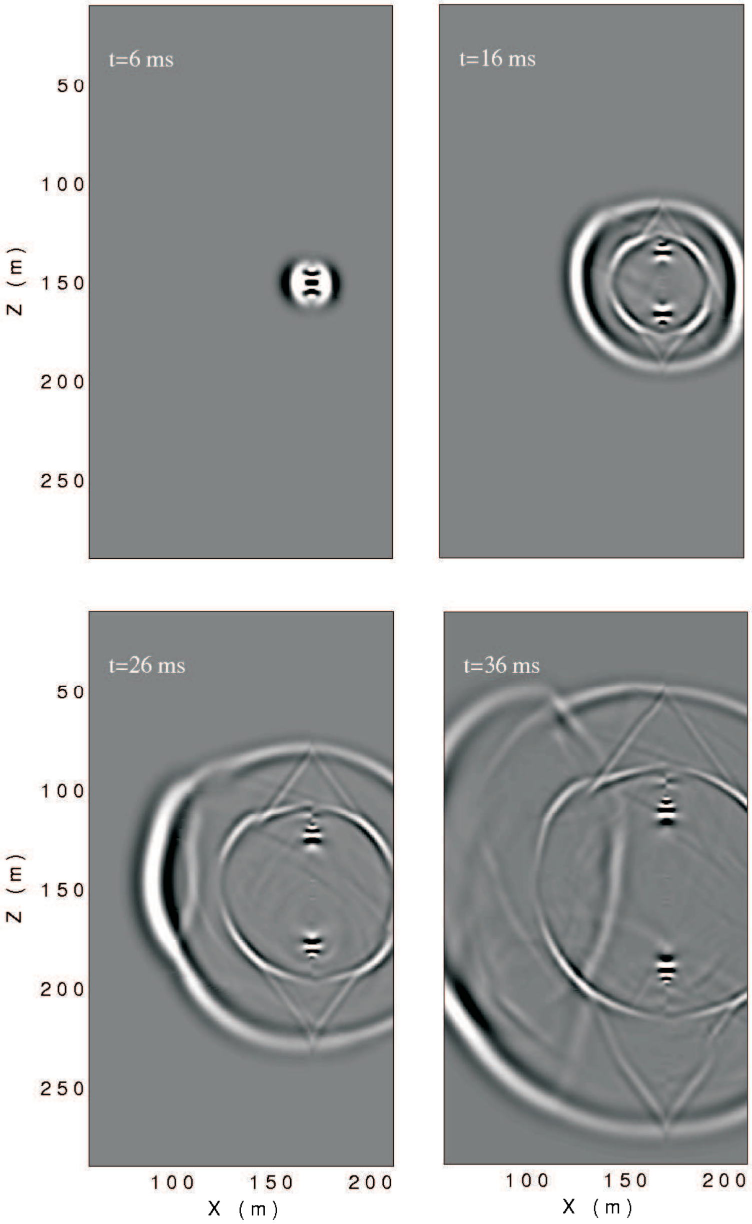

Figure 6.6: Snapshots of τ_{xx} components of the realistic salt flank model (Figure 6.5) at 6, 16, 26 and 36 ms.

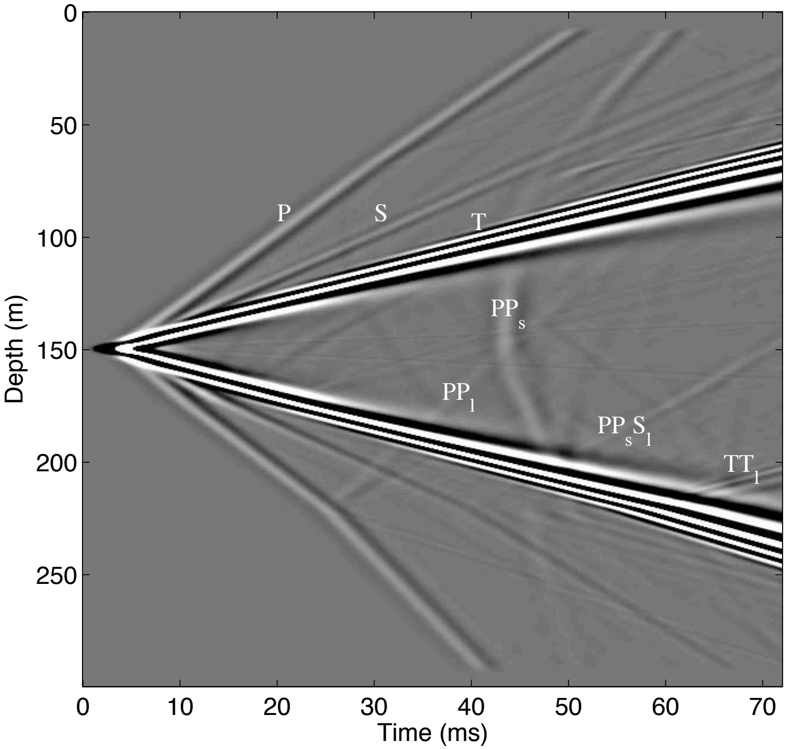

Figure 6.7: Pressure seismogram of the realistic salt flank model (Figure 6.5). P, S and T are direct P-wave, S-wave and tube wave; $\mathrm{PP_s}$ is the salt flank P-to-P reflection; $\mathrm{PP_l}$ and $\mathrm{TT_l}$ are the P-to-P and T-to-T layer reflections; and $\mathrm{PP_sS_l}$ is the converted layer reflection from the P-to-P salt flank reflection.

Chapter 7

Modeling cross-well field data

—including tube waves and tube-wave-related arrivals

Cross-well seismic data often contain strong tube waves and tube-wave-related arrivals due to the effects of the presence of two boreholes. A basic requirement for accurate cross-well seismic modeling is the inclusion of these events associated with fluid-filled boreholes.

In this chapter, we apply a parallel variable grid FD 2-D code for cross-well field data modeling with inclusion of two perforated cased boreholes. The synthetics resemble the field observations in terms of arrival times not only on direct P- and S-waves but also on tube waves and tube-wave-related secondary arrivals generated by perforations in the receiver and source wells. This study demonstrates that including boreholes into the modeling scheme can distinguish tube-wave-related events on seismograms to better assist data analysis and to guide data processing and interpretation.

7.1 Introduction

Cross-well seismic technology involves placing a seismic source in one well and a hydrophone string in another well. This technique has been widely used for reservoir characterization and waste site detection because it can provide high resolution images about subsurface. However, the presence of two boreholes has significant effects on cross-well seismic field data. Many of the strongest signals observed are modes traveling within the borehole: these tube waves are often sufficient to cloak the lower amplitude reflections and transmissions. Moreover, tube waves can re-radiate energy into the formation at changes along the borehole to generate tube-wave-related arrivals (Balch and Lee, 1984, White and Lessenger, 1988). To better understand wave patterns observed in the field data and to guide data processing and interpretation, accurate cross-well seismic modeling with inclusion of these events is required.

Full-waveform forward modeling is desirable for cross-well seismic experiments since not only P-waves but also S-waves are observed in the data. We apply our optimized variable grid FD method for solution of the 2-D velocity-stress elastic wave equation for cross-well seismic modeling. The variable grid FD algorithm can accommodate the two small boreholes in a large modeling scheme by using the grid refinement around each borehole. Furthermore, a parallel version of the algorithm is developed for more efficient calculations on a "Linux Beowulf" cluster.

The parallel variable grid FD code is used for modeling study of the cross-well field data acquired from West Texas. First, a simple model is used to test the field data analysis. Then the field data modeling is performed based on the survey geometry. Comparison between the synthetic and the field data shows that a good agreement has been achieved not only on direct P- and S-arrivals, but also on tube waves and tube-wave-related events.

7.2 Methods

The 2-D velocity-stress elastic wave equation suitable for a staggered grid FD scheme in both space and time (Virieux, 1984, 1986; Levander, 1988; Graves, 1996) is:

$$\begin{cases} \rho\dfrac{\partial v_x}{\partial t} = \dfrac{\partial \tau_{xx}}{\partial x} + \dfrac{\partial \tau_{xz}}{\partial z} \\ \rho\dfrac{\partial v_z}{\partial t} = \dfrac{\partial \tau_{xz}}{\partial x} + \dfrac{\partial \tau_{zz}}{\partial z} \\ \dfrac{\partial \tau_{xx}}{\partial t} = (\lambda+2\mu)\dfrac{\partial v_x}{\partial x} + \lambda\dfrac{\partial v_z}{\partial z} \\ \dfrac{\partial \tau_{zz}}{\partial t} = (\lambda+2\mu)\dfrac{\partial v_z}{\partial z} + \lambda\dfrac{\partial v_x}{\partial x} \\ \dfrac{\partial \tau_{xz}}{\partial t} = \mu(\dfrac{\partial v_x}{\partial z} + \dfrac{\partial v_z}{\partial x}) \end{cases} , \tag{7.1}$$

We solve this equation on a variable grid mesh and apply the fourth-order optimized variable grid FD operator developed in chapter 3 to approximate the spatial derivatives. The temporal derivatives are approximated by a second-order central difference operator.

Spatially discretizing a cross-well model involves applications of the grid refinement technique used in single-well modeling (see chapter 6) in the vicinity of two boreholes. The variable grid mesh is characterized with: (1) domains of fine grid spacing for resolving boreholes with casing and cement, (2) domains of coarse grid spacing constrained by the shortest wavelength in the medium, and (3) transition regions where the grid spacing smoothly varies between these extremes (see Figure 7.1). The use of the variable grid mesh greatly reduces the computer memory requirements and CPU time thereafter compared to a constant fine grid mesh.

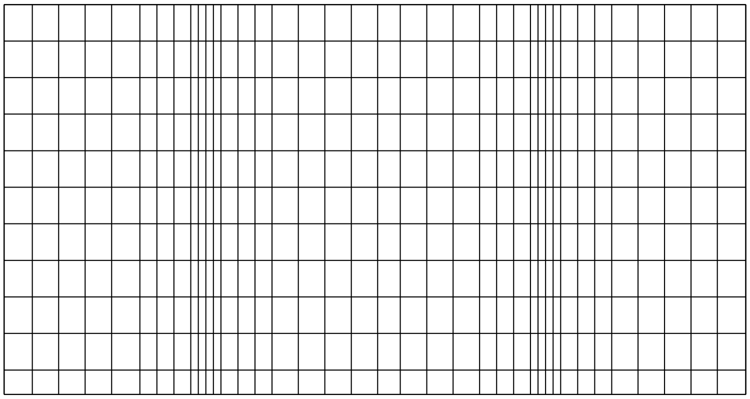

Figure 7.1: Variable grid mesh for a cross-well model. The horizontal grid spacing is variable to accommodate small scale boreholes with casing and cement in a large model.

Furthermore, a parallel version of the algorithm has been developed for more efficient calculations on a "Linux Beowulf" cluster. The parallel implementation utilizes spatial domain decomposition: different portions of the 2-D grid are allocated to different processors so that calculations within each subdomain take place synchronously. Sufficient overlap between adjacent subdomains/processors must be provided so that the fourth-order spatial FD operators can address all dependent variables at their particular staggered grid storage locations. Interprocessor data communication is based on the MPI (Message Passing Interface).

7.3 Field data analysis and modeling

The cross-well field data we are analyzing and modeling were collected in the Permian Basin, West Texas. Figure 7.2 shows the survey geometry. Two cased boreholes with 640 ft separation were used. The source well and receiver well have perforations at the depth of 9000 ft and 8930 ft, respectively.

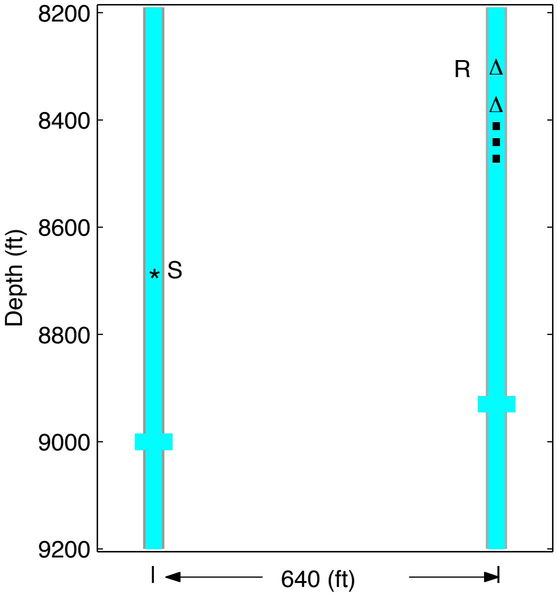

Figure 7.2: Cross-well field survey geometry. The survey depth coverage is from 8190 to 9200 ft. The distance between the two cased boreholes is 640 ft. The source and receiver wells have perforations at the depth of 9000 ft and 8930 ft, respectively.

7.3.1 Field data analysis

Figure 7.3 shows a common-shot gather from this survey. The source is at depth 8695 ft with receiver sampling interval of 5 ft. The depth of the receivers ranges from 8190 to 9200 ft. In this data, in addition to direct P- and S-waves (P, S), strong tube waves (PT, ST, TPT, TST) and tube-wave-related secondary P and S arrivals (TP, TS) are observed. The tube waves and the secondary body waves observed in the common-shot gather are caused by the borehole perforations (Mo and Harris, 1995). Perforations act as impedance discontinuities in a borehole. Impedance discontinuities in the source well cause tube waves to radiate body waves; impedance discontinuities in the receiver well cause tube waves to be generated by body wave interactions (Balch and Lee, 1984).

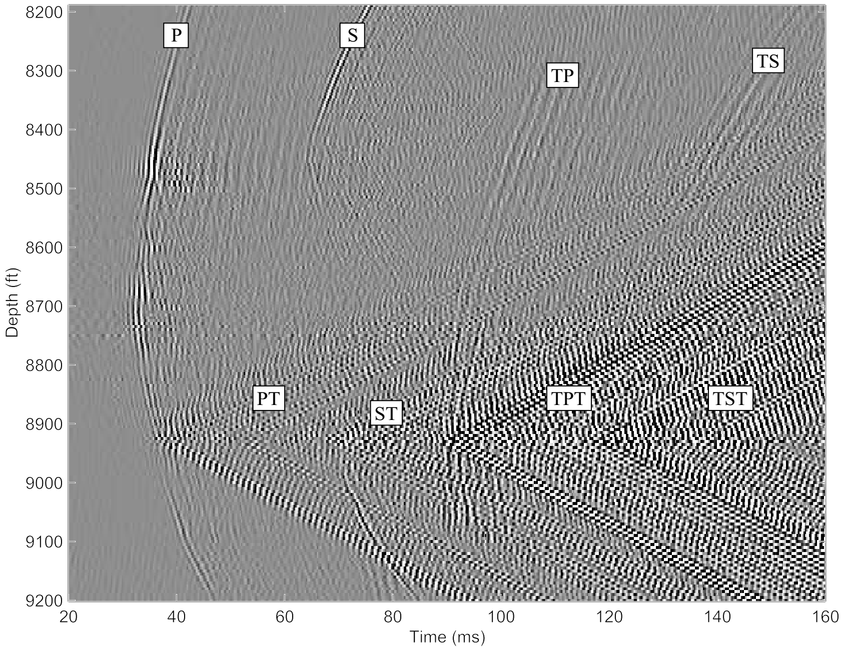

Figure 7.3: A common-shot gather of the cross-well survey from West Texas. The source depth is 8695 feet.

Figure 7.4 schematically illustrates the ray paths (Figure 7.4a) and the associated arrivals in the seismogram (Figure 7.4b) of a common-shot gather. In the source well, the source excites body waves (P, S), and also excites tube waves (T) propagating along the source well. When the tube waves hit the perforations in the source well, they radiate energy into the formation to generated tube-wave-related body waves (TP, TS). When the body waves (P, S, TP, TS) impinge upon the receiver well, strong tube waves (PT, ST, TPT, TST) are excited at the perforations and propagate along the receiver well to be recorded.

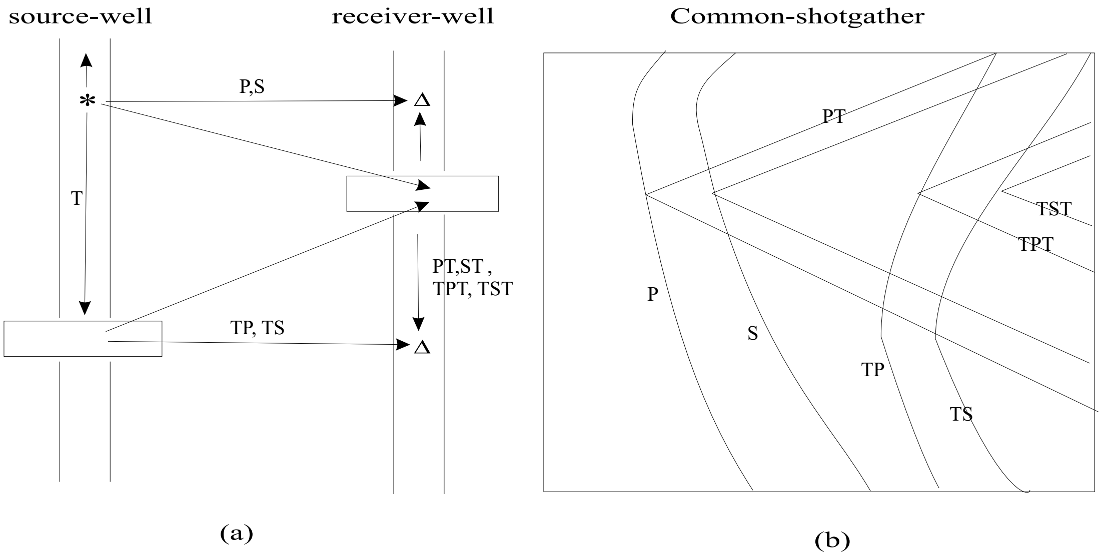

(a) (b)

Figure 7.4: Schematic diagram of waves in the cross-well survey: (a) Ray paths; (b) Arrivals in the seismogram. P and S are the direct P- and S-waves, TP and TS are the secondary P and S-waves radiated by the source tube waves (T) at the perforations in the source well. PT, ST and TPT, TST are receiver tube waves generated by the direct and secondary body waves at the perforations in the receiver well.

To test this data analysis requires including boreholes, casings and perforations into the modeling scheme.

To clearly illustrate this, the following modeling study is performed using the 2-D variable grid FD code.

First, we conduct the cross-well seismic modeling for a homogeneous model without boreholes (Figure 7.5a). In the synthetic seismogram (Figure 7.5b), we only observe the direct P-wave excited by a pressure source.

Then, we perform the modeling for the homogeneous model with two cased boreholes (Figure 7.6a). We can see both the direct P- and S-waves are observed in the

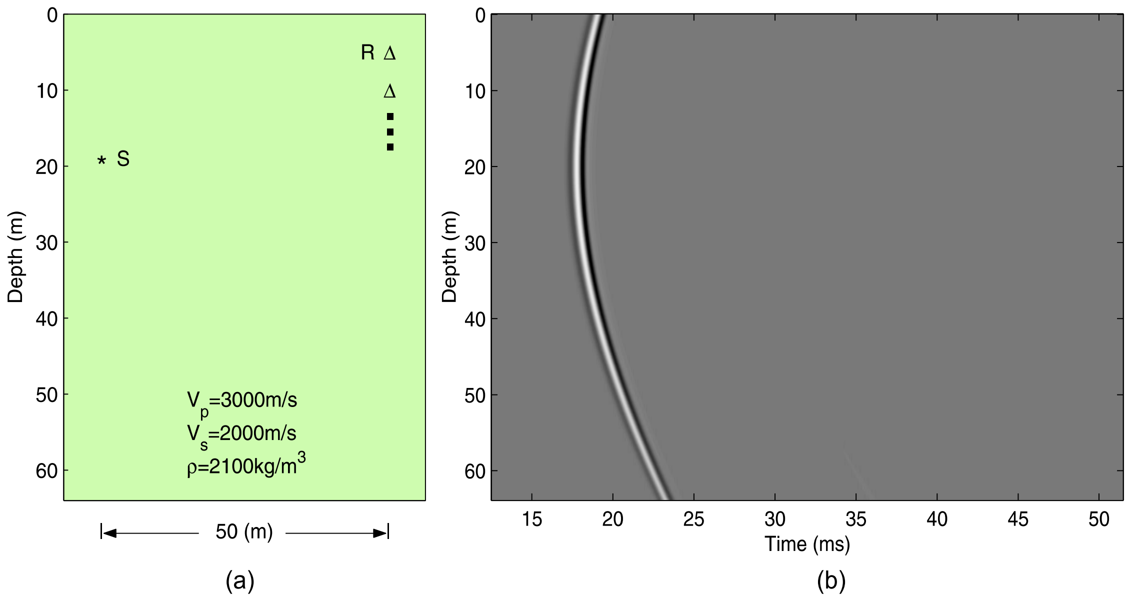

Figure 7.5: (a) Model: a homogeneous medium without boreholes; (b) Synthetic seismogram of the left model: only direct P-wave is observed.

seismogram (Figure 7.6b). The direct S-wave is P-to-S converted transmission at the contact between the source borehole and the formation.

Third, we add perforations in the source well (Figure 7.7a) and perform the simulation for this model. In addition to the direct P- and S-waves, tube-wave-related P- and S-waves are observed in the seismogram (Figure 7.7b). The secondary body waves are generated by the tube wave radiation at the perforations in the source well.

Finally, we add perforations in the receiver well too (Figure 7.8a), the simulation result of this model (Figure 7.8b) shows that tube waves are generated at the perforations in the receiver well.

This simple modeling study demonstrates the significant effects of boreholes, casings, and perforations on cross-well seismic data. Accurate field data modeling requires the inclusion of all these small features into the modeling scheme.

7.3.2 Field data modeling

Now, we use the 2-D variable grid FD parallel code to model the common shot

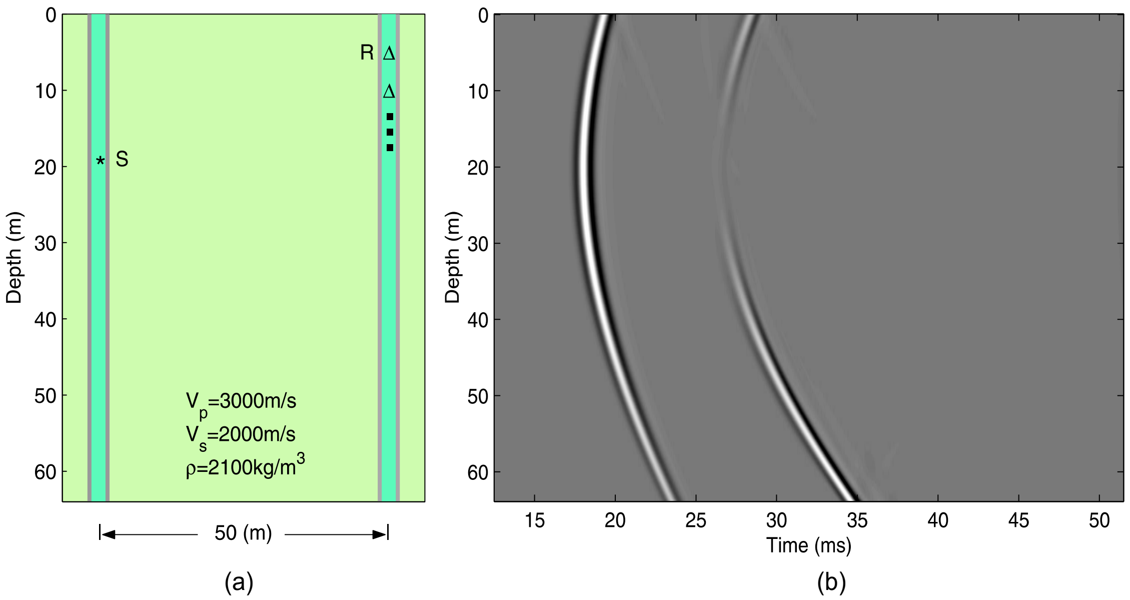

Figure 7.6: (a) Model: a homogeneous medium with two cased boreholes; (b) Synthetic seismogram of the left model: both direct P- and S-waves are observed.

gather showed in Figure 7.3 with inclusion of the two perforated cased boreholes. The model is based on the survey geometry (Figure 7.2). P-wave velocities of the formation are obtained from the blocked P-wave velocity log in the source well (Figure 7.9a). The corresponding S-wave velocities are calculated by $V_s = V_p/\sqrt{3}$. The densities are obtained by $\rho = 0.23{V_p}^{0.25}$ (Gardner et al., 1974). Note in this latter equation, the unit of ρ is g/cm^3 and the unit of V_p is ft/s. Two perforated cased boreholes are embedded in the layered formation. The parameters for the two boreholes are the same: the diameter is 7.2 inch, water-filled, the thicknesses of the casing and cement are 0.6 inch and 1.2 inch, respectively. Perforations are represented by a small rectangular hole cut through the casing, cement and into the formation. Figure 7.1 schematically illustrates the computational mesh used for the model. In the vicinity of the wells, the lateral grid spacing smoothly increases from 0.05 ft to 1 ft over a transition region of 1.8 ft wide. The vertical spacing is 1 ft throughout the grid. The total grid size for this variable grid mesh is $NX \times NZ = 742 \times 1151$, which is less than 5% of the total grid size of a regular mesh with constant dx=0.05 ft in the entire model ($NX \times NZ = 14980 \times 1151$); therefore, the computer memory requirements

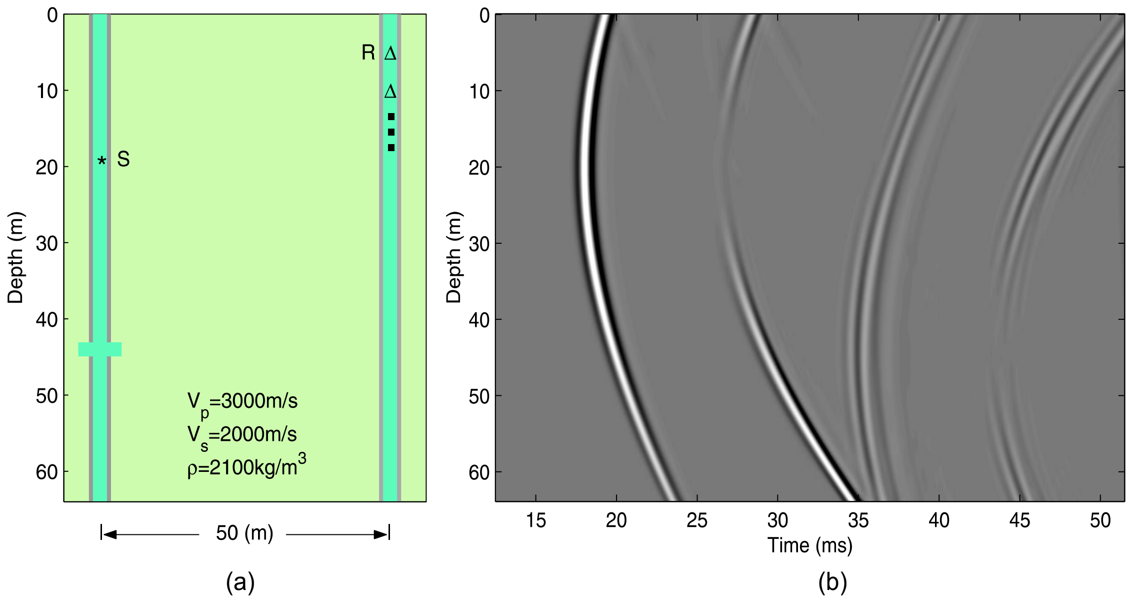

Figure 7.7: (a) Model: the source-well has perforations at 44 m; (b) Synthetic seismogram of the left model: in addition to direct P- and S-waves, tube-wave-related P- and S-waves are observed.

and CPU time thereafter are greatly reduced by the variable grid approach. Spectral analysis reveals that the frequencies in the field data are from 400 Hz to 1200 Hz. We use a Ricker wavelet with 800 Hz central frequency as the source function to excite the model. The calculations were performed on a 16 processor distributed “Linux Beowulf” cluster. One run of 110,000 timesteps for the 742×1151 size model takes about 3 hours CPU time. If the simulation is performed using a serial code on a single processor, it takes almost two days.

The synthetic seismogram of the common shot gather is shown in Figure 7.9b. We see that all the identified arrivals in the field data (Figure 7.3): direct waves (P, S), tube-wave-related arrivals (TP, TS) and strong tube waves (PT, ST, TPT, TST) are observed in the synthetic seismogram. There is a good match between the synthetic and the field observations for these events, especially in terms of the travel times. The difference between the synthetic and the field observations on the relative amplitude of some events (PT, ST, and interface reflections) may be due to the intrinsic attenuation in the real earth. This modeling result supports the previous

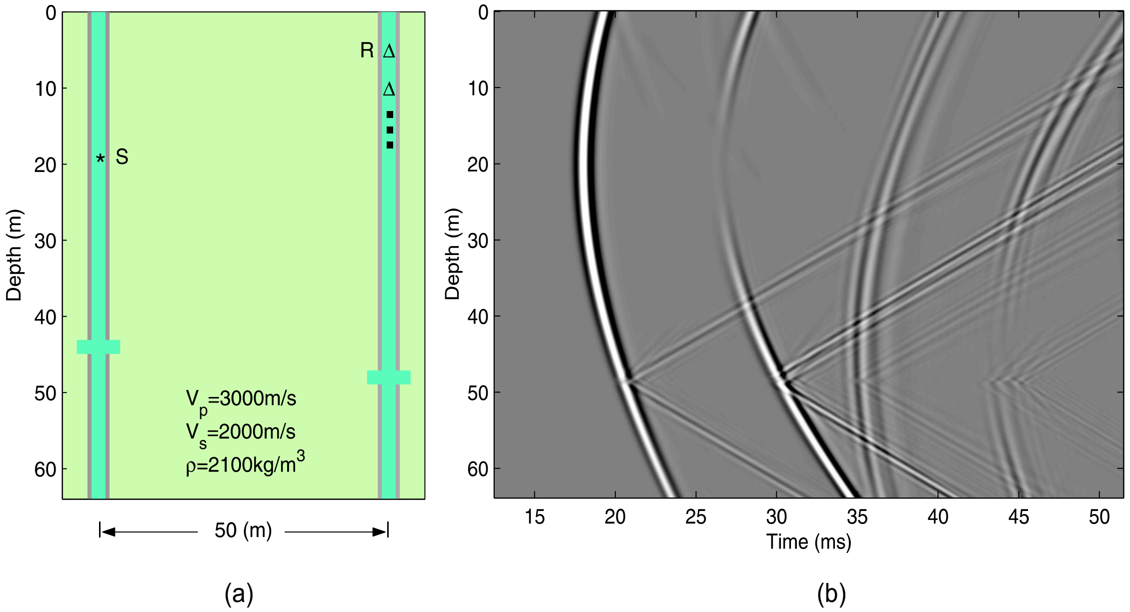

Figure 7.8: (a) Model: the source-well and the receiver-well have perforations at 44 m and 48 m, respectively; (b) Synthetic seismogram of the left model: in addition to the direct and secondary body waves, tube waves are observed.

data analysis and can be used to guide the later phase of data processing such as tube wave attenuation.

7.4 Conclusions

A 2-D velocity-stress optimized variable grid FD parallel code has been used for efficiently modeling the cross-well seismic field data from West Texas with the inclusion of the two perforated cased boreholes in the modeling scheme. The synthetic data not only match the direct P- and S-arrivals in the field observations, but also fit the tube waves and tube-wave-related events generated by the perforations in the source and receiver wells. This study demonstrates that inclusion of boreholes into the modeling scheme can capture tube-wave-related phenomena on seismograms to better assist data analysis and to guide data processing and interpretation.

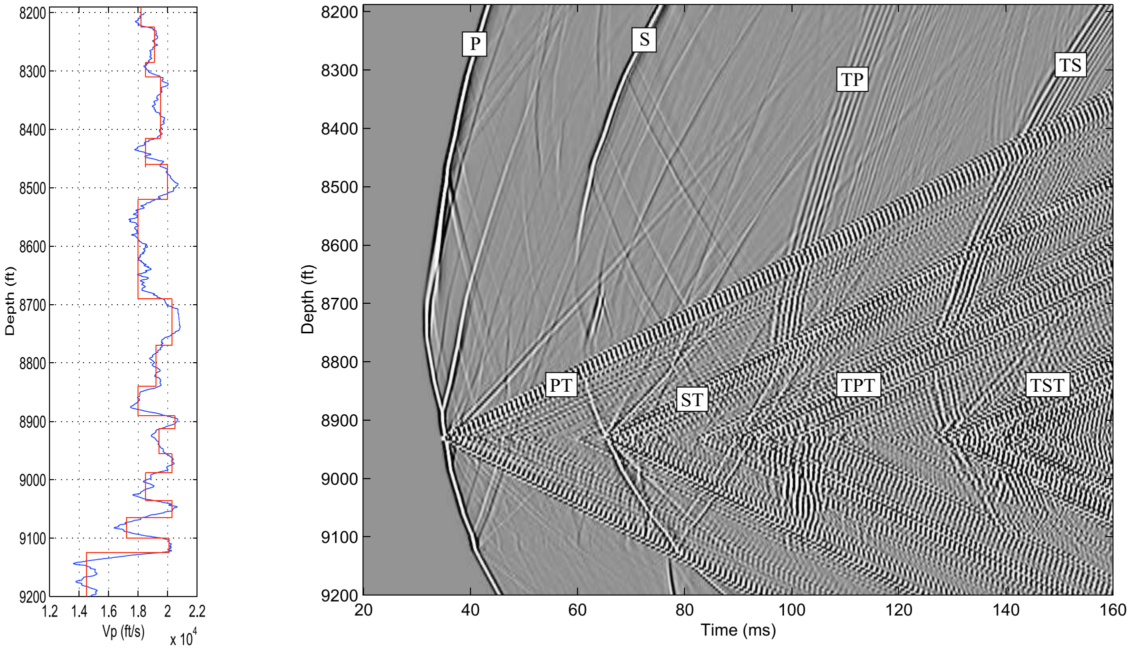

(a) (b)

Figure 7.9: (a) Blocked V_p log from the source well; (b) Synthetic seismogram generated by 2-D variable grid FD elastic modeling.

Chapter 8

Modeling DARS

This chapter presents the application of the optimized variable grid FD method for DARS (Differential Acoustic Resonance Spectroscopy) modeling. DARS is a new technique to estimate the rock properties (velocity and attenuation) of a small sample by measuring the changes in resonances of a cavity that is perturbed by the introduction of the sample. The variable grid FD method is well suited for DARS modeling by giving fine discretization for the small sample and coarse discretization for the rest of the large cavity.

8.1 Introduction

A new method of measuring the velocity and attenuation parameter (Q) of sound, i.e., compressional waves, in small samples of rock has been proposed (Harris, 1997). This method, called Differential Acoustic Resonance Spectroscopy (DARS), is based on measuring the changes in resonances of a cavity that is perturbed by the introduction of the sample. From the changes of the resonance frequencies, we can estimate the sound velocity of the sample; from the changes of the resonance-peak bandwidths, we can estimate the Q of the sample. The changes in resonances of the cavity depend on the position of the sample along the cavity. One advantage of this method is that rock properties can be measured at frequencies as low as a few hundred Hertz in the laboratory, i.e., at seismic frequencies. Perhaps more importantly, small samples with irregular shapes such as borehole cuttings can be measured.

Based on the DARS approach, a basic apparatus has been set up in SWP (Stanford Wave Physics Lab) at Stanford University. In this setup (Figure 8.1), a circular cylindrical aluminum cavity with open-ends is suspended in a plastic tank filled with silicone oil. The experiment is performed as follows: (1) measure the resonance of the oil-filled cavity; (2) introduce a small sample of rock into the cavity and measure the change in resonance. Measurements are made for each small sample at different locations along the cavity. Lab data of some rocks and synthetic samples have been collected from this setup.

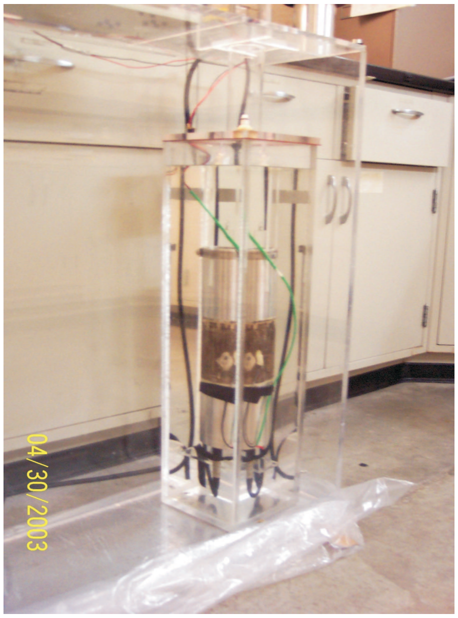

Figure 8.1: Experiment setup for DARS measurement. The open-ends circular cylindrical aluminum cavity is suspended in a plastic tank filled with silicone oil. A small sample can be put into the cavity and placed at different locations along the cavity. Resonances of the cavity with and without a sample are measured.

To better understand DARS theory, to guide experiment design, and to aid with the interpretation of lab data, numerical modeling on DARS is desirable. A big issue for DARS modeling is to handle a large-scale difference between a small sample and a large cavity. The optimized variable grid FD method developed in chapter 3 is well suited for solving this problem by giving fine discretization for the small sample and coarse discretization for the rest of the cavity. The use of the variable grid spacing can achieve both accuracy and efficiency in DARS modeling.

We apply the optimized variable grid FD method for solution of 2.5-D acoustic and visco-acoustic wave equations in cylindrical coordinates for DARS modeling. We conduct DARS methodology study, sensitivity prediction, and lab data modeling. The following sections present the method and the modeling results in detail.

8.2 Methods

To conduct the DARS modeling based on the experiment setup shown in Figure 8.1, we solve 2.5-D acoustic and visco-acoustic wave equations in cylindrical coordinates. The wave equations are:

1. Acoustic wave equation with variable density

$$\frac{\partial^2 p}{\partial t^2} = \rho c^2 [\frac{\partial}{\partial r}(\frac{1}{\rho}\frac{\partial p}{\partial r}) + \frac{1}{r\rho}\frac{\partial p}{\partial r} + \frac{\partial}{\partial z}(\frac{1}{\rho}\frac{\partial p}{\partial z})], \tag{8.1}$$

where p is the pressure, ρ and c are the density and the sound velocity of the medium.

2. Visco-acoustic wave equation with variable density

$$\frac{\partial^2 p}{\partial t^2} + \Gamma\frac{\partial p}{\partial t} = \rho c^2 [\frac{\partial}{\partial r}(\frac{1}{\rho}\frac{\partial p}{\partial r}) + \frac{1}{r\rho}\frac{\partial p}{\partial r} + \frac{\partial}{\partial z}(\frac{1}{\rho}\frac{\partial p}{\partial z})], \tag{8.2}$$

where $\Gamma = \omega/\mathrm{Q}$ is the damping constant for unit mass, and ω and Q are the resonant frequency and the quality factor.

Spatial derivatives in equation (8.1) and (8.2) are approximated using the fourth-order optimized variable grid FD operator (see chapter 3), and time derivatives are approximated using an explicit second-order central difference operator. With the spatial variable grid FD scheme, we can discretize the model with fine grid spacing for a small sample and coarse grid spacing for the rest of the cavity. The use of the variable grid spacing significantly reduces the computational time in the modeling, especially for DARS sensitivity study.

8.3 DARS modeling

In this section, we use 2.5-D acoustic and visco-acoustic codes for DARS modeling. First we conduct modeling for DARS methodology and sensitivity study. Then we perform DARS lab data modeling.

The numerical modeling is performed on a model based on the aluminum cavity in the lab (see Figure 8.1). In the modeling, we assume that the wall of the cavity is rigid and we represent the cavity's open-ends using the free boundary condition (pressure equals to zero). In the experiment, the pressure at the ends of the cavity is not zero; therefore we use a equivalent length in the modeling to model the cavity in the lab. The equivalent length is obtained through the calibration of the lab measured resonances of the cavity without the sample.

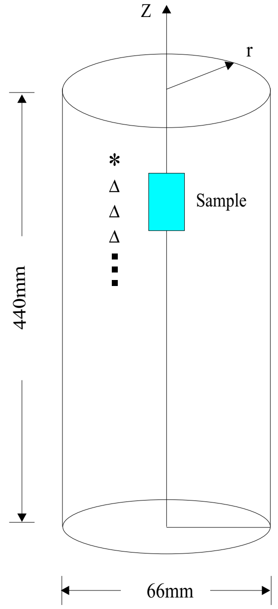

Figure 8.2: A oil-filled circular cylindrical cavity model. A small sample can be placed at any locations along the cavity.

Figure 8.2 shows the model. The circular cylindrical cavity with a diameter of 66 mm and a length of 440 mm is filled with silicon oil. The silicon oil has density of 913 kg/m^3 and acoustic velocity of 984 m/s. A small sample can be placed at different positions along the cavity for the modeling. We put a point source close to the top of the cavity and put receivers along the cavity. The source function used to excite the model is a sinc function with the amplitude of 1 for a frequency range of 400-7400 Hz (Figure 8.3). The simulation duration is 5 ms. In space, the model is discretized with fine grid spacing for the small sample and coarse grid spacing for the rest of the cavity. In time, a constant timestep of 0.0002 ms is used for the entire model. A number of tests have been carried out on this model.

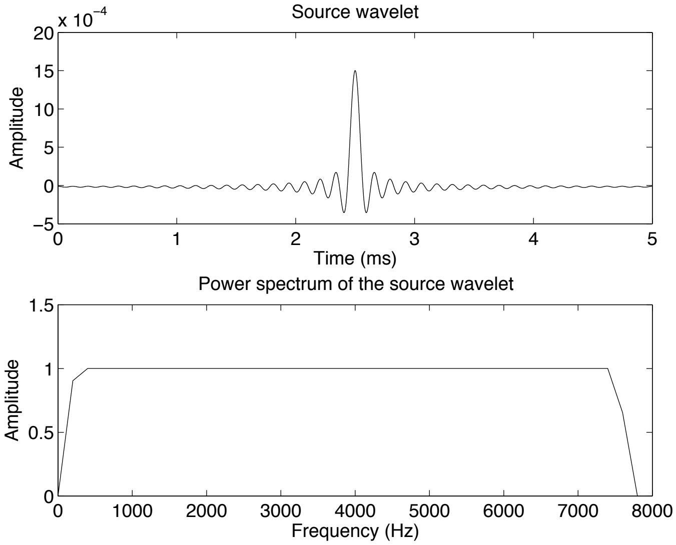

Figure 8.3: The source wavelet and its spectrum.

8.3.1 Methodology study

The DARS method is based on the perturbation theory (Appendix B) which states that the introduction of a small sample into a cavity causes the perturbation of the resonances of the cavity. Here we use numerical modeling to illustrate this.

1. Frequency shift

To show the resonance frequency shift due to a small sample, we perform the acoustic modeling for the cavity shown in Figure 8.2 with and without a sample. The sample has a dimension of 36 mm in diameter and 36 mm in length and has velocity of 2000 m/s and density of 1460 kg/m^3. For the modeling with the sample, the model is spatially discretized with variable grid spacing in z direction: a small grid spacing of 2 mm is used for the small sample and a large grid spacing of 4 mm is used for the rest of the cavity. The simulation total length is 1000 ms. We do Fourier transform for the pressure response of a receiver at z=20 mm in the cavity.

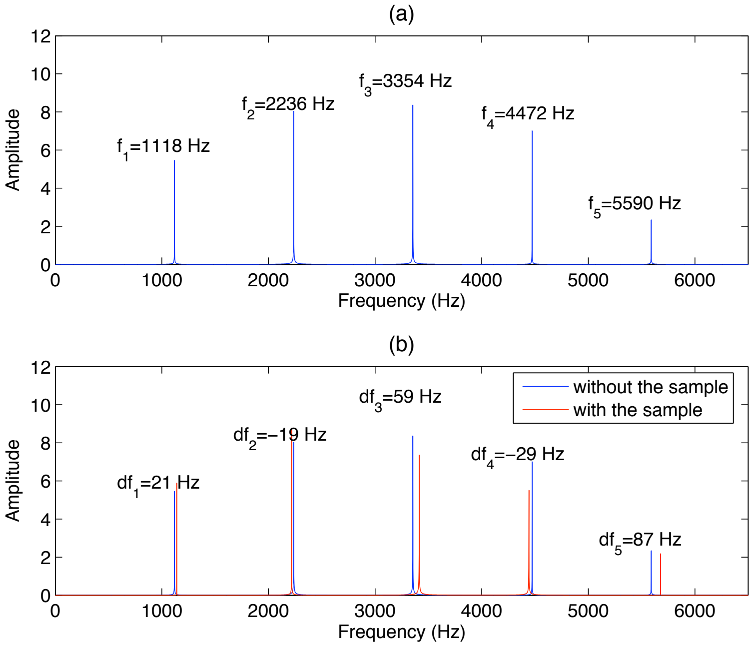

Figure 8.4: Pressure spectra of acoustic modeling. (a) Pressure spectrum of the cavity without the sample. The resonance frequencies of the 1^{st} to 5^{th} harmonics are 1118, 2236, 3354, 4472, and 5590 Hz. (b) Pressure spectra of the cavity with and without the sample. The resonance frequency shifts caused by the sample for the 1^{st} to 5^{th} harmonics are 21, -19, 59, -29, and 87 Hz.

The pressure spectrum for the cavity without the sample (Figure 8.4a) shows the resonance frequencies of the 1^{st} to 5^{th} harmonics are 1118, 2236, 3354, 4472, and 5590 Hz. These are exactly the same as those calculated from the theoretical formulation $f_n = c/2L$ (Appendix B) with c=984 m/s and L=440 mm. Figure 8.4b shows the comparison of the pressure spectra of the cavity with and without the sample. We can see the resonance frequency shift due to the small sample. The frequency shift depends on the acoustic velocity of the sample. Therefore, we can estimate the velocity of the small sample by measuring the resonance frequency shift of the cavity.

For the simulation of the cavity with the sample, the use of the variable grid spacing saves 40 % computer memory and 49 % CPU time compared to the use of a constant fine grid spacing for the entire model.

2. Attenuation effect

The above acoustic modeling on frequency shift study is based on an ideally lossless system, therefore we see spike-like resonances on the pressure spectra in Figure 8.4. In a lossy system, a resonance peak has a bandwidth which is related to the quality factor Q, the most common measure of attenuation, of the system. The introduction of a small sample into the cavity not only causes the resonance frequency shift but also causes the change in the resonance-peak bandwidth or linewidth. To illustrate this, we perform visco-acoustic modeling on the above two models with a given Q of 120 for the oil in the cavity and of 10 for the small sample.

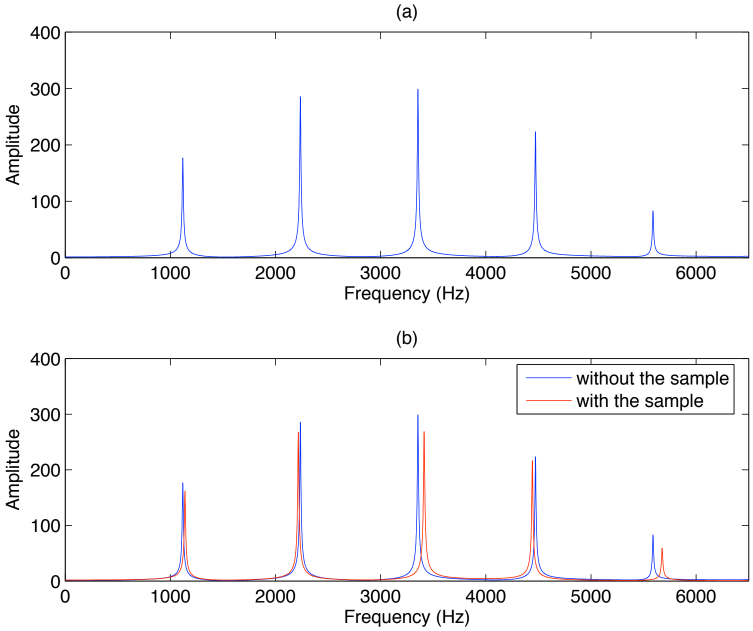

Figure 8.5: Pressure spectra of visco-acoustic modeling. (a) Pressure spectrum of the cavity without the sample (Q of oil $Q_o = 120$). (b) Pressure spectra of the cavity with and without the sample (Q of oil $Q_o = 120$, and Q of the sample $Q_s = 10$).

The pressure spectrum of the cavity without the sample of the visco-acoustic modeling is shown in Figure 8.5a. Unlike the spike-like resonances of the acoustic modeling (Figure 8.4a), each resonance of the visco-acoustic modeling has a bandwidth. A resonance-peak bandwidth Δf_n is defined as the frequency range between those values for which amplitude is 3 dB lower than the resonance peak amplitude. The quality factor Q can be estimated by $Q = f_n/\Delta f_n$.

The comparison of the pressure spectra of the cavity with and without the sample of the visco-acoustic modeling is shown in Figure 8.5b, which illustrates that the small sample not only causes the resonance frequency shift but also causes the resonance-peak bandwidth change. It is hard to see the quantitative change in the resonance-peak bandwidth in Figure 8.5b because the frequency range for the display is too large. We plot the spectra shown in Figure 8.5b with the frequency ranges of the 1^{st} and 2^{nd} normal modes in Figure 8.6 which clearly shows the change in the resonance-peak bandwidth, especially for the 1^{st} mode resonance (Figure 8.6a). The change of the resonance-peak bandwidth depends on the Q of the sample. Therefore, we can estimate the Q of the small sample by measuring the changes in the resonances of the cavity.

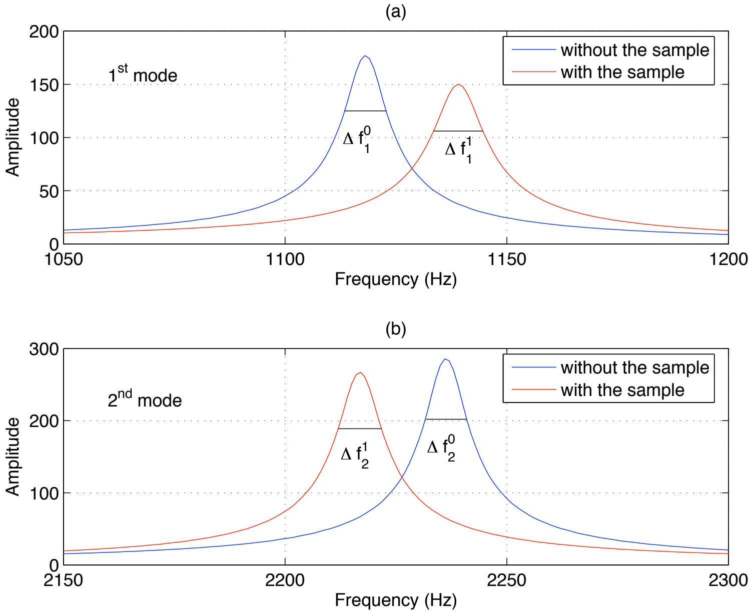

Figure 8.6: Comparison of resonances of the cavity with and without the sample: (a) The 1^{st} mode; (b) The 2^{nd} mode. Δf_n^0 and Δf_n^1 are the resonance-peak bandwidth for the cavity without and with the sample, respectively.

3. Position dependence

We have demonstrated the introduction of a small sample into a cavity causes the changes in the resonances of the cavity. These changes also depend on the position of the sample along the cavity. To illustrate this, we perform the visco-acoustic modeling for the same cavity with the sample at different locations.

Figure 8.7 shows the pressure spectra of the cavity for the frequency range of 500-6500 Hz. We can see that the changes in the resonances, especially of the higher modes, depend on the position of the sample. To clearly show the position dependence for the lower mode resonances, we plot the spectra with the frequency range of the 1^{st} mode (1050-1200 Hz) in Figure 8.8. We also plot the resonance frequency and the resonance-peak bandwidth versus the sample position in Figure 8.9a and 8.9b, respectively. The resonance-peak bandwidth versus the resonance frequency is shown in Figure 8.10 in which the Q of the system can be estimated by fitting the data.

For this position dependence study, we performed simulations for the cavity with the small sample at 44 different locations. The use of the variable grid spacing in spatial discretization saves a great amount of computational time in the modeling.

8.3.2 Sensitivity study

The DARS method is based on the perturbation theory (Appendix B); therefore it is more sensitive when the contrast of the properties (velocity and Q) of the small sample and the fluid in the cavity is not very large. Now we study the DARS sensitivity on measuring the velocity and Q using numerical modeling.

1. Sensitivity on velocity measurement

To study the DARS sensitivity on measuring the velocity of a small sample, we first assume that the sample has the same density as the silicon oil in the cavity. Then we smoothly change the velocity of the sample from 984 m/s (the same velocity of the silicon oil in the cavity) to 6000 m/s. The simulations are performed with the small sample at the center of the cavity.

Figure 8.11 shows the 1^{st} mode resonance frequency versus the velocity ratio of the small sample to the oil in the cavity ($\mathrm{c_s/c_o}$). We can see that the resonance frequency increases with the velocity faster when the velocity ratio is less than 2.5 ($c_s/c_o < 2.5$). This indicates that the DARS method is more sensitive on measuring the velocity of a small sample when the ratio of the velocity of the sample to the fluid in the cavity is less than 2.5.

2. Sensitivity on Q measurement

The modeling of DARS sensitivity on measuring Q is performed by assuming the sample with the same velocity and density as the oil in the cavity but with different Q. We keep the Q of 120 for the oil, and we smoothly change the Q of the sample from 1 to 360.

Figure 8.12 shows the Q of the system versus the ratio of Q between the small sample and the oil in the cavity (Q_s/Q_o). We can see that the Q of the system changes with the Q of the sample faster when the ratio of Q is less than 0.7 ($Q_s/Q_o \leq 0.7$). This indicates that the DARS method is more sensitive on measuring the Q of a small sample when the ratio of Q between the sample and the fluid in the cavity is less than 0.7.

The predicted DARS sensitivity through numerical modeling can aid in the design of the experiment in the laboratory.

We have performed more than 200 simulations for the sensitivity study on either velocity or Q. The variable grid FD method makes this done in 5 days rather than 10 days required by a constant grid FD method on a 1.4 GHz Athlon computer with 1 GB DDR RAM.

8.4 Lab data modeling

Lab data of some rocks and synthetic samples have been measured from the experiment setup shown in Figure 8.1. We have performed FD acoustic modeling on some of these data. Here we present the modeling results for a plastic sample and a sample of Berea. In data modeling, the dimension of the cavity and the properties of the enclosed silicon oil are the same as those used for the DARS methodology and sensitivity study.

1. Modeling the lab data of a plastic sample

The lab data of a plastic sample were measured with the plastic sample at 39 locations along the cavity. The plastic sample has a dimension of 38 mm in diameter and 36 in length. The density of the plastic sample is 1460 kg/m^3 measured directly in the lab. For FD modeling, the model is discretized with variable grid spacing in z direction: dz_1=1 mm for the small samples and dz_2=2 mm for the rest of the large cavity.

Since we do not know the velocity of the plastic sample, modeling with different velocities has been performed. We found that the modeling with the velocity of 2200 m/s for the plastic sample best fits the lab data.

Figure 8.13 shows the comparison of the modeling results (the velocity of the sample is 2200 m/s) and the lab data on the frequency shifts of the 1^{st}, 2^{nd}, and 3^{rd} normal modes. We can see that good agreement between the data and the modeling results on the three normal modes is achieved.

2. Modeling the lab data of a sample of Berea

The Berea lab data were measured with the Berea sample at 39 location along the cavity too. The dimension of the Berea sample is 25 mm in diameter and 75 mm in length. Berea has density of 2370 kg/m^3. Again FD modeling is performed on a spatially variable grid mesh with a fine grid spacing of 1 mm for the Berea sample and a coarse grid spacing of 2 mm for the rest of the cavity. Using numerical modeling to fit the lab data, we estimate a velocity of 3300 m/s for the Berea sample.

Figure 8.14 shows the comparison of the modeling results (the velocity of the Berea sample is 3300 m/s) and the lab data on the frequency shifts of the 1^{st}, 2^{nd}, and 3^{rd} normal modes. The agreement between the data and the modeling results on the three normal modes is excellent.

These two examples of the lab data modeling demonstrate the efficacy of our variable grid FD method for DARS modeling.

8.5 Conclusions

We have conducted numerical modeling to study DARS methodology, sensitivity and lab data using the variable grid FD method. The use of the variable grid spacing, which accommodates a small sample in a large cavity, greatly saves computational time in the modeling, especially for the DARS sensitivity study.

The DARS methodology study shows the changes in resonances of a cavity caused by the introduction of a small sample. The study also shows that the changes in resonances depend on the position of the small sample along the cavity. The sensitivity modeling study predicts that the DARS method is more sensitive on measuring: (1) the velocity of a small sample when the velocity ratio of the sample to the fluid in the cavity is less than 2.5; (2) the Q of a small sample when the Q ratio of the sample to the fluid in the cavity is less than 0.7. Lab data modeling achieves the excellent agreement between the numerical results and the lab data on resonance frequency shift. These studies demonstrate the efficacy of the variable grid FD method for DARS modeling.

Future work involves applying the visco-acoustic modeling for the lab data to fit not only the resonance frequency shift but also the resonance-peak bandwidth change. From this, we can invert Q of the sample from the lab data.

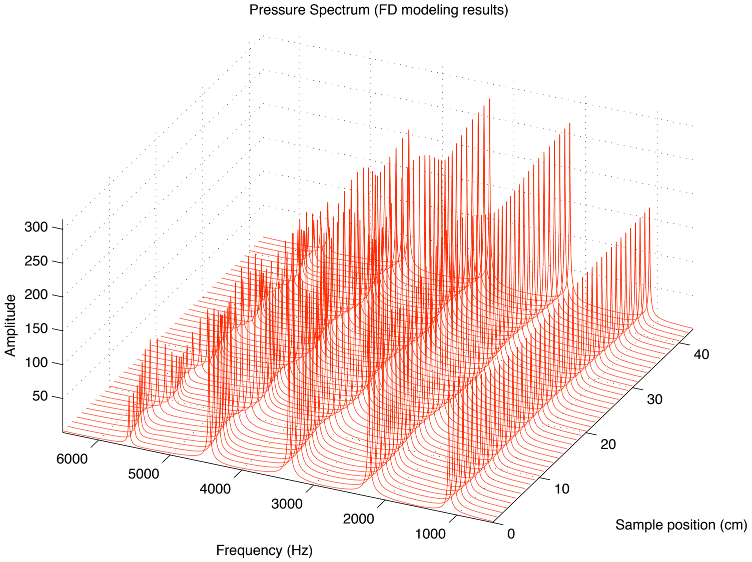

Figure 8.7: Pressure spectra of the cavity with the sample at different locations for the frequency range of 500-6500 Hz. we can see that the changes in the resonances depend on the position of the cavity.

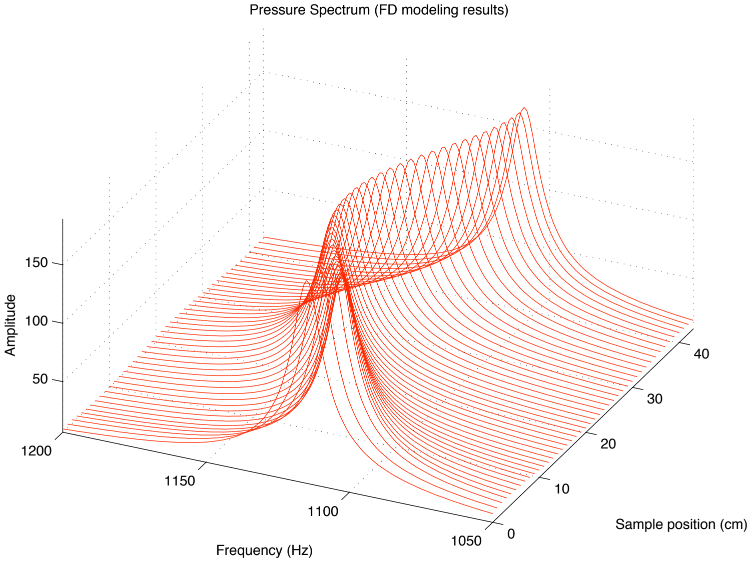

Figure 8.8: Pressure spectra of the cavity with the sample at different locations for the frequency range of 1050-1200 Hz. We clearly see that the change in the 1^{st} mode resonance depends on the position of the cavity.

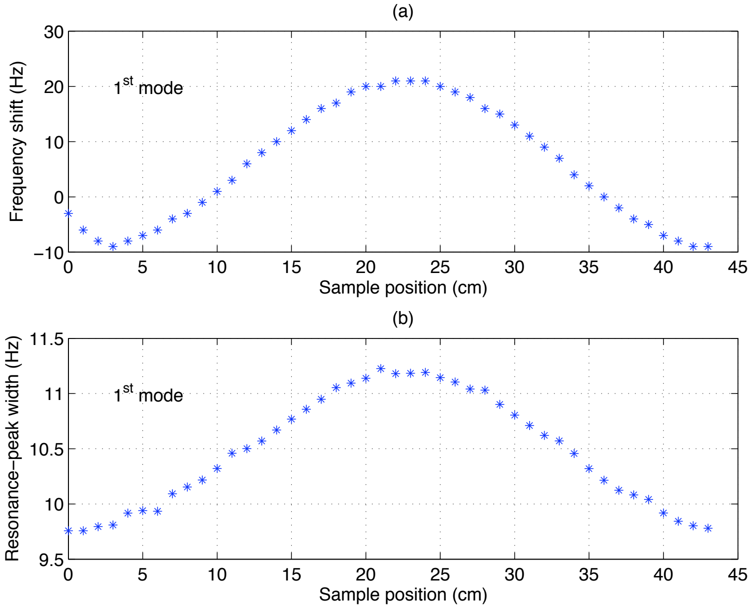

Figure 8.9: The change in the 1^{st} mode resonance: (a) Frequency shift versus. sample position; (b) Resonance-peak bandwidth versus sample position.

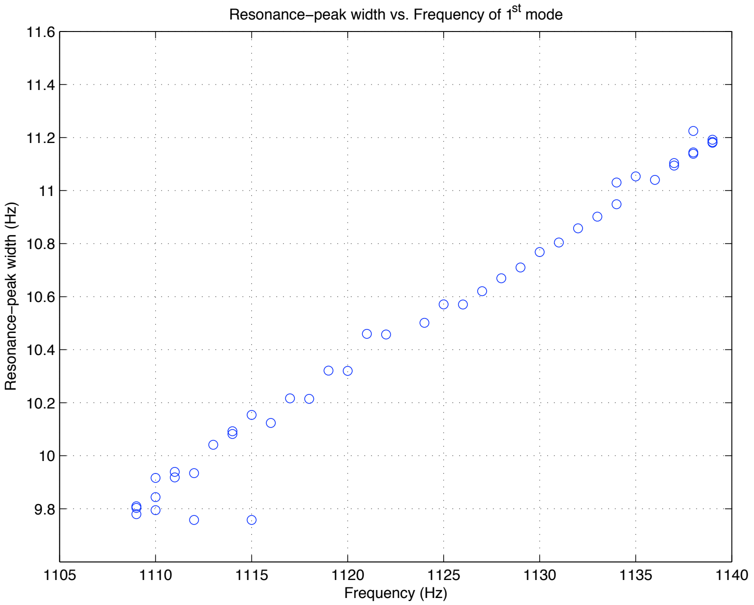

Figure 8.10: Resonance-peak bandwidth versus the resonance frequency of the 1^{st} mode.

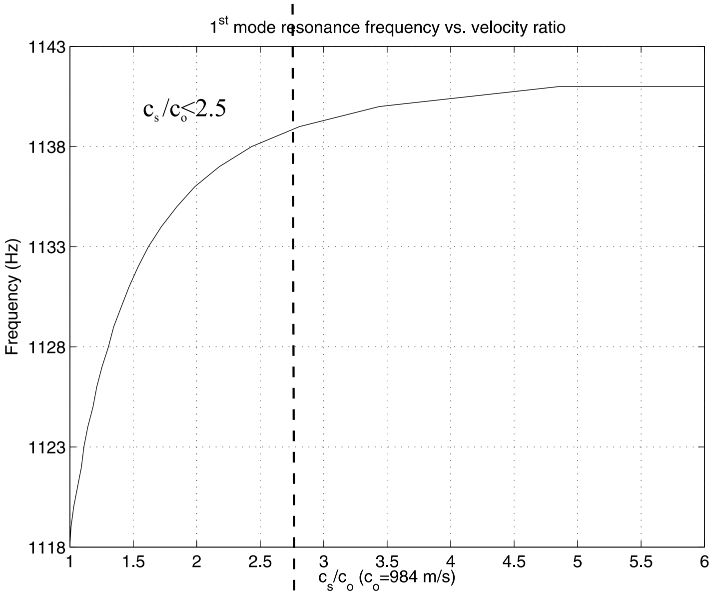

Figure 8.11: The 1^{st} mode resonance frequency versus the velocity ratio of the sample to the oil in the cavity. The resonance frequency increases faster when the velocity ratio is less than 2.5 ($\mathrm{c_s/c_o} < 2.5$).

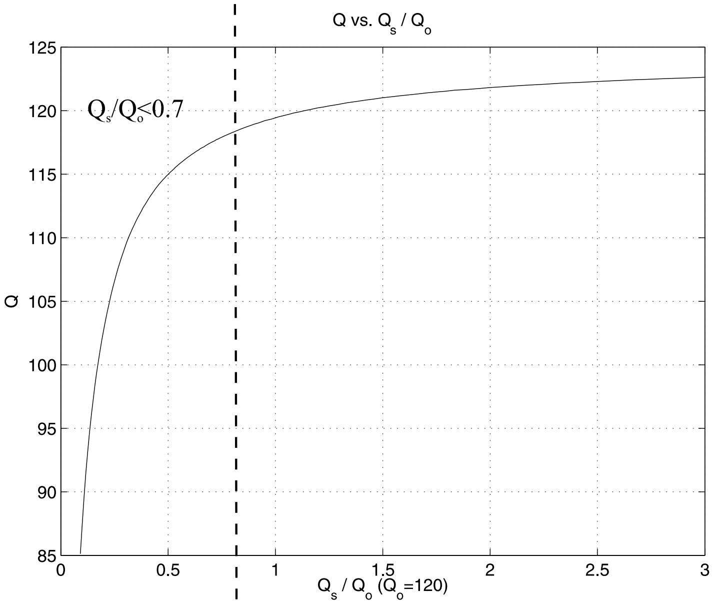

Figure 8.12: The Q of the system estimated from the 1^{st} mode resonance versus the ratio of Q between the sample and the oil in the cavity. Q changes faster when the ratio of Q is less than 0.7 ($\mathrm{Q_s/Q_o} < 0.7$).

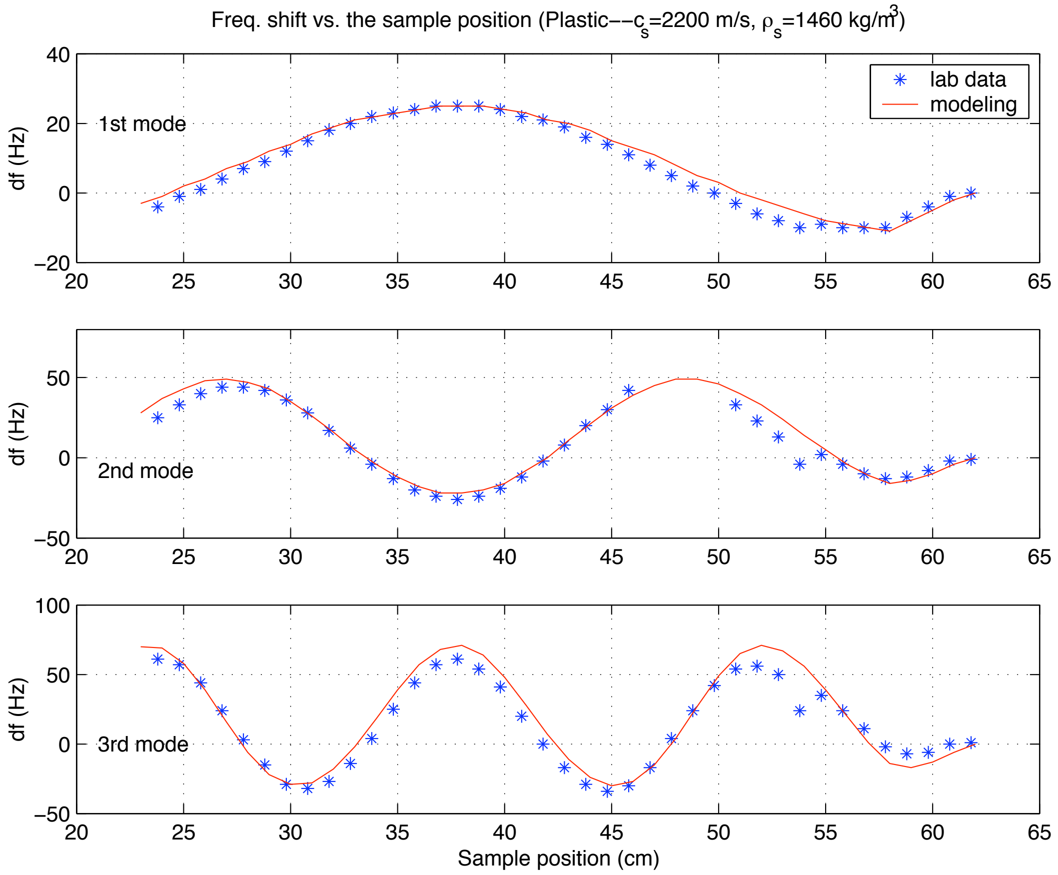

Figure 8.13: Comparison of the modeling results and the lab data of a plastic sample on frequency shift of the 1^{st}, 2^{nd} and 3^{rd} normal modes.

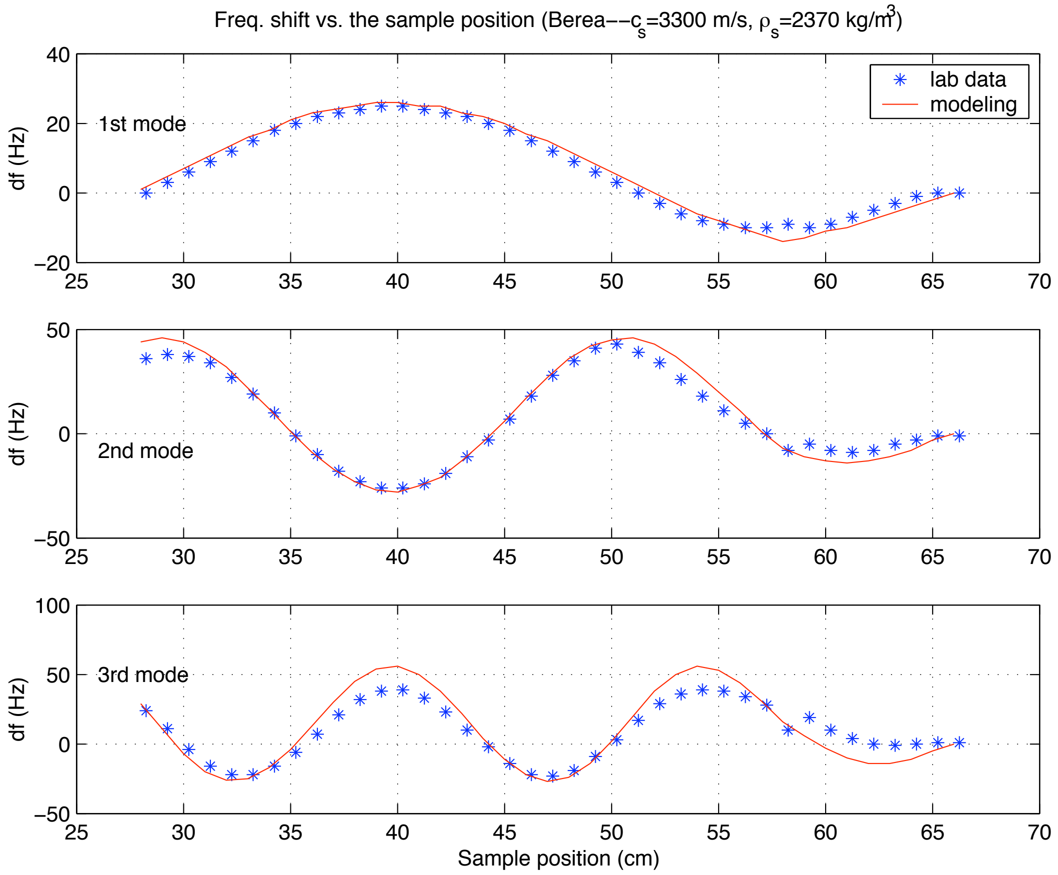

Figure 8.14: Comparison of the modeling results and the lab data of a Berea sample on frequency shift of the 1^{st}, 2^{nd} and 3^{rd} normal modes.

Appendix A

Fracture symmetric wave modes

In chapter 5, the comparison of numerical results between the TLM (thin-layer model) and the LSM (linear-slip model) is made on a model with a symmetric source-fracture geometry (Figure 5.3), therefore only symmetric wave modes along the fracture will be excited. In theory, the TLM supports a family of symmetric modes and the LSM supports only one symmetric mode. However, we only observe a slow guided wave in the TLM. To explain this, we present the analysis of fracture symmetric modes in this appendix.

Following Ferrazzini and Aki (1987), the symmetric modes existing along a fracture describe by the TLM are given by the following dispersion equations:

$$F = \frac{\rho_f}{q_f} \coth \frac{\omega q_f h}{2} + \frac{\rho_s}{q_p} R(\xi) = 0, \quad \text{for } \xi \geq 1/V_f \ , \tag{A-1a}$$

$$\frac{\rho_f}{q_f} \cot \frac{\omega q_f h}{2} - \frac{\rho_s}{q_p} R(\xi) = 0, \quad \text{for } 1/V_s \leq \xi \leq 1/V_f \ , \tag{A-1b}$$

where ξ is the phase slowness of the mode, ρ_f and ρ_s are the density of fluid and solid, respectively, h is the fracture aperture, ω is the angular frequency, and R is the

Rayleigh slowness relation

$$R = (2V_s^2\xi^2 - 1)^2 - 4V_s^4\xi^2 q_p q_s,$$

with the Rayleigh slowness of $R = 0$. The definition of the q's is:

$$q_f = \sqrt{|\xi^2 - 1/V_f^2|},$$
$$q_p = \sqrt{|\xi^2 - 1/V_p^2|},$$
$$q_s = \sqrt{|\xi^2 - 1/V_s^2|}.$$

The solution of the equation (A-1a) is the fundamental mode, which exists for all frequencies. The phase velocity of this mode is lower than the fluid velocity for all frequencies and decreases as the frequency decreases. Ferrazzini and Aki call this mode "very slow waves".

Solutions of the equation (A-1b) are a family of normal modes, which exist with ascending series of low cut-off frequencies at $\coth(\omega h q_f/2) = -(\rho_s q_f)/(\rho_f q_p)$ with $\xi = 1/V_s$. The phase velocities of these modes start from the S-wave velocity of the solid at the cut-off frequencies and approach the fluid velocity at high frequencies.

Theoretically, the linear-slip interface (the LSM) has only one symmetric mode which has the dispersion relation (Haugen and Schoenberg, 2000; Pyrak-Nolte and Cook, 1987):

$$1 - \frac{\omega Z_N}{2}\frac{\rho_s}{q_p}R(\xi) = 0, \tag{A-2}$$

where Z_N is the normal fracture compliance.

This symmetric interface wave, like the first normal mode in the TLM, has a low frequency cut-off, which is at $\omega = 2\sqrt{1/V_s^2 - 1/V_p^2}/(\rho_s Z_N)$, corresponding to a phase velocity of V_s. But unlike the first normal mode in the TLM, the phase velocity of this symmetric mode approaches to Rayleigh wave velocity at high frequencies.

Figure A.1 shows the dispersion curves of the slow wave (the fundamental symmetric mode) and the first symmetric normal mode in the TLM, and the symmetric mode in the LSM with the material parameters of the fracture model in chapter 5 (Figure 5.3). We can see that the slow wave in the TLM exists for all frequencies, while the first normal mode of the TLM and the symmetric mode of the LSM have low cut-off frequencies of 29.1 kHz and 20.4 kHz, respectively. For this model, a source pulse with central frequency of 3 kHz which is far below the cut-offs only excites the slow wave in the TLM. The numerical simulations in the paper confirm this theoretical prediction.

The slow wave observed in the snapshots of the TLM is traveling with a velocity around 1210 m/s. From equation (A-1a), we obtain a formula to theoretically predict the slow wave group velocity:

$$v_g = -\frac{\partial_k F}{\partial_\omega F} = \frac{1}{\xi(1 - \frac{\omega \partial_\omega F}{\xi \partial_\xi F})}. \tag{A-3}$$

At 3 kHz frequency, the slow wave phase velocity is 810 m/s (from Figure A.1), then its group velocity calculated from equation (A-3) is 1213 m/s, which is very close to that estimated from the numerical results. This further verifies the observed slow wave in the TLM and the used variable-grid FD modeling code.

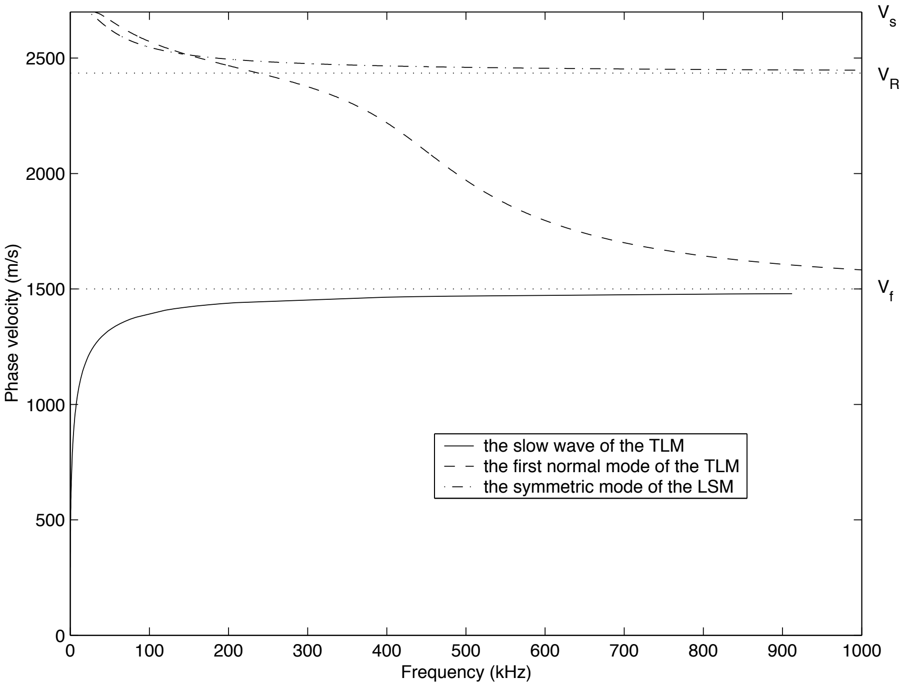

Figure A.1: Phase velocity as a function of frequency for the slow wave (the fundamental symmetric mode) and the first symmetric normal mode of the TLM, and the symmetric mode of the LSM, respectively. The material properties used are those for the fracture modeling in the text. V_R is the Rayleigh wave velocity.

Appendix B

DARS theory

In this appendix, we briefly review the quantitative analysis on the changes of the resonant frequencies of a cavity caused by the introduction of a small sample. This will help us better understand the DARS modeling study in chapter 8.

For a closed long and thin fluid-filled circular cylinder (a cavity) with rigid walls, (Figure B.1), the resonant frequencies of the longitudinal modes can be expressed as:

$$f_n = n\frac{c}{2L}, \quad (n = 1, 2, 3...), \tag{B.1}$$

where c is the sound velocity of the enclosed fluid in the cavity and L is the length of the cavity. The lowest frequency is called the fundamental frequency or the 1^{st} harmonic. Integer multiples of the 1^{st} harmonic are labeled as the 2^{nd}, 3^{rd}, etc., harmonics.

With the introduction of a small sample into this cavity (Figure B.2), the resonant frequencies of the system are perturbed to $f'_n = f_n + \Delta f_n$. The perturbation of the resonant frequencies can be quantitatively analyzed by considering scattering by the small sample (Morse and Ingard, 1968). From this analysis, the amount of the perturbation can be determined by:

$$\omega_n'^2 \approx \omega_n^2 - \frac{\omega_n^2}{A_n}(\frac{V_s}{V}) \iiint_{V_s} \delta\rho(|\rho_0 c_0 v_n|^2 - \delta\kappa p_n^2)\, dv, \tag{B.2}$$

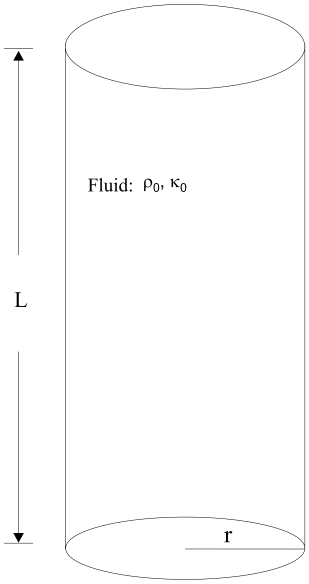

Figure B.1: A closed long and thin fluid-filled circular cylinder (r << L) with rigid walls has resonances f_n (n=1,2,...).

where $\omega_n' = 2\pi f_n'$ and $\omega_n = 2\pi f_n$; $\delta\rho$ and $\delta\kappa$ are the relative density and compressibility of the sample to the fluid in the cavity:

$$\delta\rho = \frac{\rho_s - \rho_0}{\rho_s}, \qquad \delta\kappa = \frac{\kappa_s - \kappa_0}{\kappa_0},$$

$c_0 = 1/\rho_0\kappa_0$ is the sound speed of the fluid in the cavity; V_s and V are the sample volume and the cavity volume, respectively; v_n and p_n are the velocity and the pressure inside the sample.

For $V_s \ll V$, equation (B.2) can be simplified to:

$$\omega_n'^2 \approx \omega_n^2 - \frac{\omega_n^2}{A_n}(\frac{V_s}{V}) \langle \rho_0 c_0 v_n \rangle^2 \delta\rho - \frac{\omega_n^2}{A_n}(\frac{V_s}{V}) \langle p_n^2 \rangle \delta\kappa \tag{B.3}$$

where

$$\langle \alpha^2 \rangle = \frac{1}{V_s} \iiint_{V_s} \alpha^2 \, dv,$$

is the RMS field (velocity and pressure) inside the sample.

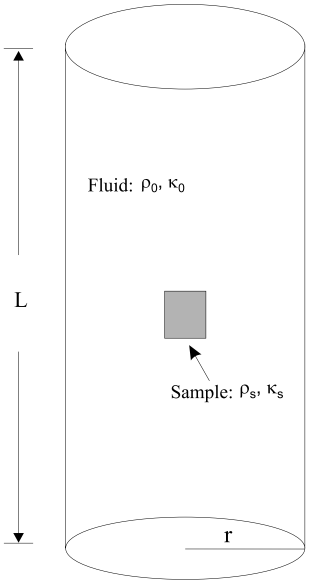

Figure B.2: The fluid-filled circular cylinder with a small sample has perturbed resonances $f_n + \Delta f_n$ (n=1,2,...).

From equation (B.3), we see that the change of the resonant frequencies proportional to the ratio of the sample volume to the cavity volume. A part of the change is proportional to the perturbation in the density times the mean-square velocity of the unperturbed wavefield. A second part of the change is proportional to the perturbation in the compressibility times the mean square of the pressure at the sample. Furthermore, we see that the change in frequency depends on the location of the sample.

In DARS, we measure the change of the resonant frequencies and estimate the sound velocity of the sample. This theory can be applied to porous media or attenuating media, therefore DARS provides a method for measuring Q and the permeability of the sample.

Bibliography

Aki, K., and Richards, P. G., 1980, *Quantitative Seismology*: W. H. Freeman and Company, San Francisco.

Auld, B. A., 1973, *Acoustic Fields and Waves in Solids, Vol. 1*: John Wiley and Sons, New York.

Alterman, Z., and Karal, F. C., 1968, Propagation of elastic waves in layered media by finite difference methods: Bull. Seism. Soc. Am., 58, 367-398.

Balch, A. H., and Lee, M. W., 1984, Vertical seismic profiling: Technique, applications, and case histories, report, Int. Human Resour. Develop. Corp., Boston, Mass.

Boore, D. M., 1972, Finite-difference methods for seismic wave propagation in heterogeneous materials, in Methods in computational physics, 11: B. A. Bolt, Ed., Academic Press.

Cameron, D. S., and Chen, S. T., 1995, Single-well salt-flank imaging, 65th Ann. Internat. Mtg: Soc. of Expl. Geophys., 461-464

Campbell, A. J., 1992, Tube wave attenuation by Polarization Filtering, 62nd Ann. Internat. Mtg: Coc. of Expl. Geophys., 99-102.

Cerjan, C., Kosloff, D., Kosloff, R., and Reshef, M., 1985, A nonreflecting boundary condition for discrete acoustic and elastic wave equations: Geophysics, 50, 705-708.

Cerveny, V., Molotkov, I. A., and Psencik, I., 1977, *Ray Method in Seismology*: Monograph. University Karlova, Praha.

Chapman, C., 2004, *Fundamentals of Seismic Wave Propagation*: Cambridge University Press.

Coates, R. T., and Schoenberg, M., 1995, Finite-difference modeling of faults and fractures: Geophysics, 60, 1514-1526.

Cruse T. A., and Rizzo, F. J., 1968, A direct formulation and numerical solution of the general transient elastodynamic problem, I: J. Math. Anal. Appl. 22, 244-259.

Cruse T. A., 1968, A direct formulation and numerical solution of the general transient elastodynamic problem, II: J. Math. Anal. Appl. 22, 341-355.

Davis, J. L., 1988, *Wave Propagation in Solids and Fluids*: Springer-Verlag, New York.

Drake, L. A., 1972, Love and Rayleigh waves in nonhorizontally layered media: Bull. Seism. Soc. Am., 62, 1241-1258.

Ewing, R. E., Sharpley, R. C., Mitchum, D., O'Leary, P., and Sochacki, J. S., 1994, Distributed computation of wave propagation models using PVM: IEEE Parallel & Distributed Technology: Systems & Applications, 2, 26-31.

Falk, J., Tessmer, E., and Gajewski, D., 1996, Tube wave modeling by the finite-difference method with varying grid spacing: Pure and Applied Geophysics, 148, 77-93.

Falk, J., and Tessmer, E., 1998, Efficient finite-difference modeling of seismic waves using locally adjustable time steps: Geophys. Prosp., 46, 603-616.

Faria, E. L., and Stoffa, P. D., 1994, Finite-difference modeling in transversely isotropic media: Geophysics, 59, 282-289.

Ferrazzini, V., and Aki, K., 1987, Slow waves trapped in a fluid-filled infinite crack: implication for volcanic tremor: J. Geophys. Res., 92, 9215-9223.

Garotta, R., 1989, Detection of azimuthal anisotropy, 59th Ann. Internat. Mtg: Soc. of Expl. Geophys., 861-863.

Gazdag, J., 1981, Modeling of the acoustic wave equation with transform methods: Geophysics, 46, 854-859.

Graves, R. W., 1996, Simulation seismic wave propagation in 3D elastic media using staggered-grid finite differences: Bull. Seim. Soc. Am., 86, 1091-1106.

Groenenboom, J., and Fokkema, J., 1998, Guided waves along hydraulic fractures, 68th Ann. Internat. Mtg: Soc. of Expl. Geophys., 1632-1635

Groenenboom, J., and Falk, J., 2000, Scattering by hydraulic fractures: Finite-difference modeling and laboratory data: Geophysics, 65, 612-622.

Gropp, W., Lusk, E., Doss, N., and Skjellum, A., 1996, A high-performance, portable implementation of the MPI message passing interface standard: Parallel Computing, 22, 789-828.

Harris, J. M., 1997, Differential acoustic resonance spectroscopy: STP report, Stanford University.

Haugen, G. U., and Schoenberg, M., 2000, The echo of a fault or fracture: Geophysics, 65, 176-189.

Jastram, C., and Behle, A., 1991, Elastic modeling by finite-difference and the rapid expansion method (REM), 61st Ann. Internat. Mtg: Soc. of Expl. Geophys., 1573-1576.

Jastram, C., and Tessmer, E., 1994, Elastic modeling on a grid with vertically varying spacing: Geophys. Prosp., 42, 357-370.

Kelly, K. R., Ward, R. W., Treitel, S., and Alford, R. M., 1976, Synthetic seismograms: A finite-difference approach: Geophysics, 41, 2-27.

Kosloff, D. D., and Baysal, E., 1982, Forward modeling by a Fourier method: Geophysics, 47, 1402-1412.

Lamb, H., 1904, On the propagation of tremors over the surface of an elastic solid: Phil. Trans. Roy. Soc. London, A203, 1-42.

Levander, A. R., 1988, Fourth-order finite-difference P-SV seismograms: Geophysics, 53, 1425-1436.

Luo, Y., and Schuster, G., 1990, Parsimonious staggered grid finite-differencing of the wave equation: Geophys. Res. Lett., 17, 155-158.

Lynn, H. B., and Thomsen, L. A., 1986, Reflection shear-wave data along the principal axes of azimuthal anisotropy, 56th Ann. Internat. Mtg.: Soc. of Expl. Geophys., Session:S9.5.

Lynn, H. B., Bates, C. R., Simon, K. M., and van Dok, R., 1995, The effects of azimuthal anisotropy in P-wave 3-D seismic, 65th Ann. Internat. Mtg: Soc. of Expl. Geophys., 727-730.

Lysmer, J., and Drake, L. A., 1972, A finite element method for seismology; Ch. 6 in B. Alder, S. Fernbach and B. A. Bolt, Ed., Methods in Computational Physics 11, Seismology, Academic Press.

Madariaga, P., 1976, Dynamics of an expanding circular fault: Bull. Seim. Soc. Am., 66, 639-666.

Majer, E.L., Peterson, J.E., Daley, T., Kaelin, B., Myer, L., Queen, J., D'Onfro, P., and Rizer, W., 1997, Fracture detection using crosswell and single-well surverys, 62th Ann. Internat. Mtg: Soc. of Expl. Geophys., 495-504

Mjelde, R., 1992, Reflection and polarization of tube waves as seen in VSP data: Geophys. Prosp., Eur. Assn. Geosci. Eng., 40, 605-618.

Mo, L.-W., and Harris, J. M., 1995, Analysis and attenuation of tube waves in crosswell seismic survey, 65th Ann. Internat. Mtg: Soc. of Expl. Geophys., 438-441.

Moczo, P., 1989, Finite-difference technique for SH waves in 2-D media using irregular grids-application to the seismic response problem: Geophys. J. Int., 99, 321-329.

Morse, P. M., and Ingard, K. U., 1968, *Theoretical Acoustics*: McGraw-Hill Book Company, New York.

Nagano, K., and Niitsuma, H., 1996, Crack stiffness from crack wave velocities: Geophys. Res. Lett., 23, 689-692.

Nihei, K. T., Nakagawa, S., and Myer, L. R., 2001, Fracture imaging with converted elastic waves, *in* Elsworth, D., Tinucci, J. P., and Heasley, K. A., eds., *Rock Mechanics in the National Interest*: A.A. Balkema, 1305-1131.

Olsen, K., and Schuster, G. T., 1992, Seismic hazard analysis in Salt Lake Valley by finite-difference simulation of three dimensional elastic wave propagation, in Scientific Excellence in High Performance Computing: The 1990 IBM Price Papers, Vol. 1, Sec. 6, Baldwin Press, Athens, Georgia, 135-165.

Pitarka, A., 1999, 3D elastic finite-difference modeling of seismic motion using staggered grids with nonuniform spacing: Bull. Seim. Soc. Am., 89, 54-68.

Pyrak-Nolte, L. J., and Cook, N. G. W., 1987, Elastic interface waves along a fracture: Geophys. Res. Lett., 14, 1107-1110.

Pyrak-Nolte, L. J., 1988, Seismic visibility of fractures, PhD thesis, University of California at Berkeley.

Randal, C. J., 1989, Absorbing boundary condition for the elastic wave equation: Velocity-stress formulation: Geophysics, 54, 1141-1152.

Schoenberg, M., 1980, Elastic wave behavior across linear slip interfaces: J. Acoust. Soc. Am., 68, 1516-1521.

Schoenberg, M., and Sayers, C. M., 1995, Seismic anisotropy of fractured rock: Geophysics, 60, 204-211.

Saenger, E. H., Gold, N., and Shapiro, S. A., 2000, Modeling the propagation of elastic waves using a modified finite-difference grid: Wave Motion, 31, 77-92.

Tam, C. K. W., and Webb, J. C., 1993, Dispersion-relation-preserving difference schemes for computational acoustic: J. of Comput. Physics, 107, 262-281.

Tessmer, E., 2000, Seismic finite-difference modeling with spatially varying time steps: Geophysics, 65, 1290-1293.

Villarreal, A., and Scales, J. A., 1997, Distributed three-dimensional finite-difference modeling of wave propagation in acoustic media: Computers in Physics, 11, 388-399.

Virieux, J., 1984, SH-wave propagation in heterogeneous media: Velocity-stress finite-difference method: Geophysics, 49, 1933-1942.

Virieux, J., 1986, P-SV wave propagation in heterogeneous media: Velocity-stress finite-difference method: Geophysics, 51, 889-901.

White, J. E., and Lessenger, M. A., 1988, Caliper effect on borehole coupling: Expl. Geophys., 19, 201-205.

White, J. E., 1983, *Underground Sound-Application of Seismic Waves*: Elsevier, New York.

Wu, C., Harris, J. M., Kurt, N. T., and Nakagawa, S., 2005, 2-D finite-difference seismic modeling of an open fluid-filled fracture: comparison of thin-layer and linear-slip models, Geophysics, in press.

Wu, C. and Harris, J. M., 2004, Cross-well seismic modeling with inclusion of tube waves and tube-wave-related arrivals: Geophys. Res. Lett., Vol. 31, No. 11, L11606.

Wu, C. and Harris, J. M., 2004, An optimized variable-grid finite-difference method for seismic forward modeling, J. Seism. Expl., 12, 343-353.

Wu, C., Harris, J. M., Daley, T. M. and Majer, E. L., 2004, San Juan single-well seismic data analysis and modeling study, 74th Ann. Internat. Mtg: Soc. of Expl. Geophys., 342-345.

Wu, C., and Harris, J. M., 2003, Borehole seismic modeling with inclusion of tube-waves and other tube-wave-related arrivals, 73rd Ann. Internat. Mtg: Soc. of Expl. Geophys., 2239-2242.

Wu, C., Harris, J. M., and Kurt, N. T., 2002, 2-D finite-difference seismic modeling of an open fluid-filled fracture: comparison of thin-layer and linear-slip models, 72nd Ann. Internat. Mtg: Soc. of Expl. Geophys., 1959-1962.

Wu, C., and Harris, J. M., 2002, An optimized variable grid finite-difference method for seismic forward modeling, paper presented at SEG Post-Convention Workshop - Advances and limitations in numerical modeling of wave propagation in challenging structures, 72nd Ann. Internat. Mtg: Soc. of Expl. Geophys., Salt Lake City, Utah.

Wu, C., Harris, J. M., and Franklin, J., 2001, Single-well seismic modeling in viscoelastic media using a variable-grid finite-difference method, 71st Ann. Internat. Mtg: Soc. of Expl. Geophys., 1155-1158.

Xu, T., and McMechan, G. A., 1998, Efficient 3-D viscoelastic modeling with application to near-surface land seismic data: Geophysics, 63, 601-612.

Zhang, J., 1997, Quadrangle-grid velocity-stress finite-difference method for elastic-wave-propagation simulation: Geophys. J. Int., 131, 127-134.